STM TRANSPORT THROUGH COPPER PHTHALOCYANINE ON THIN INSULATING FILMS

DISSERTATION ZUR ERLANGUNG DES DOKTORGRADES DER NATURWISSENSCHAFTEN (DR. RER. NAT.) DER FAKULTÄT PHYSIK DER UNIVERSITÄT REGENSBURG

vorgelegt von Benjamin Siegert aus Hirschau

im Jahr 2015

Promotionsgesuch eingereicht am: 16.10.2015

Die Arbeit wurde angeleitet von: Prof. Dr. Milena Grifoni

Prüfungsausschuss:
Vorsitz: Prof. Dr. John Lupton
Erstgutachter: Prof. Dr. Milena Grifoni
Zweitgutachter: Prof. Dr. Jascha Repp
Weiterer Prüfer: Prof. Dr. Ingo Morgenstern

In loving memory of Barbara Künzl

ABSTRACT

This thesis comprises the description and analysis of electronic transport through copper phthalocyanine in an STM setup on thin insulating films. A major part deals with the derivation of a semi-empirical many-body Hamiltonian in the molecular basis for copper phthalocyanine. The symmetry of the molecular orbitals allows for reducing the required number of matrix elements of the Coulomb interaction. Later on, also spin-orbit interaction and interactions with magnetic fields are added to the description of copper phthalocyanine and we derive an effective low-energy Hamiltonian which allows for the identifaction of the different many-body transitions observed in the numerical transport calculations. Transport dynamics is obtained by evaluating a master equation for the reduced density operator. Thereby, STM-specific properties are contained in the tunneling matrix elements, which describe the tunneling of electrons from the tip and the substrate onto the molecule. Using this transport formalism and the many-body Hamiltonian for copper phthalocyanine, we find negative differential conductance phenomena caused by interference of many-body states. Furthermore, a tip-position controlled population inversion to an excited neutral state of the molecule is identified. Associated to the latter is the change of the total spin of the molecule from a low-spin to a high-spin state.

PUBLICATIONS

Large portions of the chapters have appeared in the following publications:

1. A. Donarini, B. Siegert, S. Sobczyk, and M. Grifoni. Topographical fingerprints of many-body interference in STM junctions on thin insulating films. Phys. Rev. B **86**, 155451, 2012.

2. B. Siegert, A. Donarini, and M. Grifoni. Non-equilibrium spin-crossover in copper phthalocyanine. Preprint (submitted to Phys. Rev. Lett.), arXiv:1507.05504v2.

3. B. Siegert, A. Donarini, and M. Grifoni. Effects of spin-orbit coupling and many-body correlations in STM transport through copper phthalocyanine. Preprint (accepted for publication in Beilstein J. Nanotechnol.), arXiv:1508.04647.

The following publication, based on my diploma thesis, was also completed and published during the doctorate:

1. B. Siegert, A. Donarini, and M. Grifoni. The role of the tip symmetry on the STM topography of π-conjugated molecules. Phys. Stat. Sol. (b) **250**, 2444, 2013.

ACKNOWLEDGMENTS

I would like to thank all the people that have contributed to making this thesis possible. First and foremost I am deeply grateful to my supervisor Milena Grifoni for providing me the possibility to write and finish this thesis at her chair, and for creating an enjoyable and stimulating atmosphere to work in. I would also like to thank her for her guidance helping me to maneuver through this work during the past years, and for her patience especially in the last few weeks and months. I would also like to thank Andrea Donarini. With pleasure I look back to all the countless nice (and quite lengthy) discussions concerning our research, about problems in the model and the numerics, but also about many non-academic things. He has always had a friendly ear; and I hope I inherited a bit of his great intuition for physics and for finding clean and coherent models, or, as he calls them, "elaborate guesses". Gratitude is owed also to all my other colleagues for the cheerful and pleasant times I spent with them together at our chair; in particular to my friends Sebastian Pfaller and Paul Wenk. Without them, working at the university would not have been nearly as much fun, and sharing an office with Paul was one of the best experiences during my doctorate. I am also very grateful to Robert Hrdina who has been very helpful in all sorts of administrative and bureaucratic problems. Finally, I want to thank my family for their endless support throughout all the years of my study and my doctorate. I also want to thank Elisabeth for cheering me up during the last weeks of finishing this thesis. In particular I want to thank my girlfriend Christine for encouraging me and lending her support, especially during the writing stage.

CONTENTS

LIST OF FIGURES

LIST OF TABLES

ACRONYMS

STM scanning tunneling microscope

TME tunneling matrix element

GME generalized master equation

RDM reduced density matrix

SCO spin crossover

HS high spin

LS low spin

MPc metal phthalocyanine

CuPc copper phthalocyanine

FePc iron phthalocyanine

SOI spin-orbit interaction

MO molecular orbital

LCAO linear combination of atomic orbitals

HOMO highest occupied molecular orbital

SOMO singly occupied molecular orbital

LUMO lowest unoccupied molecular orbital

NDC negative differential conductance

XMCD X-ray magnetic circular dichroism

1 INTRODUCTION

In this chapter we give a short overview about the field of single molecule junctions. We then turn our attention to the scanning tunneling microscope (STM) and discuss its basic operating principle and different use cases. Last but not least we introduce the family of the phthalocyanines, molecules that are used in many different areas ranging from physics and chemistry to technology.

1.1 SINGLE MOLECULE JUNCTIONS

Single molecule junctions are a youthful field of research in physics. Altough already in 1974 a single molecule was proposed as a molecular rectifier in the theoretical work of Aviram and Ratner [AR74], it took over 20 years, after some setbacks [AJP88, AJP89], until the conductance of an actual single molecule junction was measured by Joachim et al. [JGSC95]. In the experiment an STM was used to contact a C_{60} molecule. Since then, single molecule junctions have attained broad interest [AV13], both theoretically [CCL07, BMO+02, DVPL00] and experimentally [RZM+97, SNU+02, ROB+02, XT03]. One very prominent experimental technique for the realization of a single molecule junction is the break junction technique [SNU+02]: Here, a gap in a thin conducting wire is either formed mechanically, chemically or electrically. The mechanical way is to put the wire on a supporting substrate and then to push the substrate from below with a nanorod until the nanowire breaks and a gap is formed. Chemically, gap formation can be achieved by etching. Electrically, by electromigration, where high currents which are passed through the wire cause the ablation of atoms in the wire [PLA+99]. The formation of the gap then can be monitored by measuring the conductance; it decreases in steps of one conductance quantum, as the atoms which are connecting the two sides of the wire are reduced, and falls below one conductance quantum when a gap is formed [RFU00]. Another way of realizing a single molecule junction is to integrate sulfur anchoring groups into molecules and use the fact that sulfur very strongly binds to gold [MWR+03]. Also fullerenes have been proposed as promising anchoring groups [MDS+08]. Last but not least, STMs are outstandingly suitable for the realization of single molecule junctions, both in the tunneling regime [QNH03] and in contact [XT03]. In particular, the role of many-body effects in STM-based single molecule junctions is gaining more and more interest, theoretically [SDG12, DSSG12, TRC11, TRC13, SID+15] as well as experimentally [SSR11, SID+15, MGD+12, GMN+12, LDWG15].

1.2 THE SCANNING TUNNELING MICROSCOPE

The STM was invented by Binnig and Rohrer [BRGW82] in 1982 at the IBM labs in Zürich. Its most essential part is a metallic tip which is mounted above a metallic substrate. Through the use of piezoelectric transducers, which contract or expand when a voltage is applied on them, the tip can be moved in all three dimensions with high accuracy.

The operational principle of an STM is based on quantum tunneling: When the tip is near the sample and a bias voltage between tip and substrate is applied, the finite overlap between the wavefunctions of electrons in the tip and electrons in the substrate makes it possible for a tip electron to tunnel out of the tip into the substrate, generating current. Intuitively, this current is in first approximation proportional to the local density of states of the substrate. Having the tip at fixed distance to the sample and at finite bias voltage, scanning in x- and y-direction thus produces a map of the tip-position dependent tunneling current. This operating mode is called constant height mode. Alternatively, a feedback loop can be switched on: It compares the measured current to a predetermined reference current, the setpoint. If the measured current is larger (smaller) than the setpoint, a corresponding voltage is applied to the piezo driver in z-direction which then in turn increases (decreases) the tip-sample distance. During this constant current mode, the relative z-positions with respect to the initial z-position are recorded.

In addition to topographical images, STM can also give spectroscopic information by measuring at a fixed tip position the current in dependence of the applied bias voltage; specifically, using lock-in techniques, by measuring the differential conductance one can obtain information about the spectral properties of the sample.

As discussed in the previous section, STM junctions involving single molecules are particularly interesting. Put directly on a metal substrate, they can for example reveal Kondo enhancement [GMN+12, MRK+12], giant magnetoresistance [SBN+11], spin crossover (SCO) [GMN+12] and negative differential conductance [GLH00]. If in direct contact with a metallic substrate, molecules are strongly perturbed due to hybridization. In order to avoid this, an insulating layer on top of the metal substrate can be added to effectively decouple the molecule from the substrate while still enabling tunneling [RMSac+05, GMM+11], thus allowing the investigation of nearly pristine molecules. However, also in connection with insulating layers substrate-induced effects like charging [SSR11, LDWG15] and bistability [SID+15, SSR11, LRM07a] can occur.

The theoretical description of STM transport is a difficult task. Because of its inherently large parameter space, there exist many different models trying to give insight into experiments [HFS03]. The most widely used approach to describe STM was proposed by Tersoff and

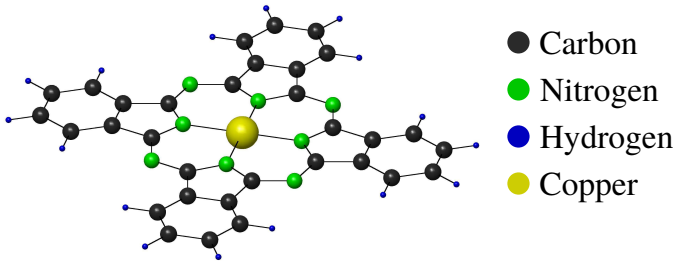

Figure 1.1: Geometry of a metal phthalocyanine molecule on the example of copper phthalocyanine.

Hamann [TH83], based on the tunneling theory of Bardeen [Bar61]. They concluded that the current in STM experiments is proportional to the local density of states of the molecule, evaluated at the position of the tip $\mathbf{r}_\mathrm{T}$:

$$I \sim \sum_\nu |\psi_\nu(\mathbf{r}_\mathrm{T})|^2 \, \delta\left(E_\nu - E_\mathrm{F}\right), \tag{1.1}$$

where E_F is the Fermi energy of the sample and E_ν is the energy of the sample wavefunction ψ_ν. As we will show in the later chapters in this work, there exist many circumstances where the recorded current does not resemble the local density of states of the molecule; rather its topographical features can depend strongly on many-body effects.

1.3 PHTHALOCYANINES

Phthalocyanines are heteronuclear organic macrocycles made of an inner cycle, consisting of alternating carbon and nitrogen atoms, and of four benzene rings covalently bonded to the inner cycle, see Fig. 1.1. In hydrogen phthalocyanine (H_2Pc) the center of the molecule either comprises two hydrogen atoms bonded to two of the inner nitrogens, whereas in metal phthalocyanine (MPc) there is one metal atom at the center. The different possible metal centers found in phthalocyanines are numerous: Just to name a few, common metals are Mn, Fe, Co, Ni, Cu, Zn, etc. All in all there are over 70 possible different phthalocyanine complexes [OB92]. Most metal phthalocyanines are square planar molecules and belong to the D_{4h} rotational group, thus having a fourfold principal symmetry axis through the center of the molecule, and four twofold symmetry axes going through the inner lying or the outer lying nitrogens (see Fig. 1.1), respectively. The planarity of MPc is also mirrored in their electronic structures: The π-system, comprising all orbitals which point out of the molecular plane, is decoupled from the σ-system, which consists of the orbitals that are overlapping in the molecular plane.

Technologically, phthalocyanines have already reached everyday life in the form of dyes (phthalo blue) and inks. Some of their most promising future applications lie in gas and radiation sensors [TES+92], fuel

cells [BJ84], organic light emitting diodes [QGWW02], organic field effect transistors [BLD96] and various others [KSG03].

Also, from the experimental point of view phthalocyanines are fascinating molecules: The list of novel phenomena appearing in phthalocyanine-based experiments goes from current-induced tautomerization [LRM07b], giant magnetoresistance [SBN+11, WEHP+15] and negative differential conductance (NDC) [TMH08, WEHP+15] through to giant orbital anisotropy [SMC+10], bistability [SSR11, SID+15] and the Kondo effect [MRK+12].

1.4 OUTLINE

This thesis contains the description and analysis of electronic transport through copper phthalocyanine (CuPc) in an STM setup on thin insulating films. In the following we give an outline of this thesis:

In Chapter 2 we introduce the molecular Hamiltonian. Starting from the atomic basis, we rewrite the Hamiltonian in the molecular orbital (MO) basis and explain the possible advantages a description has in this basis. We then illustrate this approach on the example of CuPc. Moreover, we identify the most relevant MO for transport; by exploiting their symmetry properties we are able to set up a model many-body Hamiltonian for CuPc containing all possible Coulomb interaction terms between the frontier orbitals.

Chapter 3 is dedicated to the derivation of our STM transport formalism. We identify the most important ingredients that enable us to describe STM transport and proceed to derive a master equation for the reduced density matrix (RDM) of the system. We further examine how electrostatic interactions with the environment can influence the charge states of the molecule. After explaining the numerical algorithm used in this work to find the stationary solution of the master equation, we finally present our transport formalism on the basis of a short example.

In Chapter 4 we discuss the possible appearance of NDC in electronic transport through CuPc, caused by many-body interference between orbitally degenerate many-body states. To this end we set up a minimal model containing only the relevant physics. Furthermore, we explain the mechanism leading to the interference blocking scenario and identify the spectroscopic and topographical footprints of this many-body effect. We finally conclude the chapter by discussing the stability of the interference NDC.

We dedicate Chapter 5 to the description of an effect termed nonequilibrium spin-crossover, which is a phenomenon during which the CuPc molecule can undergo a transition to different spin states, depending on the position of the tip. We provide a simple pedagogical example to show that this effect is caused by population inversion to excited neutral states of the molecule. In the last part of Chapter 5 we finally give

general constraints on molecular properties like electron affinity, ionization potential and the optical gap to narrow down classes of molecules that could possibly exhibit such many-body effects.

In Chapter 6 we add spin-orbit interaction (SOI) and interaction with magnetic fields to the description of CuPc. Furthermore, we derive an effective low-energy Hamiltonian for CuPc. In magnetotransport measurements the anisotropic properties of CuPc are revealed and the effective Hamiltonian is used to gather information about the different transitions showing up in the magnetotransport calculations.

Finally, we conclude our work in chapter 7 and provide a list of possible extensions of this thesis in the hope of stimulating continuation of this work.

2

MANY-BODY HAMILTONIANS FOR π-CONJUGATED MOLECULES

The most important ingredient in the calculation of transport properties of molecules in whatever junction geometry surely is the molecular Hamiltonian. Since many-particle problems scale exponentially with their degrees of freedom - a quantum mechanical system with only ten different "pots" to allocate electrons has already over one million different electronic configurations - one has to come up with a clever scheme to tackle such intricate problems.

In this chapter we derive a semiempirical model Hamiltonian for π-conjuated molecules, specifically on the example of CuPc. By using our procedure as a guideline it should be possible to extend the model to further molecules, in particular to other members of the MPc family.

2.1 A GENERAL MANY-BODY HAMILTONIAN

The most general Hamiltonian for a molecule consisting of N_e electrons and N_n nuclei reads

$$\hat{H}_\mathrm{mol} = \hat{T}_\mathrm{e} + \hat{T}_\mathrm{n} + \hat{V}_\mathrm{en} + \hat{V}_\mathrm{ee} + \hat{V}_\mathrm{nn}, \tag{2.1}$$

which is composed of the electronic kinetic energy,

$$\hat{T}_\mathrm{e} = \sum_{i=1}^{N_\mathrm{e}} \frac{\hbar^2}{2m_\mathrm{e}} \boldsymbol{\nabla}_i^2, \tag{2.2}$$

the kinetic energy of the nuclei with masses M_α positioned at $\mathbf{r}_\alpha$,

$$\hat{T}_\mathrm{n} = \sum_{\alpha=1}^{N_\mathrm{n}} \frac{\hbar^2}{2M_\alpha} \boldsymbol{\nabla}_\alpha^2, \tag{2.3}$$

the Coulomb interaction between electrons and nuclei,

$$\hat{V}_\mathrm{en} = -\sum_{i=1}^{N_\mathrm{e}} \sum_{\alpha=1}^{N_\mathrm{n}} \frac{Z_\alpha e^2}{4\pi\varepsilon_0 r_{i\alpha}}, \tag{2.4}$$

where $r_{i\alpha} = |\mathbf{r}_i - \mathbf{r}_\alpha|$, the Coulomb interaction between electrons,

$$\hat{V}_\mathrm{en} = \frac{1}{2} \sum_{i=1}^{N_\mathrm{e}} \sum_{\substack{j=1 \\ j\neq i}}^{N_\mathrm{e}} \frac{e^2}{4\pi\varepsilon_0 r_{ij}}, \tag{2.5}$$

and finally the Coulomb interaction between the nuclei,

$$\hat{V}_\mathrm{nn} = \frac{1}{2} \sum_{\alpha=1}^{N_\mathrm{n}} \sum_{\substack{\beta=1 \\ \beta\neq\alpha}}^{N_\mathrm{n}} \frac{Z_\alpha Z_\beta e^2}{4\pi\varepsilon_0 r_{\alpha\beta}}, \tag{2.6}$$

with Z_α being the proton number of atom α. Solving Eq. (2.1) means dealing with an $N_\mathrm{n} + N_\mathrm{e}$-particle problem: the total wavefunction Ψ_tot describes the motion of all nuclei and electrons at the same time. A commonly used simplification of this problem is the Born-Oppenheimer approximation [BO27], under which the electronic and nuclear degrees of freedom are decoupled, $\Psi_\mathrm{tot} = \Psi_\mathrm{n}\left(\{\mathbf{r}_\alpha\}\right) \times \Psi_\mathrm{e}\left(\{\mathbf{r}_\alpha\}, \{\mathbf{r}_i\}\right)$. The justification of this approximation is based on the huge mass difference between electrons and nuclei, leading to a movement of electrons on a much shorter timescale than the nuclei. Thus for the electrons the nuclei are essentially frozen, while from the nuclear point of view the electrons are generating an energy landscape (PES, potential energy surface [Jen99]) whose minima and curvature ultimately determine the rest positions and vibrational motions of the nuclei, respectively.

Since our main interest in this work lies in the description of electronic effects, we assume the nuclei to be fully frozen; that is, we neglect vibrational excitations of the molecule.

2.1.1 *Molecular Hamiltonian in the atomic basis*

After exploiting the Born-Oppenheimer approximation and freezing the nuclear motion, we write Eq. (2.1) in second quantization:

$$\begin{aligned}\hat{H}_\mathrm{mol} = &\sum_{\substack{\alpha\beta\\mn}}\sum_{\sigma\sigma'} \langle \alpha m\sigma| \frac{\hat{\mathbf{p}}^2}{2m_\mathrm{e}} + \sum_\gamma \hat{V}_\gamma \,|\beta n\sigma'\rangle \; \hat{d}^\dagger_{\alpha m\sigma}\hat{d}_{\beta n\sigma'} \\ &+ \frac{1}{2}\sum_{\substack{\alpha\beta\gamma\delta\\mnpq}}\sum_{\sigma\sigma'} V^{mnpq}_{\alpha\beta\gamma\delta}\, \hat{d}^\dagger_{\alpha m\sigma}\hat{d}^\dagger_{\gamma p\sigma'}\hat{d}_{\delta q\sigma'}\hat{d}_{\beta n\sigma},\end{aligned} \tag{2.7}$$

where $\hat{d}^\dagger_{\alpha m\sigma}$ creates an electron in the atomic orbital $|\alpha m\sigma\rangle$ with quantum numbers m, σ centered at atom α:

$$\langle \mathbf{r}\sigma'|\alpha m\sigma\rangle = \phi_{\alpha m}(\mathbf{r})\delta_{\sigma\sigma'}. \tag{2.8}$$

In the following, we omit spin indices when they are not explicitly required. The operator $\hat{V}_\gamma$ denotes the nuclear potential of atom γ at position $\mathbf{r}_\gamma$, cf. Eq. (2.4), and finally $V^{mnpq}_{\alpha\beta\gamma\delta}$ is the matrix element of the Coulomb interaction $V(r) = \frac{e^2}{4\pi\varepsilon_0 r}$,

$$V^{mnpq}_{\alpha\beta\gamma\delta} = \int \mathrm{d}^3r_1\mathrm{d}^3r_2\, \phi^*_{\alpha m}(\mathbf{r}_1)\, \phi_{\beta n}(\mathbf{r}_1)\, V\left(r_{12}\right)\, \phi^*_{\gamma p}(\mathbf{r}_2)\, \phi_{\delta q}(\mathbf{r}_2), \tag{2.9}$$

where $r_{12} = |\mathbf{r}_1 - \mathbf{r}_2|$. A more convenient form of writing the single particle part in Eq. (2.7) is

$$\hat{H}^{(1)}_\mathrm{mol} = \sum_{\substack{\alpha\beta\\mn}} \left(h_{\alpha m,\beta n} + V^\mathrm{ion}_{\alpha m,\beta n}\right) \hat{d}^\dagger_{\alpha m}\hat{d}_{\beta n}, \tag{2.10}$$

where

$$V^\mathrm{ion}_{\alpha m,\beta n} = \sum_\gamma^{\gamma\neq\alpha,\beta} \langle \alpha m|\hat{V}_\gamma|\beta n\rangle \tag{2.11}$$

is the crystal field correction to the single particle Hamiltonian, and

$$h_{\alpha m,\beta n} = \epsilon_{\alpha m}\delta_{\alpha\beta}\delta_{mn} + b_{\alpha m,\beta n}. \tag{2.12}$$

is the matrix representation of the single particle Hamiltonian with onsite energies $\epsilon_{\alpha m}$ and hopping integrals $b_{\alpha m,\beta n}$, see App. A.1.

For planar π-electron systems a prominent way to set up $h_{\alpha m,\beta n}$ is the Hückel method [Hue31]. In the case of benzene, $h_{\alpha m,\beta n}$ would be parametrized using only two parameters a and b with $\epsilon_{\alpha m} = a$ and $b_{\alpha m,\beta n} = b$ for nearest neighbours, yielding eigenenergies $E(l) = a + 2b\cos\frac{2\pi l}{6}$ $(|l| = 0, 1, 2, 3)$ which can be fitted to experimental data coming from e.g. photoelectron spectroscopy [CF67] or electronic absorption spectroscopy [Skl42]. For more complicated molecules and where the σ-system has to be considered, the Slater-Koster linear combination of atomic orbitals (LCAO) scheme [SK54] can be used: Here, the hopping integrals are expressed as

$$b_{\alpha m,\beta n} = \sum_{\xi} V_{\ell\ell'\xi}(r_{\alpha\beta}) f_{\xi}(\varphi_{\alpha\beta}), \tag{2.13}$$

where ℓ and ℓ' denote the subshells (s, p, d, f,...) of orbitals $|\alpha m\rangle$ and $|\beta n\rangle$, respectively, and $\xi = \sigma, \pi, \delta$ is the character of the bond, which is roughly given by the number of overlapping lobes (one, two or four) of the participating orbitals; for example a bond between two p_x orbitals aligned along the y-axis is a pure π-bond, while it is has pure σ-character if the two p_x orbitals are aligned along the x-axis. Thus a general bond can have more than one distinct character. The $V_{\ell\ell'\xi}(r_{\alpha\beta})$ depend on the distance $r_{\alpha\beta}$ and can be parametrized using the method of Harrison [FH79], while the $f_{\xi}(\varphi_{\alpha\beta})$ depend only on the angle $\varphi_{\alpha\beta}$ of the bond vector $\mathbf{r}_{\alpha\beta} = \mathbf{r}_{\beta} - \mathbf{r}_{\alpha}$ with respect to the different coordinate axes and can be foundin Slater's paper [SK54]. As a short example, the hopping integral between a p_y orbital at position $\mathbf{r}_1$ and a p_x orbital at position $\mathbf{r}_2$ is given by

$$b_{1\mathrm{p}_y,2\mathrm{p}_x} = V_{\mathrm{pp}\sigma}\cos\varphi_{12,x}\cos\varphi_{12,y} - V_{\mathrm{pp}\pi}\cos\varphi_{12,x}\cos\varphi_{12,y}, \tag{2.14}$$

where $\varphi_{12,i} = \angle(\mathbf{r}_{12}, \hat{\mathbf{e}}_i)$ is the angle between the bond vector and the unit vector $\hat{\mathbf{e}}_i$ of the Cartesian coordinate system.

2.1.2 *The molecular orbital basis*

The $h_{\alpha m,\beta n}$ in Eq. 2.12 are elements of a matrix $\mathbf{h}$ which corresponds to the single particle Hamiltonian of the molecule with only onsite energies and hopping terms. Since $|\alpha m\rangle$ and $|\beta n\rangle$ can be centered on different atoms, they are in general not orthogonal. Instead they have a finite overlap $S_{\alpha m,\beta n} = \langle\alpha m|\beta n\rangle$. In this work, though, we assume $S_{\alpha m,\beta n}$ to be negligible. This was also checked in numerical tests and we found no qualitative differences. After using the approximation that the basis $|\alpha m\rangle$ is orthogonal,

$$\langle\alpha m|\beta n\rangle = \delta_{\alpha\beta}\delta_{mn}, \tag{2.15}$$

diagonalizing $\mathbf{h}$ yields the molecular orbital (MO) basis,

$$\psi_i(\mathbf{r}) = \langle \mathbf{r}|i\rangle = \sum_{\alpha m} c_{i\alpha m}\ \langle \mathbf{r}|\alpha m\rangle\,. \tag{2.16}$$

Then the Hamiltonian in Eq. (2.7) reads:

$$\begin{aligned}\hat{H}_{\mathrm{mol}} &= \sum_{ij\sigma}\left(\epsilon_i\delta_{ij} + V_{ij}^{\mathrm{ion}}\right)\ \hat{d}_{i\sigma}^{\dagger}\hat{d}_{j\sigma} \\ &+\frac{1}{2}\sum_{ijkl}\sum_{\sigma\sigma'} V_{ijkl}\,\hat{d}_{i\sigma}^{\dagger}\hat{d}_{k\sigma'}^{\dagger}\hat{d}_{l\sigma'}\hat{d}_{j\sigma}.\end{aligned} \tag{2.17}$$

The ϵ_i are the single particle eigenenergies and V_{ij}^{ion} is given by

$$V_{ij}^{\mathrm{ion}} = \sum_{\substack{\alpha\beta\\ mn}} c_{i\alpha m}^{*} c_{j\beta n}\, V_{\alpha m,\beta n}^{\mathrm{ion}}. \tag{2.18}$$

Finally, we have the matrix element of the Coulomb interaction in the molecular orbital basis,

$$V_{ijkl} = \int \mathrm{d}^3 r_1 \int \mathrm{d}^3 r_2\, \psi_i^{*}(\mathbf{r}_1)\psi_j(\mathbf{r}_1)\, V(r_{12})\, \psi_k^{*}(\mathbf{r}_2)\psi_l(\mathbf{r}_2). \tag{2.19}$$

This basis brings along some advantages: The resulting eigenenergies often grasp rather well the realistic order of the molecular orbitals, so that their occupations follow the Aufbau principle analogous to filling up atomic shells. This is the case for example in the metal-free phthalocyanine H_2Pc [SDG13]. Furthermore, a huge simplification which is possible in the MO basis, is the reduction of the size of our Hilbert space $\mathcal{H}$, which occurs by retaining few relevant MOs only. To this end, we split the full MO basis into frozen and dynamic orbitals, where N_f of the frozen orbitals are assumed to be always fully occupied and the remaining N_e set to be always empty. We do not make any assumption about the occupation of the N_d dynamic states. Whether these N_d frontier orbitals are full or empty depends on the electrochemical potential of the molecule, and on whether an exchange of electrons with the environment is possible. Then, in the occupation number representation a general state of the Fock space looks like

$$|\Psi\rangle \approx \underbrace{|11\ldots11\rangle}_{2N_f} \otimes \underbrace{|n_{k\uparrow}n_{k\downarrow}\ldots n_{l\uparrow}n_{l\downarrow}\rangle}_{2N_d} \otimes \underbrace{|00\ldots00\rangle}_{2N_e}\,. \tag{2.20}$$

Last but not least, the symmetry properties of the molecular orbitals can be used to narrow down the required number of matrix elements V_{ijkl} of the Coulomb interaction and V_{ij}^{ion} of the crystal field correction. We will illustrate this in the following section by the example of CuPc.

2.2 THE HAMILTONIAN OF COPPER PHTHALOCYANINE

We now discuss the construction of the many-body model Hamiltonian of CuPc. This molecule has 195 valence electrons stemming from the

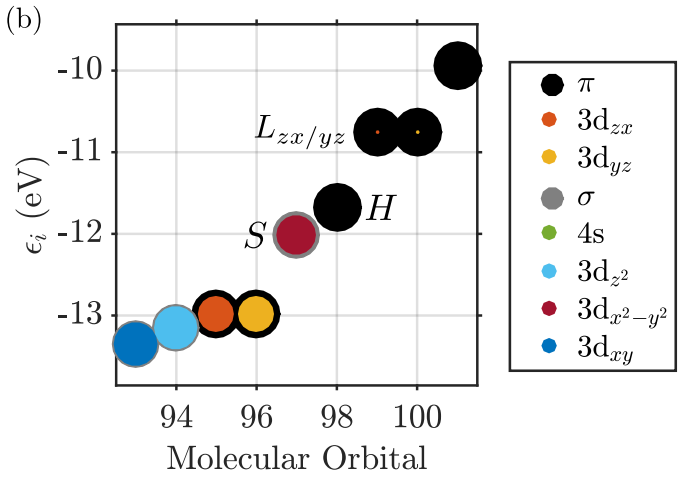

Figure 2.1: Cutout of the single particle spectrum of CuPc around the positions of the relevant molecular orbitals. Black (grey) circles depict the π (σ) character of the corresponding orbital. The color (diameter) of the inner circles characterizes the type (weight) of the metal orbital contribution on the corresponding molecular orbital. S, H and $L_{zx/yz}$ denote the energies of the SOMO, HOMO and the two LUMOs, respectively.

1s, 2s and 2p orbitals on the ligand and from the 3d and 4s orbitals on the copper center. Due to the odd number of valence electrons, the filling of the MOs according to the Aufbau principle is not straightforward, because a priori we have no hints about which MO to leave singly occupied. Thus a many-body description which includes inter- and intra-molecular orbital interactions is required.

2.2.1 *The single particle spectrum*

As shown in Sec. 2.1.1, the matrix representing the single particle Hamiltonian in Eq. (2.10) in the atomic basis $|\alpha m\rangle$ reads

$$h_{\alpha m,\beta n} = \epsilon_\alpha \delta_{\alpha\beta}\delta_{mn} + b_{\alpha m,\beta n}. \tag{2.21}$$

For the ligand we consider the set of all 2s (1s for hydrogen), $2p_x$ and $2p_y$ orbitals as the σ-system, and consequently the set of $2p_z$ orbitals as the π-system. On the metal, the $3d_{xy}$, $3d_{x^2-y^2}$, $3d_{z^2}$ and 4s orbitals contribute to the σ-system, while the $3d_{zx}$ and $3d_{yz}$ belong to the π-system. Atomic onsite energies ϵ_α and geometrical parameters are taken from Refs. [Man67, LS01]. The hopping matrix elements $b_{\alpha\beta}$ in Eq. (2.21) are obtained by using the Slater-Koster [SK54] and Harrison [FH79] LCAO schemes, which already were presented in Sec. 2.1.1. Numerical diagonalization of $\mathbf{h}$ finally yields single particle energies ϵ_i, see Fig. 2.1, and MOs $|i\rangle = \sum_\alpha c_{i\alpha} |\alpha\rangle$.

Intuitively, despite the odd number of valence electrons, the highest occupied molecular orbital (HOMO) should be one of the orbitals Nr.

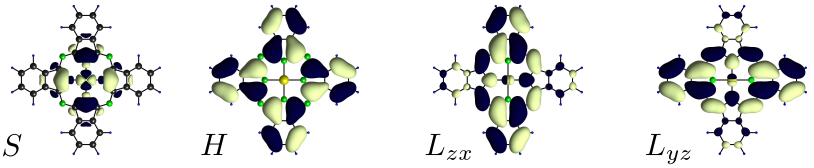

Figure 2.2: Depiction of the four frontier orbitals of CuPc: SOMO (S), HOMO (H) and LUMO$_{zx/yz}$ ($L_{zx/yz}$).

97 or 98, see Fig. 2.1. By comparing our eigenstates (cf. Fig 2.2) to the literature [ECS+07, dOESGL+10, CFN07, LS01] we can infer that the orbitals 97 to 100 in Fig. 2.1 build up the set of frontier orbitals, in CuPc, i.e. the set of orbitals most relevant in transport. We thus choose the set of these orbitals to build up the subspace of dynamic orbitals, see Eq. (2.20), resulting in double filling of the lower 96 MOs. Hence, for neutral CuPc the number of electrons populating the frontier orbitals is $N_0 = 3$.

Without any prior assumption about the occupations of the frontier orbitals we stick to the naming convention given in the literature, thus in the rest of this work we will call them SOMO, HOMO and LUMO$_{zx/yz}$. These names are easier to grasp than the other alternative for naming them, which is denoting them by the irreducible representations of D_{4h}, which are the b_{1g}, a_{1u} and e_g representations for the singly occupied molecular orbital (SOMO), the HOMO and the two lowest unoccupied molecular orbitals (LUMOs), respectively.

Also shown in Fig. 2.1 are the quite distinct contributions of the frontier orbitals on the copper center. While the SOMO is largely concetrated on the metal, the degenerate LUMOs have small contributions and the HOMO is a pure ligand orbital. This can be nicely seen in the real space representations of the molecular orbitals in Fig. 2.2. The LUMO orbitals, $|L_{zx}\rangle$ and $|L_{yz}\rangle$, have equal contributions $c_L \approx 0.097$ on either $3\mathrm{d}_{zx}$ and $3\mathrm{d}_{yz}$ orbitals on the metal, respectively:

$$|L_{zx/yz}\rangle = \sqrt{1-c_L^2}\,|L_{zx/yz}\rangle_{\mathrm{Pc}} + c_L\,|3\mathrm{d}_{zx/yz}\rangle_{\mathrm{Cu}}\,. \tag{2.22}$$

To distinguish contributions from the pure phthalocyanine (Pc) ligand and the copper (Cu) center, we introduced $|\cdot\rangle_{\mathrm{Pc}}$ and $|\cdot\rangle_{\mathrm{Cu}}$, respectively. Likewise, with $c_S \approx 0.90$, we can write for the SOMO:

$$|S\rangle = \sqrt{1-c_S^2}\,|S\rangle_{\mathrm{Pc}} + c_S\,|3\mathrm{d}_{x^2-y^2}\rangle_{\mathrm{Cu}}\,. \tag{2.23}$$

Finally, the HOMO has no metal contributions and thus we have trivially $|H\rangle = |H\rangle_{\mathrm{Pc}}$. The single particle eigenenergies of the frontier orbitals are $\epsilon_S = -12.0$ eV, $\epsilon_H = -11.7$ eV and $\epsilon_{L\pm} = -10.7$ eV.

Before we continue with setting up the many-body Hamiltonian of CuPc, we discuss the symmetry properties of the four frontier orbitals and their implications on the matrix elements of the Hamiltonian.

2.2.2 *A short detour to group theory*

CuPc belongs to the point group D_{4h} (order 16), which itself is a product group of the dihedral group D_4 of order 8 and the group of inversions S_2 of order 2, thus $D_{4h} = D_4 \otimes S_2$. This fact can be exploited heavily, because the eigenstates of the Hamiltonian have to transform under action of the group elements of D_{4h} in the same way as its irreducible representations. Moreover, matrix elements of operators of the group between wavefunctions of different irreducible representations will vanish exactly [Tin64]. To examine the properties of the group D_{4h}, we first start with its subgroup D_4. It contains four rotations around the principal axis and four reflections in the plane. All elements of the group can be set up through the generators of the group: the identity e, the counterclockwise rotation of $\frac{\pi}{2}$ around the principal axis, g, and the rotation of π around an axis in the plane joining two vertices of the square, h. The element gh describes a rotation of π around axes bisecting two opposing edges. The point group D_4 has five irreducible representations, four of them are one-dimensional and one is two-dimensional. The character $\chi_A(g)$ of a representation A of a given group element g is defined as the trace of its matrix representation. From the character table (see Table 2.1) the rotational properties of the irreducible representations of D_4 can be read out at one glance, at least for the one-dimensional representations:

1. A_1 is invariant under any rotation;
2. A_2 is invariant under rotations around the principal axis, and changes sign under rotations around in-plane symmetry axes;
3. B_1 changes sign under g, is invariant under h, and changes sign under gh;
4. B_2 changes sign under g and h and is thus invariant under gh.

In fact, regarding the one-dimensional representations, the characters are displaying the eigenvalues of the group elements, while the irreducible representations are the corresponding eigenvectors. For the two-dimensional representation the characters yield the traces of its representation matrices and thus the sum of their eigenvalues. For the element g we have $\chi_E(g) = 0$, thus its eigenvalues must differ in their signs. Together with the character for g^2, $\chi_E(g^2) = -2$, we are immediately able to give the diagonal elements of the two-dimensional matrix representation of E, as for any diagonal two-dimensional matrix M it holds that from $tr(M) = 0$ and $tr(M^2) = -2$ its diagonal elements follow as $M_{11} = \pm i$ and $M_{22} = -M_{11}$.

2.2.2.1 *"Bloch's theorem" in rotational symmetric molecules*

Consider the Hamiltonian of a molecule belonging to the point group $D_{4(h)}$. It is invariant under the rotation of $\frac{\pi}{2}$ around the principal axis

#	1	2	1	2	2
	e	g	g^2	h	gh
A_1	1	1	1	1	1
A_2	1	1	1	-1	-1
B_1	1	-1	1	1	-1
B_2	1	-1	1	-1	1
E	2	0	-2	0	0

Table 2.1: Character table of the point group D_4.

of the system, described by the operator $R_{\frac{\pi}{2}}$, which is equivalent to the generator g of the group $D_{4(h)}$ and cycles through the unit cells of CuPc. Its properties are:

$$R_{\frac{\pi}{2}} \cdot f(\varphi,(\vartheta,r)) = f(\varphi+\tfrac{\pi}{2},(\vartheta,r)), \tag{2.24}$$

$$\begin{aligned}\left(R_{\frac{\pi}{2}}\right)^n \cdot f(\varphi) &= \left(R_{\frac{\pi}{2}}\right)^{n-1} \cdot f(\varphi+\tfrac{\pi}{2}) = \dots \\ &= f(\varphi + n\cdot\tfrac{\pi}{2}) \\ &= R_{\frac{n\pi}{2}} \cdot f(\varphi),\end{aligned} \tag{2.25}$$

$$R_{\frac{\pi}{2}} \cdot H(\varphi) = H(\varphi+\tfrac{\pi}{2}) = H(\varphi). \tag{2.26}$$

Applying $R_{\frac{\pi}{2}}$ to both sides of $H\psi = E\psi$ yields:

$$R_{\frac{\pi}{2}} \cdot (H\psi) = H(\varphi+\tfrac{\pi}{2})\psi(\varphi+\tfrac{\pi}{2}) = H(\varphi)\psi(\varphi+\tfrac{\pi}{2}), \tag{2.27}$$

$$R_{\frac{\pi}{2}} \cdot (E\psi(\varphi)) = E\psi(\varphi+\tfrac{\pi}{2}). \tag{2.28}$$

Thus $R_{\frac{\pi}{2}}\psi$ is also an eigenstate of the Hamiltonian with the same energy E, but ψ is not necessarily invariant under the action of $R_{\frac{\pi}{2}}$. However, since $[H, R_{\frac{\pi}{2}}] = 0$, there exists a complete orthogonal set of mutual eigenstates Ψ of both operators:

$$H\Psi_i(\varphi) = E_i\Psi_i(\varphi), \tag{2.29}$$

$$R_{\frac{\pi}{2}}\Psi_i(\varphi) = \Psi_i(\varphi+\tfrac{\pi}{2}) = \lambda_i\Psi_i(\varphi). \tag{2.30}$$

The absolute value of λ_i must equal unity as well as λ_i^4, since

$$|\lambda_i|^2 = ||R_{\frac{\pi}{2}}\Psi_i(\varphi)||^2 = ||\Psi_i(\varphi+\tfrac{\pi}{2})||^2 = 1, \tag{2.31}$$

$$\lambda_i^4\Psi_i(\varphi) = R_{2\pi}\Psi_i(\varphi) = \Psi_i(\varphi+2\pi) = \Psi_i(\varphi). \tag{2.32}$$

Accordingly, λ_i has the form $\lambda_i = \mathrm{e}^{i\frac{\pi}{2}\ell_i}$ with $\ell_i \in \mathbb{Z}$. To obtain the exact values of ℓ_i we have to take a look at the character table of D_4, since the λ_i are the eigenvalues of the generator g with respect

to a given one-dimensional representation, i.e. eigenstate Ψ_i. In two dimensional representations the λ_i can be read out from the diagonal representation. For the one-dimensional representations of type A the characters are $\chi_A(g) = 1$ and $\chi_A(g^2) = 1$, thus $\ell_A = 0 \pmod 4$ for wavefunctions transforming according to these representations. The other one-dimensional representations have characters $\chi_B(g) = -1$ and $\chi_B(g^2) = 1$, yielding

$$-1 = \lambda_B = \mathrm{e}^{i\frac{\pi}{2}\ell_B} \Rightarrow \ell_B = 2 \pmod 4. \tag{2.33}$$

Having $\chi_E(g) = 0$ and $\chi_E(g^2) = -2$ for the two-dimensional representations we get

$$0 = \lambda_{E,1} + \lambda_{E,2} = \mathrm{e}^{i\frac{\pi}{2}\ell_{E,1}} + \mathrm{e}^{i\frac{\pi}{2}\ell_{E,2}}, \tag{2.34}$$

$$-2 = \lambda_{E,1}^2 + \lambda_{E,2}^2 = \mathrm{e}^{i\pi\ell_{E,1}} + \mathrm{e}^{i\pi\ell_{E,2}}, \tag{2.35}$$

$$\Rightarrow \ell_{E,1/2} = \pm 1. \tag{2.36}$$

Thus we have shown that for each orbital Ψ_i of a molecule belonging to the point group $D_{4(h)}$ there exists a number ℓ_i so that

$$\Psi_i(r, \vartheta, \varphi + \tfrac{\pi}{2}) = \mathrm{e}^{i\frac{\pi}{2}\ell_i}\Psi_i(r, \vartheta, \varphi), \tag{2.37}$$

analogous to Bloch's theorem for wavefunctions in crystals. Because of this we can attribute to them some sort of pseudo angular momentum to ℓ_i (pseudo angular momentum). On the basis of this example this concept can be carried on to other point groups with discrete rotational symmetry.

2.2.2.2 *A short example*

Consider the following Hamiltonian of a fictitious molecule, consisting of four atoms with p_z-orbitals arranged in a square symmetry around one central pair of zx- and yz-orbitals:

$$\hat{H} = \begin{pmatrix} \hat{H}_\pi & \hat{H}_{\mathrm{M}\pi}^\dagger \\ \hat{H}_{\mathrm{M}\pi} & \hat{H}_{\mathrm{M}} \end{pmatrix}, \tag{2.38}$$

where $\hat{H}_\pi$ is the Hamiltonian of the four p_z-orbitals,

$$\hat{H}_\pi = \begin{pmatrix} \epsilon & \beta & 0 & \beta \\ \beta & \epsilon & \beta & 0 \\ 0 & \beta & \epsilon & \beta \\ \beta & 0 & \beta & \epsilon \end{pmatrix}, \tag{2.39}$$

with $\beta < 0$ and $\hat{H}_{\mathrm{M}} = \left(\begin{smallmatrix} \epsilon_M & 0 \\ 0 & \epsilon_M \end{smallmatrix}\right)$ is the Hamiltonian of the central metal orbitals. The Hamiltonian which describes the hopping between "ligand" and metal reads:

$$\hat{H}_{\mathrm{M}\pi} = \begin{pmatrix} -t & 0 & t & 0 \\ 0 & -t & 0 & t \end{pmatrix}. \tag{2.40}$$

The generators of D_4 written in the basis of the four p_z orbitals read:

$$g = \begin{pmatrix} 0 & 1 & 0 & 0 \\ 0 & 0 & 1 & 0 \\ 0 & 0 & 0 & 1 \\ 1 & 0 & 0 & 0 \end{pmatrix}, \qquad h = \begin{pmatrix} 0 & 0 & -1 & 0 \\ 0 & -1 & 0 & 0 \\ -1 & 0 & 0 & 0 \\ 0 & 0 & 0 & -1 \end{pmatrix}. \tag{2.41}$$

The matrix g describes a rotation of $\frac{\pi}{2}$ around the z-axis and cycles through the locations of the p_z-orbitals, and h displays a rotation around an in-plane axis connecting two atoms through the center. All its non-zero elements are negative, since under an in-plane rotation p_z-orbitals are changing their signs. We now diagonalize $\hat{H}_\pi$ and classify the molecular orbitals by means of their transformation properties. The molecular orbitals in the real basis are:

$$\psi_0 = \frac{1}{2}\begin{pmatrix} 1 \\ 1 \\ 1 \\ 1 \end{pmatrix}, \qquad \psi_a = \frac{1}{\sqrt{2}}\begin{pmatrix} 1 \\ 0 \\ -1 \\ 0 \end{pmatrix},$$

$$\psi_2 = \frac{1}{2}\begin{pmatrix} -1 \\ 1 \\ -1 \\ 1 \end{pmatrix}, \qquad \psi_b = \frac{1}{\sqrt{2}}\begin{pmatrix} 0 \\ 1 \\ 0 \\ -1 \end{pmatrix}, \tag{2.42}$$

with energies $\epsilon_0 = \epsilon + 2\beta$, $\epsilon_{a/b} = \epsilon$ and $\epsilon_2 = \epsilon - 2\beta$. Now we express g and h in the basis $\{\psi_0,\psi_a,\psi_b,\psi_2\}$:

$$\tilde{g} = \begin{pmatrix} 1 & 0 & 0 & 0 \\ 0 & 0 & 1 & 0 \\ 0 & -1 & 0 & 0 \\ 0 & 0 & 0 & -1 \end{pmatrix}, \quad \tilde{h} = \begin{pmatrix} -1 & 0 & 0 & 0 \\ 0 & 1 & 0 & 0 \\ 0 & 0 & -1 & 0 \\ 0 & 0 & 0 & -1 \end{pmatrix}. \tag{2.43}$$

Apparently ψ_0 and ψ_2 transform like A_2 ($\ell_A = 0$) and B_2 ($\ell_B = 2$), respectively. The states ψ_a and ψ_b seem to transform according to the E representation. Diagonalizing this subblock yields the states ψ_+ and ψ_-, with

$$\psi_\pm = \mp\frac{1}{\sqrt{2}}\left(\psi_a \pm i\,\psi_b\right), \quad \ell_\pm = \pm 1. \tag{2.44}$$

We represent g and h in the basis of the metal orbitals $\{\psi^M_\pm\}$,

$$\bar{g} = \begin{pmatrix} 0 & 1 \\ -1 & 0 \end{pmatrix}, \qquad \bar{h} = \begin{pmatrix} -1 & 0 \\ 0 & 1 \end{pmatrix}. \tag{2.45}$$

The basis $\psi_{\pm}^{M} = \mp\frac{1}{\sqrt{2}}(\psi_{zx} \pm i\psi_{yz})$ with pseudo angular momenta $\ell_{\pm} = \pm 1$ renders $\bar{g}$ diagonal. Reexpressing $\hat{H}_{\mathrm{M}\pi}$ in this basis gives

$$\hat{H}'_{\mathrm{M}\pi} = \begin{pmatrix} 0 & -\sqrt{2}t & 0 & 0 \\ 0 & 0 & -\sqrt{2}t & 0 \end{pmatrix}, \tag{2.46}$$

thus yielding the complete Hamiltonian

$$\hat{H} = \begin{pmatrix} \epsilon + 2\beta & 0 & 0 & 0 & 0 & 0 \\ 0 & \epsilon & 0 & 0 & -\sqrt{2}t & 0 \\ 0 & 0 & \epsilon & 0 & 0 & -\sqrt{2}t \\ 0 & 0 & 0 & \epsilon - 2\beta & 0 & \\ 0 & -\sqrt{2}t & 0 & 0 & \epsilon_M & 0 \\ 0 & 0 & -\sqrt{2}t & 0 & 0 & \epsilon_M \end{pmatrix}. \tag{2.47}$$

Notice that only MOs of the E representation are coupling to the metal orbitals, further that only states with equal pseudo angular momenta have non vanishing matrix elements. Thus ψ_0 and ψ_2 are also representing eigenstates of the full Hamiltonian. For the reduced Hamiltonian $\hat{H}'$, which was projected onto the basis $\{\psi_-, \psi_+, \psi_-^M, \psi_+^M\}$,

$$\hat{H}' = \sqrt{2}t \begin{pmatrix} \bar{\epsilon} - \delta & 0 & -1 & 0 \\ 0 & \bar{\epsilon} - \delta & 0 & -1 \\ -1 & 0 & \bar{\epsilon} + \delta & 0 \\ 0 & 1 & 0 & \bar{\epsilon} + \delta \end{pmatrix}, \tag{2.48}$$

where $\bar{\epsilon} - \delta = \epsilon/\sqrt{2}t$ and $\bar{\epsilon} + \delta = \epsilon_M/\sqrt{2}t$, we find the following eigensystem:

$$\psi_1^+ = \frac{1}{\sqrt{1+\lambda^2}} \begin{pmatrix} 0 \\ \lambda \\ 0 \\ 1 \end{pmatrix}, \qquad \psi_2^+ = \frac{1}{1+\lambda^2} \begin{pmatrix} 1 \\ 0 \\ \lambda \\ 0 \end{pmatrix},$$

$$\psi_1^- = \frac{1}{\sqrt{1+\lambda^2}} \begin{pmatrix} -\lambda \\ 0 \\ 1 \\ 0 \end{pmatrix}, \qquad \psi_2^- = \frac{1}{\sqrt{1+\lambda^2}} \begin{pmatrix} 0 \\ -1 \\ 0 \\ \lambda \end{pmatrix},$$

$$\epsilon_1^{\pm} = \bar{\epsilon} - \sqrt{1+\delta^2}, \qquad \epsilon_2^{\pm} = \bar{\epsilon} + \sqrt{1+\delta^2}. \tag{2.49}$$

Here, $\lambda = \delta + \sqrt{1+\delta^2}$. Thus for each pair of states $\psi_1^{\pm}$ there exists another pair $\psi_2^{\pm}$ with higher energy and inverse weight on the metal center.

2.2.3 *Symmetries in the frontier orbital basis*

Following the short example given in Sec. 2.2.2.2, we can make linear combinations of the two degenerate LUMO orbitals $|L_{zx/yz}\rangle$ to rep-

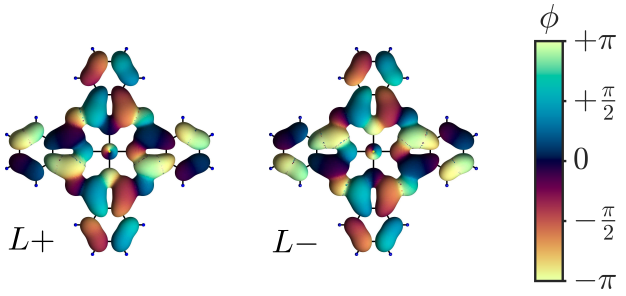

Figure 2.3: The LUMO orbitals of CuPc in their rotationally invariant representation. The color denotes the complex phase of the orbitals.

resent them in their complex, rotationally invariant basis $|L\pm\rangle$, see Fig. 2.3:

$$\begin{aligned}|L\pm\rangle &= \mp 2^{-1/2}\left(|L_{zx}\rangle \pm i\,|L_{yz}\rangle\right)\\ &= \mp 2^{-1/2}\sqrt{1-c_L^2}\left(|L_{zx}\rangle_{\mathrm{Pc}} \pm i\,|L_{yz}\rangle_{\mathrm{Pc}}\right)\\ &\quad \mp 2^{-1/2}\,c_L\left(|3\mathrm{d}_{zx}\rangle_{\mathrm{Cu}} \pm i\,|3\mathrm{d}_{yz}\rangle_{\mathrm{Cu}}\right)\\ &= \sqrt{1-c_L^2}\;|L\pm\rangle_{\mathrm{Pc}} + c_L\,|3,2,\pm1\rangle_{\mathrm{Cu}}\,, \end{aligned} \tag{2.50}$$

where $|3,2,\pm1\rangle_{\mathrm{Cu}}$ is the $n=3$ metal orbital with angular momentum $\ell=2$ and magnetic quantum number $m=\pm1$. Analogously, we can write for the SOMO:

$$\begin{aligned}|S\rangle &= \sqrt{1-c_S^2}\;|S\rangle_{\mathrm{Pc}} + c_S\,|3\mathrm{d}_{x^2-y^2}\rangle_{\mathrm{Cu}}\\ &= \sqrt{1-c_S^2}\;|S\rangle_{\mathrm{Pc}} + 2^{-1/2}\,c_S\left(|3,2,-2\rangle_{\mathrm{Cu}} + |3,2,2\rangle_{\mathrm{Cu}}\right), \end{aligned} \tag{2.51}$$

where $|3,2,\pm2\rangle_{\mathrm{Cu}}$ is the $n=3$ metal orbital with angular momentum $\ell=2$ and projection $m=\pm2$ onto the z-axis. Expressing the frontier orbitals in their rotationally invariant representations has the advantage that they can be characterized by their distinct phases acquired under rotations of $\frac{\pi}{2}$ around the main molecular symmetry axis, which are $\phi_S=\pi$ for the SOMO, $\phi_H=0$ for the HOMO and $\phi_{L\pm}=\pm\frac{\pi}{2}$ for the two LUMOs. This in turn imposes symmetry constraints on the Hamiltonian (2.17): Let again R be the rotation of 90 degrees around the fourfold molecular axis with $\tilde{\mathbf{r}} := R^{-1}\mathbf{r}$

$$R\,|j\rangle = \mathrm{e}^{i\phi_j}\,|j\rangle\,, \tag{2.52}$$

$$\psi_j(R^{-1}\mathbf{r}) = \psi_j(\tilde{\mathbf{r}}) = \langle\tilde{\mathbf{r}}|j\rangle = \langle\mathbf{r}|R|j\rangle = \mathrm{e}^{i\phi_j}\,\langle\mathbf{r}|j\rangle = \psi_j(\mathbf{r})\,\mathrm{e}^{i\phi_j}. \tag{2.53}$$

Now, consider for example the Coulomb interaction

$$V(r_{12}) = \frac{1}{4\pi\varepsilon_0}\frac{1}{|\mathbf{r}_1-\mathbf{r}_2|}. \tag{2.54}$$

Due to the absolute value, $V(r_{12})$ is invariant under rotations of both $\mathbf{r}_1$ and $\mathbf{r}_2$. This yields for V_{ijkl} after a coordinate transformation $\mathbf{r}_i \to \tilde{\mathbf{r}}_i$ under the integral:

$$V_{ijkl} = \int \mathrm{d}^3r_1 \int \mathrm{d}^3r_2\,\psi_i^*(\mathbf{r}_1)\psi_j(\mathbf{r}_1)V(r_{12})\psi_k^*(\mathbf{r}_2)\psi_l(\mathbf{r}_2)$$

$$
\begin{aligned}
&= \int \mathrm{d}^3\tilde{r}_1 \int \mathrm{d}^3\tilde{r}_2\, \psi_i^*(\tilde{\mathbf{r}}_1)\psi_j(\tilde{\mathbf{r}}_1)V(\tilde{r}_{12})\psi_k^*(\tilde{\mathbf{r}}_2)\psi_l(\tilde{\mathbf{r}}_2) \\
&= \int \mathrm{d}^3 r_1 \int \mathrm{d}^3 r_2\, \psi_i^*(R^{-1}\mathbf{r}_1)\psi_j(R^{-1}\mathbf{r}_1)\ldots \\
&\qquad\qquad V(r_{12})\psi_k^*(R^{-1}\mathbf{r}_2)\psi_l(R^{-1}\mathbf{r}_2) \\
&= \int \mathrm{d}^3 r_1 \int \mathrm{d}^3 r_2\, \psi_i^*(\mathbf{r}_1)\mathrm{e}^{-i\phi_i}\psi_j(\mathbf{r}_1)\mathrm{e}^{i\phi_j}\ldots \\
&\qquad\qquad V(r_{12})\psi_k^*(\mathbf{r}_2)\mathrm{e}^{-i\phi_k}\psi_l(\mathbf{r}_2)\mathrm{e}^{i\phi_l} \qquad (2.55) \\
&= \mathrm{e}^{-i(\phi_i-\phi_j+\phi_k-\phi_l)}\, V_{ijkl}. \qquad (2.56)
\end{aligned}
$$

In order to obtain a true statement, the phases have to meet the constraint

$$\phi_i - \phi_j + \phi_k - \phi_l = 0 \bmod 2\pi. \qquad (2.57)$$

Therefore a given matrix element of the Coulomb interaction V_{ijkl} is different from zero only if the sum of the corresponding phases adds up to multiples of 2π: $\phi_i - \phi_j + \phi_k - \phi_l = 2\pi \cdot n,\ n \in \mathbb{Z}$, which drastically reduces the number of possible matrix elements of the Coulomb interaction. In Tab. 2.2 we list all nonvanishing matrix elements of the Coulomb interaction which are used in this work. For the crystal field correction V_{ij}^{ion} it can be shown that:

$$
\begin{aligned}
V_{ij}^{\mathrm{ion}} &= \mathrm{e}^{-i(\phi_i-\phi_j)}\, V_{ij}^{\mathrm{ion}} \qquad (2.58) \\
\Rightarrow V_{ij}^{\mathrm{ion}} &= V_{ii}^{\mathrm{ion}}\, \delta_{ij}, \qquad (2.59)
\end{aligned}
$$

since all phases ϕ_i are different; $\phi_i \neq \phi_j$ for $i \neq j$. Hence V_{ij}^{ion} is diagonal in the $\{S,H,L\pm\}$ basis. In the following we treat the V_{ii}^{ion} as free parameters and include them in the parameter Δ_i.

2.2.4 *The many-body Hamiltonian of copper phthalocyanine*

After all these preparatory considerations, we are finally able to write a many-body Hamiltonian for CuPc in the frontier orbital basis:

$$
\begin{aligned}
\hat{H}_{\mathrm{mol}} = &\sum_i (\epsilon_i + \Delta_i)\ \hat{n}_i + \sum_i U_i\, n_{i\uparrow}n_{i\downarrow} + \frac{1}{2}\sum_{[ij]} U_{ij}\, \hat{n}_i\hat{n}_j \\
&- \frac{1}{2}\sum_{[ij]}\sum_\sigma J_{ij}^{\mathrm{ex}}\ \left(\hat{n}_{i\sigma}\hat{n}_{j\sigma} - \hat{d}_{i\sigma}^\dagger\hat{d}_{j\bar{\sigma}}^\dagger\hat{d}_{i\bar{\sigma}}\hat{d}_{j\sigma}\right) \\
&+ \frac{1}{2}\sum_{[ij]}\sum_\sigma J_{ij}^{\mathrm{p}}\ \hat{d}_{i\sigma}^\dagger\hat{d}_{i\bar{\sigma}}^\dagger\hat{d}_{j\bar{\sigma}}\hat{d}_{j\sigma} \\
&+ \frac{1}{2}\sum_{[ijk]}\sum_\sigma \left(\tilde{J}_{ijk}^{\mathrm{p}}\ \hat{d}_{i\sigma}^\dagger\hat{d}_{i\bar{\sigma}}^\dagger\hat{d}_{k\bar{\sigma}}\hat{d}_{j\sigma} + \mathrm{h.c.}\right) \qquad (2.60)
\end{aligned}
$$

where indices are now running only over orbitals from the dynamic set $\{S,\ H,\ L\pm\}$. Stemming from Hartree-Fock calculations for isolated

U_S	11.352 eV	$J^{\mathrm{ex}}_{HL} = -\tilde{J}^{\mathrm{p}}_{H+-}$	548 meV
U_H	1.752 eV	J^{ex}_{+-}	258 meV
$U_L = U_{+-}$	1.808 eV	J^{p}_{+-}	168 meV
U_{SH}	1.777 eV	$J^{\mathrm{ex}}_{SL} = -\tilde{J}^{\mathrm{p}}_{S+-}$	9 meV
U_{SL}	1.993 eV	$J^{\mathrm{ex}}_{SH} = J^{\mathrm{p}}_{SH}$	2 meV
U_{HL}	1.758 eV		

Table 2.2: Major nonvanishing Coulomb integrals between the SOMO(S), the HOMO(H), the LUMO$^+$ (+) and the LUMO$^-$ (-). All values are calculated numerically using Monte Carlo integration [Gal13] of the real space orbitals depicted in Figs. 2.2 and 2.3, respectively, and renormalized by a constant $\epsilon_{mol} = 2.2$.

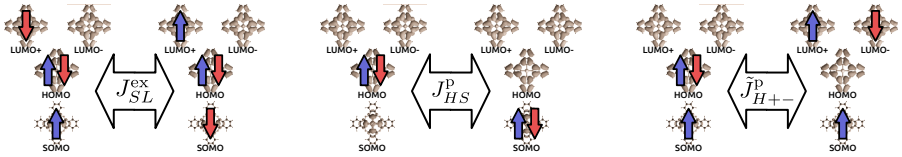

Figure 2.4: Artistic scheme depicting some of the interaction terms appearing in Eq. (2.60). From left to right: Ordinary exchange term, pair hopping term and split-pair hopping term.

atoms [Man67], the atomic onsite energies ϵ_α in Eq. (2.21) do not take into account the ionic background of the molecule and crystal field contributions. Therefore the MO energies ϵ_i have to be renormalized with parameters to counteract this shortage. The corresponding paramters Δ_i are free parameters in our theory.

The abbreviations we introduced in Eq. (2.60) are the orbital Coulomb interaction $U_i = V_{iiii}$, the inter-orbital Coulomb interaction $U_{ij} = V_{iijj}$, the exchange integral $J^{\mathrm{ex}}_{ij} = V_{ijji}$, the ordinary pair hopping term $J^{\mathrm{p}}_{ij} = V_{ijij}$ and the split pair hopping term $\tilde{J}^{\mathrm{p}}_{ijk} = V_{ijik}$, which couples states with a pair of electrons in one orbital to states having electrons with opposite spin in either LUMO. In Fig. 2.4 we show schematically which many-body basis states are coupled by the just introduced terms. For a description of how the interacting part can be brought into the form as in Eq. (2.60), see App. A.2.1. Contributions with four different indices are found to be very small (on the order of μeV) and thus omitted in this work. The integrals V_{ijkl} are calculated by Monte Carlo integrating (see App. A.2.2) the respective real space orbitals $\psi_i(\mathbf{r})$ with the Coulomb interaction and renormalized with a dielectric constant ε_r in order to account for screening given by the frozen occupied orbitals [RDGR13]. Table 2.2 lists all Coulomb integrals which were used in this work. For the atomic orbitals $\phi_{\alpha m}(\mathbf{r})$ we used as a real space basis Slater-type orbitals [Sla30] for the evaluation of the integrals. In contrast to the wavefunctions of the hydrogen atom, they do not have nodes, but rather approach their asymptotic form for larger

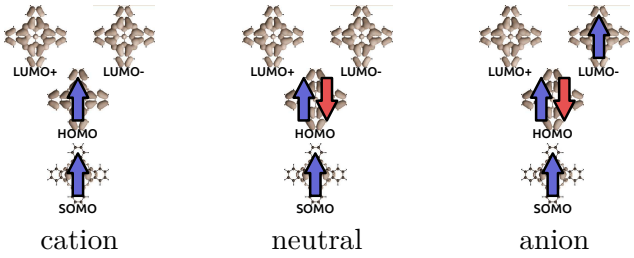

Figure 2.5: Artistic depiction of the ground states of the cationic, neutral and anionic molecule.

distances. The radial part of a Slater-type orbital for an electron in the n-th shell is given by

$$\psi(r) = N_r r^{n-1} \, \mathrm{e}^{-\xi r}, \tag{2.61}$$

where N_r is the normalization and ξ is an effective nuclear charge. In this work we used the effective charges from Ref. [CR63]. To obtain atomic orbitals, they are dressed with spherical harmonics Y_{lm} analogous to the atomic orbitals of hydrogen. For a $2\mathrm{p}_z$ orbital for example we then have:

$$\begin{aligned} \psi(\mathbf{r}) &= Y_{10}(\theta, \phi) N_r r^1 \, \mathrm{e}^{-\xi r} \\ &= \frac{N_r}{2} \sqrt{\frac{3}{\pi}} \, z \, \mathrm{e}^{-\xi r}. \end{aligned} \tag{2.62}$$

In Fig. 2.5 we show artistic depictions of the ground states of the cationic, neutral and anionic molecule. Note that the actual states, due to the interaction terms in Eq. 2.60, contain many more contributions from different Slater determinants.

3 A TRANSPORT FORMALISM FOR STM SETUPS

STM junctions with molecules on insulating films are highly asymmetric transport setups; on the one hand they have a design-inherent asymmetry in the rates of tunneling between tip and molecule and between the molecule and the substrate [WBJJ89, NWH05]. On the other hand, in contrast to lateral quantum dot setups, in an STM the voltage drops asymetrically across the junction [DTH+97, WEHP+15]. By considering an insulating layer with thickness d and relative dielectric constant ε_r, the bias drop across the dielectric can be estimated by using a two-capacitor model as

$$c_{\mathrm{S}} = \frac{d}{d + \varepsilon_r h}, \tag{3.1}$$

where h is the tip-molecule separation. Thus the voltage drop across the vacuum in this model is given by $c_{\mathrm{T}} = 1 - c_{\mathrm{S}}$, yielding the asymmetric dependences of the tip and substrate chemical potentials with the applied bias voltage V_b:

$$\mu_{\mathrm{S}}(V_b) = -\phi_0^{\mathrm{S}} - c_{\mathrm{S}}|e|V_b, \tag{3.2}$$

$$\mu_{\mathrm{T}}(V_b) = -\phi_0^{\mathrm{T}} + c_{\mathrm{T}}|e|V_b, \tag{3.3}$$

where $|e|$ is the absolute value of the elementary charge. Since $c_{\mathrm{S}} < c_{\mathrm{T}}$ due to Eq. (3.1), the chemical potential of the substrate moves much slower with applied bias voltage than the one of the tip. For a more sophisticated discussion also involving a voltage drop across the molecule, see Sec. 3.1.3. Throughout this work, we assume tip and substrate equilibrium chemical potentials to be equal, $\phi_0^{\mathrm{S}} = \phi_0^{\mathrm{T}} = \phi_0$.

As we will see in later chapters, these asymmetries can have substantial effects on the transport properties of such junctions. In this

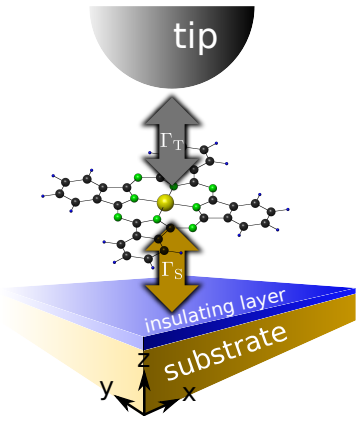

Figure 3.1: Schematic view of an STM single molecule junction.

chapter we demonstrate how we model electronic transport through those systems.

3.1 THEORETICAL DESCRIPTION OF STM SETUPS

The full Hamiltonian describing transport across an STM junction with a molecule on a thin insulating layer, cf. Fig. 3.1, reads

$$\hat{H} = \hat{H}_{\mathrm{mol}} + \hat{H}_{\mathrm{mol-env}} + \hat{H}_{\mathrm{S}} + \hat{H}_{\mathrm{T}} + \hat{H}_{\mathrm{tun}}, \tag{3.4}$$

where $\hat{H}_{\mathrm{mol}}$ is the Hamiltonian of the molecule and $\hat{H}_{\mathrm{S}}$ and $\hat{H}_{\mathrm{T}}$ are the Hamiltonians of the substrate and the tip, respectively. They are describing noninteracting electronic leads,

$$\hat{H}_{\eta} = \sum_{\mathbf{k}\sigma} \epsilon_{\eta\mathbf{k}}\, \hat{c}^{\dagger}_{\eta\mathbf{k}\sigma} \hat{c}_{\eta\mathbf{k}\sigma}, \tag{3.5}$$

with $\eta = \mathrm{S/T}$. Here $\hat{c}^{\dagger}_{\mathbf{k}\sigma}$ creates an electron in lead η with spin σ. To incorporate image charge effects which lead to renormalization of the charged states of the system [KF11], we include a term $\hat{H}_{\mathrm{mol-env}}$, see Sec. 3.1.3. The tunneling Hamiltonian $\hat{H}_{\mathrm{tun}}$ finally is given by

$$\hat{H}_{\mathrm{tun}} = \sum_{\eta\mathbf{k}i\sigma} t^{\eta}_{\mathbf{k}i}\, \hat{c}^{\dagger}_{\eta\mathbf{k}\sigma} + \mathrm{h.c.}, \tag{3.6}$$

where the $t^{\eta}_{\mathbf{k}i}$ are the tunneling matrix elements (TMEs) between lead η and the molecule. They are calculated as the overlap integrals between electronic lead states $|\eta\mathbf{k}\rangle$ and molecular orbitals $|i\rangle$ [SDG12, DSSG12]:

$$t^{\eta}_{\mathbf{k}i} = \epsilon_i \langle \eta\mathbf{k}|i\rangle\,. \tag{3.7}$$

The lead wavefunctions $\langle \mathbf{r}|\eta\mathbf{k}\rangle$ can be expressed in the following form:

$$\Psi^{\eta}(x,y,z) = \psi^{\chi}_{\parallel}(x,y)\psi^{\chi}_{\perp}(z), \tag{3.8}$$

where $\psi^{\eta}_{\parallel}(x,y)$ is given by plane waves for $\eta = \mathrm{S}$, or by the wavefunction of the ground state of a two-dimensional harmonic oscillator for $\eta = \mathrm{T}$ [SDG12]. The wavefunctions $\psi^{\eta}_{\perp}(z)$ are the exponentially decaying parts of the solutions of one-dimensional finite potential wells, see Fig. 3.2:

$$\psi^{\mathrm{S}}_{\perp}(z) = n^{\mathrm{S}}_{\perp}\, \mathrm{e}^{-\kappa_{\mathrm{S}} z} \quad \text{and} \quad \psi^{\mathrm{T}}_{\perp}(z) = n^{\mathrm{T}}_{\perp}\, \mathrm{e}^{\kappa_{\mathrm{T}}(z - z_{\mathrm{tip}})}, \tag{3.9}$$

where $n^{\eta}_{\perp}$ accounts for normalization and κ_{η} is given by:

$$\kappa_{\eta} = \sqrt{\frac{2m}{\hbar^2}(-\varepsilon^{\eta}_0 - \epsilon_z)}, \tag{3.10}$$

where $\varepsilon^{\eta}_0 = -\varepsilon^{\eta}_{\mathrm{F}} - \phi^{\eta}_0$ is the depth of the potential well in lead η and ϵ_z is the energy in z-direction of the lead state. The Fermi energy of lead η is denoted by ε_{F}. A general state in lead η has the energy

$$\epsilon_{\eta\mathbf{k}} = \varepsilon^{\eta}_0 + \epsilon_{\parallel} + \epsilon_z, \tag{3.11}$$

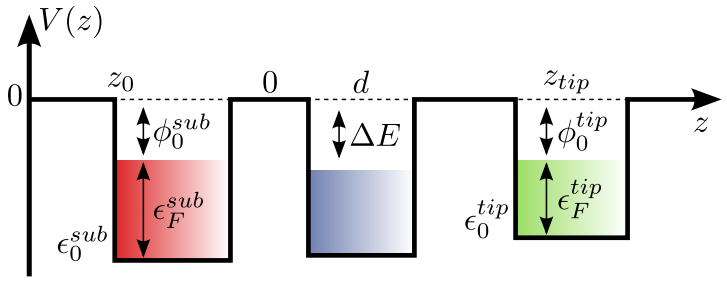

Figure 3.2: Potentials in transport direction in an STM setup. The $\varepsilon_0^{\mathrm{sub}}$ and $\varepsilon_0^{\mathrm{tip}}$ are the depths of the potential well in the respective lead, ϕ_0^{sub} and ϕ_0^{tip} are the workfunctions and $\varepsilon_{\mathrm{F}}^{\mathrm{sub}}$ and $\varepsilon_{\mathrm{F}}^{\mathrm{tip}}$ the Fermi energies.

where $\epsilon_{\parallel}$ is its energy in the x and y directions.

For the analytical derivation of the TMEs we approximate the atomic orbital $\phi_{\alpha m}(\mathbf{r})$ by contracted Gaussian orbitals $g(\mathbf{r})$ to simplify the calculation of the overlap integrals:

$$g(\mathbf{r}) = \sum_{i=1}^{N_c} d_i \, \mathrm{e}^{-a_i r^2}. \tag{3.12}$$

Here N_c is the number of Gaussians used to approximate the atomic orbital; in this work we used $N_c = 3$. A more thorough definition of the Gaussian orbitals, their contraction coefficients d_i and their exponents a_i can be found in Refs. [HSP69, PLHS80]. As an example, a p_z orbital in this approximation is given by

$$p_z(\mathbf{r}) = n_{\mathrm{p}} \, \mathbf{r} \cdot \hat{\mathbf{e}}_{\mathbf{z}} \, g_{2p}(\mathbf{r}). \tag{3.13}$$

A d_{zx} orbital then accordingly reads:

$$d_{zx}(\mathbf{r}) = n_{\mathrm{d}} \, \mathbf{r} \cdot \hat{\mathbf{e}}_x \, \mathbf{r} \cdot \hat{\mathbf{e}}_z \, g_{3d}(\mathbf{r}). \tag{3.14}$$

The parameters n_{p} and n_{d} are ensuring normalization and thus depend on the actual atomic species for which the orbitals are calculated for.

Anticipating from subsequent sections, the TMEs appear in our transport formalism in the following form:

$$\Gamma_{ij}^{\eta} = \frac{2\pi}{\hbar} \sum_{\mathbf{k}} \left(t_{\mathbf{k}i}^{\eta}\right)^* t_{\mathbf{k}j}^{\eta} \, \delta(\epsilon_{\eta\mathbf{k}} - \Delta E). \tag{3.15}$$

Introducing

$$M_{\alpha m,\beta n}^{\eta}(\Delta E) = \frac{2\pi}{\hbar} \sum_{\mathbf{k}} \delta(\epsilon_{\eta\mathbf{k}} - \Delta E) \langle \alpha m | \eta\mathbf{k} \rangle \langle \eta\mathbf{k} | \beta n \rangle, \tag{3.16}$$

we can write

$$\Gamma_{ij}^{\eta} = \epsilon_i \epsilon_j \sum_{\alpha\beta} c_{i\alpha m} c_{j\beta n}^* \, M_{\alpha m,\beta n}^{\eta}. \tag{3.17}$$

The quantity $M_{\alpha m,\beta n}^{\eta}$ depends on the type of the orbitals $|\alpha m\rangle$ and $|\beta n\rangle$. In the following subsections, we illustrate how we analytically derive all the different contributions to $M_{\alpha m,\beta n}^{\eta}$.

3.1.1 *Substrate-molecule tunneling rates*

In the case of the substrate, the sum over $\mathbf{k}$ in Eq. 3.16, after splitting it into an in-plane part $\sum_{\mathbf{k}_\parallel}$ and a part in z-direction $\sum_{\mathbf{k}_z}$, is converted to the following integral [SDG12]:

$$\sum_{\mathbf{k}} \to \Omega_\mathrm{S} \int \mathrm{d}E_\mathrm{S}, \tag{3.18}$$

where we used the abbreviations

$$\int \mathrm{d}E_\mathrm{S} := \int_0^{-\varepsilon_0^\mathrm{S}} \mathrm{d}\epsilon_z \int_0^{\epsilon_z} \mathrm{d}\epsilon_\parallel \, \frac{1}{\sqrt{\epsilon_z}} \delta\left(\varepsilon_0^\mathrm{S} + \epsilon_z + \epsilon_\parallel - \Delta E\right) \tag{3.19}$$

for the energy integration and

$$\Omega_\mathrm{S} = \frac{V_\mathrm{S}}{a_0^3} \frac{\pi}{2\hbar\sqrt{\epsilon_R^3}}, \tag{3.20}$$

with the volume of the substrate V_S, the Bohr radius a_0 and the Rydberg energy ϵ_R. The in-plane momentum is given by

$$k_\parallel = \sqrt{\frac{2m\epsilon_\parallel}{\hbar^2}}. \tag{3.21}$$

Then $M^\mathrm{S}_{\alpha m,\beta n}$ can be represented in the following form:

$$M^\mathrm{S}_{\alpha m,\beta n} = \Omega_\mathrm{S} \int \mathrm{d}E_\mathrm{S} \, f^*_{\alpha m}(k_\parallel,\kappa) f_{\beta n}(k_\parallel,\kappa) \, G_{\alpha m,\beta n}(k_\parallel). \tag{3.22}$$

The functions $f_{\alpha m}(k_\parallel,\kappa)$ depend on the nuclear species of atom α and the type of orbital m; the functions needed to set up TMEs involving the SOMO, the HOMO and the LUMOs in CuPc thus are:

$$\begin{aligned}
f_{\alpha\mathrm{s}}(k_\parallel,\kappa) &= \pi \frac{n_{\alpha\mathrm{s}}}{\sqrt{S}} \sum_i \frac{d_i}{a_i} \mathrm{e}^{-\frac{k_\parallel^2}{4a_i}} I^0_\mathrm{S}(\kappa,a_i),\\
f_{\alpha\mathrm{p}_{x/y}}(k_\parallel,\kappa) &= -i\pi k_\parallel \frac{n_{\alpha\mathrm{p}}}{2\sqrt{S}} \sum_i \frac{d_i}{a_i^2} \mathrm{e}^{-\frac{k_\parallel^2}{4a_i}} I^0_\mathrm{S}(\kappa,a_i),\\
f_{\alpha\mathrm{p}_z}(k_\parallel,\kappa) &= \pi \frac{n_{\alpha\mathrm{p}}}{\sqrt{S}} \sum_i \frac{d_i}{a_i} \mathrm{e}^{-\frac{k_\parallel^2}{4a_i}} I^1_\mathrm{S}(\kappa,a_i),\\
f_{\alpha\mathrm{d}_{zx/yz}}(k_\parallel,\kappa) &= -i\pi k_\parallel \frac{n_{\alpha\mathrm{d}_{zx/yz}}}{2\sqrt{S}} \sum_i \frac{d_i}{a_i^2} \mathrm{e}^{-\frac{k_\parallel^2}{4a_i}} I^1_\mathrm{S}(\kappa,a_i),\\
f_{\alpha\mathrm{d}_{x^2-y^2}}(k_\parallel,\kappa) &= -\frac{\pi}{4} k_\parallel^2 \frac{n_{\alpha\mathrm{d}_{x^2-y^2}}}{\sqrt{S}} \sum_i \frac{d_i}{a_i^3} \mathrm{e}^{-\frac{k_\parallel^2}{4a_i}} I^0_\mathrm{S}(\kappa,a_i),
\end{aligned} \tag{3.23}$$

where S is the surface area of the substrate. The $I^0_\mathrm{S}(\kappa,a_i)$ and $I^1_\mathrm{S}(\kappa,a_i)$ stem from the integration over z of the overlap integral between the

atomic orbital and the substrate wavefunction, cf. App. A.3, while the $G_{\alpha m,\beta n}(k_\parallel)$ capture the angular integration in k-space:

$$G_{\alpha m,\beta n}(k_\parallel) := \int_0^{2\pi} \mathrm{d}\theta\, \mathrm{e}^{ik_\parallel r_{\alpha\beta}\cos\theta}\, g_m^*(\theta+\theta_{\alpha\beta}) g_n(\theta+\theta_{\alpha\beta}). \tag{3.24}$$

Equation (3.24) governs the angular dependence of the overlap integral. The angle $\theta_{\alpha\beta}$ is the polar angle between the vector $\mathbf{r}_{\alpha\beta}$ and the positive x-axis. Unlike the functions $f_{\alpha m}$, the functions g_m depend only on the type of the respective orbital:

$$\begin{aligned} g_{\mathrm{s}}(\theta) &= g_{\mathrm{p}_z}(\theta) = 1, \\ g_{\mathrm{p}_x}(\theta) &= g_{\mathrm{p}_{zx}}(\theta) = \cos\theta, \\ g_{\mathrm{p}_y}(\theta) &= g_{\mathrm{p}_{yz}}(\theta) = \sin\theta, \\ g_{\mathrm{p}_{x^2-y^2}}(\theta) &= \cos^2\theta - \sin^2\theta. \end{aligned} \tag{3.25}$$

The integral in Eq. (3.24) can be evaluated using

$$\begin{aligned} &\int_0^{2\pi} \mathrm{d}\theta\, \sin^p(\theta+\varphi)\cos^q(\theta+\varphi)\,\mathrm{e}^{ix\cos\theta} \\ =&\frac{(-1)^p\, i^q \pi}{2^{p+q-1}} \sum_{k=0}^{p}\sum_{l=0}^{q} \binom{p}{k}\binom{q}{l} (-1)^l\, J_{p+q-2(k+l)}(x)\, \mathrm{e}^{i(2[k+l]-[p+q])\varphi}, \end{aligned} \tag{3.26}$$

where $J_i(x)$ is the i-th order Bessel function (See App. A.3 for the derivation of Eq. (3.26)). Due to the delta function, the integral over $\epsilon_\parallel$ in Eq. (3.19) can be evaluated trivially by substituting

$$k_\parallel \to \tilde{k}_{\mathrm{S}} = \sqrt{\frac{2m}{\hbar^2}\left(\Delta E - \varepsilon_0\mathrm{S} - \epsilon_z\right)} \tag{3.27}$$

and multiplying the integrand in Eq. (3.22) with the product of Heaviside functions $\theta_{\mathrm{H}}\left(\Delta E - \varepsilon_0^{\mathrm{S}} - \epsilon_z\right)\theta_{\mathrm{H}}\left(\varepsilon_0^{\mathrm{S}} + 2\epsilon_z - \Delta E\right)$. The remaining integration over ϵ_z has to be done numerically. As an example, $M^{\mathrm{S}}_{\alpha m,\beta n}$ for a $\mathrm{d}_{x^2-y^2}$ orbital at $\mathbf{r}_\alpha$ and a p_x orbital at $\mathbf{r}_\beta$ reads:

$$\begin{aligned} M^{\mathrm{S}}_{\alpha\mathrm{d}_{x^2-y^2},\beta\mathrm{p}_x} = &\frac{\pi^4}{16}\frac{V}{a_0^3}\frac{n_{\alpha\mathrm{d}_{x^2-y^2}} n_{\beta\mathrm{p}_x}}{S\hbar\sqrt{2\epsilon_R^3}} \sum_{ij}\frac{d_i d_j}{a_i^3 a_j^2} \\ &\times \int_0^{-\varepsilon_0^{\mathrm{S}}} \mathrm{d}\epsilon_z\, \frac{\tilde{k}_{\mathrm{S}}^3}{\sqrt{\epsilon_z}}\, \mathrm{e}^{-\frac{\tilde{k}_{\mathrm{S}}^2}{4}\left(a_i^{-1}+a_j^{-1}\right)} I_{\mathrm{S}}^0(\kappa,a_i) I_{\mathrm{S}}^0(\kappa,a_j) \\ &\times \left(\cos 3\theta_{\alpha\beta}\, J_3(\tilde{k}_{\mathrm{S}} r_{\alpha\beta}) - \cos\theta_{\alpha\beta}\, J_1(\tilde{k}_{\mathrm{S}} r_{\alpha\beta})\right) \\ &\times \theta_{\mathrm{H}}\left(\Delta E - \varepsilon_0^{\mathrm{S}} - \epsilon_z\right)\theta_{\mathrm{H}}\left(\varepsilon_0^{\mathrm{S}} + 2\epsilon_z - \Delta E\right). \end{aligned} \tag{3.28}$$

Since $M^{\mathrm{S}}_{\alpha m,\beta n}$ is not position-dependent, it is invariant under rotations of $\frac{\pi}{2}$ around the main symmetry axis of CuPc. Thus, due to the acquired phases ϕ_i of the molecular orbitals under such rotations, we can infer for Γ^{S}_{ij} analogous to Eq. (2.55):

$$\Gamma^{\mathrm{S}}_{ij} = \mathrm{e}^{i(\phi_i-\phi_j)}\,\Gamma^{\mathrm{S}}_{ij}. \tag{3.29}$$

This means that in the frontier orbital basis $\{S,H,L\pm\}$ the tunneling rates of the substrate are diagonal, i.e. $\Gamma^{\mathrm{S}}_{ij} = \Gamma^{\mathrm{S}}_{ii}\,\delta_{ij}$.

3.1.2 *Tip-molecule tunneling rates*

Due to the fact that the planar energy component of the tip wavefunction is fixed at $\varepsilon_{\parallel} = \hbar\omega$ [SDG12], there is only one single integration in energy to evaluate in order to obtain the tip-molecule tunneling rates. Because of this, they are much more straightforward to calculate than their substrate-molecule counterparts:

$$\begin{aligned} M^{\mathrm{T}}_{\alpha m,\beta n} =& \frac{2\pi}{\hbar^2}\int_0^{-\varepsilon_0^{\mathrm{T}}} \mathrm{d}\varepsilon_z\, D(\varepsilon_z)\langle\alpha|\mathrm{T}\mathbf{k}\rangle\langle\mathrm{T}\mathbf{k}|\beta\rangle\,\delta(\epsilon_{\mathbf{k}} - \Delta E) \\ =& \frac{2\pi}{\hbar^2}\sqrt{\frac{m}{2}}\frac{L_{\mathrm{T}}}{\Delta E - \varepsilon_0^T - \hbar\omega}\langle\alpha\sigma|T\vec{k}\sigma\rangle\langle T\vec{k}\sigma|\beta\sigma\rangle. \end{aligned} \tag{3.30}$$

The parameter L_{T} stems from the one-dimensional density of states of the tip and it is cancelled later on by the normalization of the tip wavefunction. In the following we list the overlap integrals needed to construct the matrices $M^{\mathrm{T}}_{\alpha\beta}$. After introducing the following parameters and abbreviations, $\nu^2 = \frac{m\omega}{2\hbar}$, $\Delta y_\alpha = y_{\mathrm{tip}} - y_\alpha$, $\Delta x_\alpha = x_{\mathrm{tip}} - x_\alpha$, $\lambda_i = \frac{\nu^2 a_i}{\nu^2 + a_i}$ and finally $\kappa_{\mathrm{T}} = \sqrt{\frac{2m}{\hbar^2}(\hbar\omega - \Delta E)}$, we are able to give the overlap integrals between the different orbitals located at $\mathbf{r}_\alpha$ and the tip wavefunction:

$$\begin{aligned} \langle\alpha\mathrm{s}|\mathrm{T}\mathbf{k}\rangle &= \sqrt{2\pi}\nu n_{\alpha\mathrm{s}}\sum_j \frac{d_j}{\nu^2 + a_j}\,\mathrm{e}^{-\lambda_j\left(\Delta x_\alpha^2 + \Delta y_\alpha^2\right)}\, I^0_{\mathrm{T}}(\kappa_{\mathrm{T}}, a_j), \\ \langle\alpha\mathrm{p}_x|\mathrm{T}\mathbf{k}\rangle &= \sqrt{2\pi}\nu^3 n_{\alpha\mathrm{p}_x}\sum_j \frac{d_j\Delta x_\alpha}{(\nu^2 + a_j)^2}\,\mathrm{e}^{-\lambda_j\left(\Delta x_\alpha^2 + \Delta y_\alpha^2\right)}\, I^0_{\mathrm{T}}(\kappa_{\mathrm{T}}, a_j), \\ \langle\alpha\mathrm{p}_x|\mathrm{T}\mathbf{k}\rangle &= \sqrt{2\pi}\nu^3 n_{\alpha\mathrm{p}_y}\sum_j \frac{d_j\Delta y_\alpha}{(\nu^2 + a_j)^2}\,\mathrm{e}^{-\lambda_j\left(\Delta x_\alpha^2 + \Delta y_\alpha^2\right)}\, I^0_{\mathrm{T}}(\kappa_{\mathrm{T}}, a_j), \\ \langle\alpha\mathrm{p}_x|\mathrm{T}\mathbf{k}\rangle &= \sqrt{2\pi}\nu n_{\alpha\mathrm{p}_z}\sum_j \frac{d_j}{\nu^2 + a_j}\,\mathrm{e}^{-\lambda_j\left(\Delta x_\alpha^2 + \Delta y_\alpha^2\right)}\, I^1_{\mathrm{T}}(\kappa_{\mathrm{T}}, a_j), \\ \langle\alpha\mathrm{d}_{zx}|\mathrm{T}\mathbf{k}\rangle &= \sqrt{2\pi}\nu^3 n_{\alpha\mathrm{d}_{zx}}\sum_j \frac{d_j\Delta x_\alpha}{(\nu^2 + a_j)^2}\,\mathrm{e}^{-\lambda_j\left(\Delta x_\alpha^2 + \Delta y_\alpha^2\right)}\, I^1_{\mathrm{T}}(\kappa_{\mathrm{T}}, a_j), \\ \langle\alpha\mathrm{d}_{yz}|\mathrm{T}\mathbf{k}\rangle &= \sqrt{2\pi}\nu^3 n_{\alpha\mathrm{d}_{yz}}\sum_j \frac{d_j\Delta y_\alpha}{(\nu^2 + a_j)^2}\,\mathrm{e}^{-\lambda_j\left(\Delta x_\alpha^2 + \Delta y_\alpha^2\right)}\, I^1_{\mathrm{T}}(\kappa_{\mathrm{T}}, a_j), \\ \langle\alpha\mathrm{d}_{x^2-y^2}|\mathrm{T}\mathbf{k}\rangle &= \sqrt{2\pi}\nu^5 n_{\alpha\mathrm{d}_{x^2-y^2}}\sum_j \frac{d_j(\Delta x_\alpha^2 - \Delta y_\alpha^2)}{(\nu^2 + a_j)^2} \\ &\quad\times \mathrm{e}^{-\lambda_j\left(\Delta x_\alpha^2 + \Delta y_\alpha^2\right)}\, I^1_{\mathrm{T}}(\kappa_{\mathrm{T}}, a_j). \end{aligned} \tag{3.31}$$

With this at hand, we can compute the tunneling rates for the tip as

$$\Gamma^{\mathrm{T}}_{ij} = \epsilon_i\epsilon_j\sum_{\alpha\beta} c_{i\alpha m}c^*_{j\beta n}\, M^{\mathrm{T}}_{\alpha m,\beta n}. \tag{3.32}$$

In contrast to the tunneling rates for the substrate, the tip tunneling rates can be nondiagonal, i.e. in general $\Gamma^{\mathrm{T}}_{ij} \neq 0$ for $i \neq j$.

3.1.3 *Electrostatical interactions with the environment*

Due to the presence of the leads, the Hamiltonian $\hat{H}_{\text{mol}}$ for a molecule in an STM setup gets renormalized due to image charges effects [KF11, PVM+13]. We model these effects with an effective Hamiltonian

$$\hat{H}_{\text{mol-env}} = -\delta_{\text{ic}}(\hat{N} - N_0)^2, \tag{3.33}$$

with $\hat{N}$ the particle number operator on the system and δ_{ic} the strength of the image charge renormalization. Due to the polarizability of the molecule, the bias voltage between source and drain is not entirely dropping at the contacts between the molecule and the leads. Depending on the geometry of the junction, a considerable fraction can also drop across the molecule itself, thus $c_{\text{S}} + c_{\text{T}} + c_{\text{M}} = 1$. Then the values of δ_{ic} and $c_{\text{S}/T/M}$ are calculated according to the following electrostatic considerations.

From the addition energy of the neutral molecule $U_0 \equiv E_{N_0+1,0} - 2E_{N_0,0} + E_{N_0-1,0}$, we associate a capacitance $C_{\text{M}} = e^2/U_0$ to the molecule. For the tip-molecule and the substrate-molecule capacitances we adopt the parallel plate model and define $C_{\text{T}} = \epsilon_0 A/h$ and $C_{\text{S}} = \epsilon_0\epsilon_r A/d$, where $A = 144$ Å^2 is an estimate of the CuPc single molecule surface, h is the tip-molecule distance, $\epsilon_r = 5.9$ is the relative permittivity of NaCl, d is the thickness of the NaCl thin film and ϵ_0 is the vacuum permittivity. Connecting these three capacitances in series, we obtain an estimate of the relative potential drops

$$c_{\text{S}/T/M} = \frac{C_{tot}}{C_{\text{S}/T/M}}, \tag{3.34}$$

where $C_{tot}^{-1} = C_{\text{S}}^{-1} + C_{\text{T}}^{-1} + C_{\text{M}}^{-1}$. The relative potential drop c_{M} on the molecule is for $h = 5$ Å, $d = 8.1$ Å(thickness of a trilayer NaCl) and $U_0 = 2.7$ eV about a quarter of the applied bias.

The estimate for the image charge parameter δ_{ic} proceeds from the same model. First we calculate the electrostatic energy associated to the three capacitors C_{T}, C_{M} and C_{S} in series. We assume that no external bias is applied but the first and the last plate are grounded. We then calculate the electrostatic energy E_{up} (E_{down}) for a unit charge deposited between C_{T} and C_{M} (C_{M} and C_{S}): Consider that a charge e is placed between C_{T} and C_{M}. Since the molecule is polarizable, the charge will distribute asymetrically across the molecule, with Q_1 facing "upwards" and $-Q_2$ facing "downwards", with $Q_1 - Q_2 = e$, see Fig. 3.3. This yields a potential $V_1 = \frac{Q_1}{c_{\text{T}}}$ against the tip, a potential $V_2 = \frac{-Q_2}{c_{\text{S}}}$ against the substrate and a potential $V_2 - V_1 = \frac{Q_2}{c_{\text{M}}}$ across the molecule. Then, solving for V_1 and using $E_{\text{up}} = \frac{eV_1}{2}$ yields

$$E_{\text{up}} = \frac{e^2}{2}\frac{1}{\frac{C_{\text{M}}C_{\text{S}}}{C_{\text{M}}+C_{\text{S}}} + C_{\text{T}}}, \qquad E_{\text{down}} = \frac{e^2}{2}\frac{1}{\frac{C_{\text{M}}C_{\text{T}}}{C_{\text{M}}+C_{\text{T}}} + C_{\text{S}}}, \tag{3.35}$$

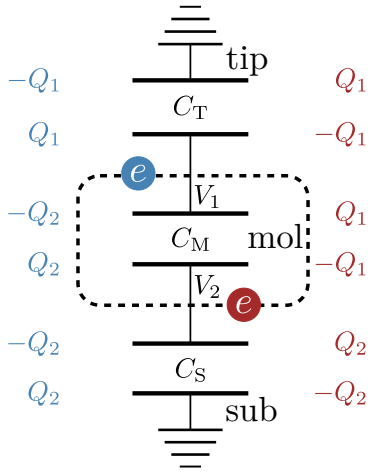

Figure 3.3: Three-capacitor model to estimate the image charge renormalization. The dashed area represents the molecular "slab". Blue (red) colors denote the situation when the charge e is placed between C_T and C_M (C_M and C_S).

where E_{down} is found in an analogous way. Finally, for the image charge parameter we write:

$$-\delta_{\text{ic}} = \frac{E_{\text{up}} + E_{\text{down}}}{2} - U_0/2, \tag{3.36}$$

i.e. the difference between the average electrostatic energy and the average energy needed to charge the isolated molecule. The average of the electrostatic energies gives an estimate of the energy needed to charge the molecule in presence of the leads. If we subtract from it the average addition energy of the isolated molecule, $U_0/2$, for which we already account in the many-body Hamiltonian (2.60), we obtain indeed an estimate of the image charge effects.

3.2 THE TRANSPORT DYNAMICS

In this Section we set up a master equation to describe the transport dynamics through CuPc in an STM setup. Since coherences of the density operator ρ can play a large role in such systems, we try to not make any assumption about the off-diagonal elements of ρ a priori. We take them into account in the best possible way while maintaining the feasibility of our computations.

3.2.1 *The Liouville-von Neumann equation*

As already discussed in the previous Sections, the full Hamiltonian describing a molecule on an insulating layer in an STM setup reads

$$\hat{H} = \hat{H}_{\text{mol}} + \hat{H}_{\text{mol-env}} + \hat{H}_{\text{S}} + \hat{H}_{\text{T}} + \hat{H}_{\text{tun}}. \tag{3.37}$$

Following Ref. [Blu96], we can calculate the time evolution of the density operator $\hat{\rho}$ of the total system using the Liouville-von Neumann equation:

$$i\hbar \frac{\mathrm{d}\hat{\rho}(t)}{\mathrm{d}t} = \left[\hat{H},\, \hat{\rho}(t)\right]. \tag{3.38}$$

By treating the tunneling Hamiltonian $\hat{H}_{\mathrm{tun}}$ as a perturbation to the Hamiltonian $\hat{H}_0 = \hat{H}_{\mathrm{mol}} + \hat{H}_{\mathrm{mol-env}} + \hat{H}_{\mathrm{S}} + \hat{H}_{\mathrm{T}}$, we can change into the interaction picture with the transformation

$$\hat{\rho}^I(t) = \mathrm{e}^{\frac{i}{\hbar}\hat{H}_0 t}\, \hat{\rho}(t)\, \mathrm{e}^{-\frac{i}{\hbar}\hat{H}_0 t}. \tag{3.39}$$

This yields the Liouville-von Neumann equation in the interaction picture:

$$i\hbar \frac{\mathrm{d}\hat{\rho}^I(t)}{\mathrm{d}t} = \left[\hat{H}^I_{\mathrm{tun}}(t),\, \hat{\rho}^I(t)\right], \tag{3.40}$$

where

$$\hat{H}^I_{\mathrm{tun}}(t) = \mathrm{e}^{\frac{i}{\hbar}\hat{H}_0 t}\, \hat{H}_{\mathrm{tun}}\, \mathrm{e}^{-\frac{i}{\hbar}\hat{H}_0 t}. \tag{3.41}$$

Formally, the solution of Eq. (3.40) is given by:

$$\hat{\rho}^I(t) = \hat{\rho}^I(t_0) - i\hbar \int_{t_0}^{t} \mathrm{d}t_1\, [\hat{H}^I_{\mathrm{tun}}(t_1),\, \hat{\rho}^I(t_1)], \tag{3.42}$$

which, reinserted into Eq. (3.40) yields:

$$\dot{\hat{\rho}}^I(t) = -i\hbar\, [\hat{H}^I_{\mathrm{tun}}(t),\ \hat{\rho}^I(t_0)] + (i\hbar)^2 \int_{t_0}^{t} \mathrm{d}t_1\, \left[\hat{H}^I_{\mathrm{tun}}(t),\, [\hat{H}^I_{\mathrm{tun}}(t_1),\, \hat{\rho}^I(t_1)]\right]. \tag{3.43}$$

3.2.2 *The master equation for the reduced density matrix*

In order to reduce the complexity of our problem, we trace out the bath degrees of freedom to arrive at the equation of motion for the reduced density operator $\hat{\rho}^I_{\mathrm{red}}(t) = \mathrm{Tr}_{\mathrm{S,T}}\, \hat{\rho}^I(t)$:

$$\begin{aligned}\dot{\hat{\rho}}^I_{\mathrm{red}}(t) = &-\frac{i}{\hbar}\, \mathrm{Tr}_{\mathrm{S,T}}\, [\hat{H}^I_{\mathrm{tun}}(t),\ \hat{\rho}^I(t_0)] \\ &+ \left(\frac{i}{\hbar}\right)^2 \int_{t_0}^{t} \mathrm{d}t_1\, \mathrm{Tr}_{\mathrm{S,T}}\, \left[\hat{H}^I_{\mathrm{tun}}(t),\, [\hat{H}^I_{\mathrm{tun}}(t_1),\, \hat{\rho}^I(t_1)]\right].\end{aligned} \tag{3.44}$$

Assuming the molecule to be uncorrelated with the contacts at t_0, we factorize the density matrix at $t = t_0$:

$$\hat{\rho}^I(t_0) = \hat{\rho}^I_{\mathrm{red}}(t_0)\hat{\rho}_{\mathrm{T}}(t_0)\hat{\rho}_{\mathrm{S}}(t_0). \tag{3.45}$$

Considering the leads as large thermal reservoirs, their density matrices at time t_0 are described by equilibrium density operators:

$$\hat{\rho}_\eta(t_0) \equiv \hat{\rho}_\eta = \frac{e^{-\beta(\hat{H}_\eta - \mu_\eta \hat{N}_\eta)}}{Z_\eta}. \tag{3.46}$$

Assuming weak coupling between the molecule and the leads allows the total density matrix at time t to be factorized:

$$\hat{\rho}^I(t) = \hat{\rho}^I_{\text{red}}(t)\hat{\rho}_{\text{T}}\hat{\rho}_{\text{S}}. \tag{3.47}$$

Inserting Eq. (3.47) into Eq. (3.44) yields:

$$\dot{\hat{\rho}}^I_{\text{red}}(t) = -\frac{1}{\hbar^2}\int_{t_0}^{t} \mathrm{d}t_1 \ \text{Tr}_{\text{S,T}}\left[\hat{H}^I_{\text{tun}}(t),\, [\hat{H}^I_{\text{tun}}(t_1),\, \hat{\rho}^I_{\text{red}}(t_1)\hat{\rho}_{\text{T}}\hat{\rho}_{\text{S}}]\right], \tag{3.48}$$

where we dropped the first term of Eq. (3.44) since it does not conserve the particle number in the leads and thus vanishes. In Eq. (3.48), due to $\hat{H}^I_{\text{tun}}(t)$ and $\hat{H}^I_{\text{tun}}(t_1)$, there are expectation values of creation and annihilation operators of the leads at different times, so-called bath-correlation functions. If they decay much faster than the characteristic time scale of the molecule, the latter will be unaffected by those rapid changes [Blu96] and we can change $\hat{\rho}^I_{\text{red}}(t_1)$ to $\hat{\rho}^I_{\text{red}}(t)$ in Eq. (3.48):

$$\dot{\hat{\rho}}^I_{\text{red}}(t) = -\frac{1}{\hbar^2}\int_{t_0}^{t} \mathrm{d}t_1 \ \text{Tr}_{sub,\,tip}\left[\hat{H}^I_{\text{tun}}(t),\, [\hat{H}^I_{\text{tun}}(t_1),\, \hat{\rho}^I_{\text{red}}(t)\hat{\rho}_{\text{T}}\hat{\rho}_{\text{S}}]\right]. \tag{3.49}$$

However, when $t \to \infty$ in the stationary limit, we regain an exact solution despite this approximation. Finally we perform a variable transformation $t_1 = t - \tau$, and, since we are interested in the dynamics of the system for $t \gg t_0$, set $t_0 \to \infty$. Going back to the Schrödinger picture, expanding the commutators and taking the traces in Eq. (3.49) ultimately yields the generalized master equation (GME) for the reduced density matrix:

$$\begin{aligned}
\dot{\hat{\rho}}_{\text{red}} = \ & -\frac{i}{\hbar}\left[\hat{H}_0,\, \hat{\rho}_{\text{red}}\right] - \frac{1}{\hbar^2}\sum_{\eta}\sum_{ijk}\int_0^{\infty}\mathrm{d}\tau\, t^{\eta}_{ki}(t^{\eta}_{kj})^*\Big\{ \\
& f^+_{\eta}(\epsilon_{\mathbf{k}})\left(\hat{d}_i\hat{d}^{\dagger}_j(-\tau)\hat{\rho}_{\text{red}} - \hat{d}^{\dagger}_j(-\tau)\hat{\rho}_{\text{red}}\hat{d}_i\right)\mathrm{e}^{+\frac{i}{\hbar}\epsilon_{\mathbf{k}}\tau} \\
& + f^-_{\eta}(\epsilon_{\mathbf{k}})\left(\hat{d}^{\dagger}_j\hat{d}_i(-\tau)\hat{\rho}_{\text{red}} - \hat{d}_i(-\tau)\hat{\rho}_{\text{red}}\hat{d}^{\dagger}_j\right)\mathrm{e}^{-\frac{i}{\hbar}\epsilon_{\mathbf{k}}\tau} \\
& + f^+_{\eta}(\epsilon_{\mathbf{k}})\left(\hat{\rho}_{\text{red}}\hat{d}_i(-\tau)\hat{d}^{\dagger}_j - \hat{d}^{\dagger}_j\hat{\rho}_{\text{red}}\hat{d}_i(-\tau)\right)\mathrm{e}^{-\frac{i}{\hbar}\epsilon_{\mathbf{k}}\tau} \\
& + f^-_{\eta}(\epsilon_{\mathbf{k}})\left(\hat{\rho}_{\text{red}}\hat{d}^{\dagger}_j(-\tau)\hat{d}_i - \hat{d}_i\hat{\rho}_{\text{red}}\hat{d}^{\dagger}_j(-\tau)\right)\mathrm{e}^{+\frac{i}{\hbar}\epsilon_{\mathbf{k}}\tau}\Big\},
\end{aligned} \tag{3.50}$$

where $f^+_{\eta}(\epsilon_{\mathbf{k}})$ is the Fermi distribution in lead η with chemical potential μ_{η} and $f^-_{\eta}(\epsilon_{\mathbf{k}}) = 1 - f^+_{\eta}(\epsilon_{\mathbf{k}})$.

3.2.3 *The GME in operator form*

Introducing the Liouvillian superoperator $\mathcal{L}$, Eq. (3.50) can be rewritten in the following form (dropping subscript and hat from $\hat{\rho}_{\text{red}}$):

$$\mathcal{L}[\rho] = \sum_{\eta}\left\{\left(\hat{\Gamma}^{\eta} - \frac{i}{\hbar}\hat{H}_{\text{mol}}\right)\rho + \rho\left(\hat{\Gamma}^{\eta} - \frac{i}{\hbar}\hat{H}_{\text{mol}}\right)^{\dagger} + \mathcal{L}^{\eta}_{\text{rest}}[\rho]\right\} \tag{3.51}$$

where

$$\mathcal{L}^{\eta}_{\text{rest}}[\rho] = \frac{1}{\hbar^2}\sum_{ij\sigma}\sum_{\mathbf{k}}\int_0^\infty \mathrm{d}\tau\, t^{\eta}_{\mathbf{k}i}(t^{\eta}_{\mathbf{k}j})^* \left(\hat{d}^\dagger_{j\sigma}(-\tau)\rho\,\hat{d}_{i\sigma}\, f^+_\eta(\epsilon_{\mathbf{k}})\,\mathrm{e}^{\frac{i}{\hbar}\epsilon_{\mathbf{k}}\tau} + \hat{d}_{i\sigma}(-\tau)\rho\,\hat{d}^\dagger_{j\sigma}\, f^-_\eta(\epsilon_{\mathbf{k}})\,\mathrm{e}^{-\frac{i}{\hbar}\epsilon_{\mathbf{k}}\tau}\right) + \text{h.c.}, \tag{3.52}$$

and $\hat{\Gamma}^\eta$ is given by

$$\hat{\Gamma}^{\eta} = -\frac{1}{\hbar^2}\sum_{ij\sigma}\sum_{\mathbf{k}}\int_0^\infty \mathrm{d}\tau\, t^{\eta}_{\mathbf{k}i}(t^{\eta}_{\mathbf{k}j})^* \left(\hat{d}_{i\sigma}\hat{d}^\dagger_{j\sigma}(-\tau)\, f^+_\eta(\epsilon_{\mathbf{k}})\,\mathrm{e}^{\frac{i}{\hbar}\epsilon_{\mathbf{k}}\tau} + \hat{d}^\dagger_{j\sigma}\hat{d}_{i\sigma}(-\tau)\, f^-_\eta(\epsilon_{\mathbf{k}})\,\mathrm{e}^{-\frac{i}{\hbar}\epsilon_{\mathbf{k}}\tau}\right). \tag{3.53}$$

To account for relaxation processes leading to de-excitation of molecular excited states, we introduce a phenomenological relaxation term $\mathcal{L}_{\text{rel}}$ in the Liouvillian in analogy to Ref. [KvO05]:

$$\mathcal{L}_{\text{rel}}[\rho] = -\frac{1}{\tau}\left(\rho - \sum_{Nm}\rho^{\text{th},N}_{mm}\,|Nm\rangle\langle Nm|\sum_n \rho^N_{nn}\right). \tag{3.54}$$

However, we have included in (3.54) coherences, thus $\mathcal{L}_{\text{rel}}$ accounts also for dephasing. For simplicity, we assume the same phenomenological rate for dephasing and dissipation. The relaxation term is proportional to the deviation of the reduced density matrix from the thermal one ρ^{th}, which is given by the Boltzmann distribution $\rho^{\text{th},N}_{mm} \sim \exp\left(-\frac{E_{Nm}}{k_B T}\right)$ with $\sum_m \rho^{\text{th},N}_{mm} = 1$. Since $\mathcal{L}_{\text{rel}}$ describes relaxation processes which conserve the particle number on the molecule, it does not contribute directly to the current: $\mathrm{Tr}_{\text{mol}}\left\{\hat{N}\mathcal{L}_{\text{rel}}[\rho]\right\} = 0$. The relaxation rate $\frac{1}{\tau}$ is taken of the same order of magnitude as the mean tip tunneling rate.

Equation (3.51) can be brought into a simpler form. By using the Sokhotski-Plemelj theorem,

$$\int_0^\infty \mathrm{d}\tau\,\mathrm{e}^{-i(x\pm\omega)\tau} = \pi\delta(x+\omega) - i\,\text{p.v.}\,\frac{1}{x\pm\omega}, \tag{3.55}$$

where p.v. denotes the Cauchy principal value, we find for a time-dependent operator $O(-\tau) = \mathrm{e}^{-\frac{1}{\hbar}\hat{H}_0\tau}\,O\,\mathrm{e}^{\frac{1}{\hbar}\hat{H}_0\tau}$:

$$\begin{aligned}&\int_0^\infty \mathrm{d}\tau\, O(-\tau)\, f^+_\eta(\epsilon_{\mathbf{k}})\,\mathrm{e}^{\frac{i}{\hbar}\epsilon_{\mathbf{k}}\tau}\\ &= \sum_{mn}\langle m|O|n\rangle\left(\int_0^\infty \mathrm{d}\tau\,\mathrm{e}^{-\frac{i}{\hbar}(E_m - En)}\,\mathrm{e}^{\frac{i}{\hbar}\epsilon_{\mathbf{k}}\tau}\, f^+_\eta(\epsilon_{\mathbf{k}})\right)|m\rangle\langle n|\end{aligned}$$

$$= \pi\hbar \sum_{mn} \langle m|O|n\rangle \left(f_\eta^+ (E_m - E_n) - \frac{i}{\pi} p_\eta(E_m - E_n) \right) |m\rangle \langle n| \,. \quad (3.56)$$

Here, the $p_\eta(\Delta E) = -\operatorname{Re} \psi\left(\frac{1}{2} + \frac{i\beta}{2\pi}(\Delta E - \mu_\eta)\right)$ stem from the principal part integration of the Fermi functions, with $\psi(z)$ the digamma function. Assuming that the TMEs $t^\eta_{\mathbf{k}i}$ are approximately constant when evaluating the principal part integrals, we can define the following operators:

$$D^{\eta+}_{i\sigma} := \sum_{mnj} \Gamma^\eta_{ij}(\Delta_{mn}) \langle m|\hat{d}^\dagger_{j\sigma}|n\rangle \left(f_\eta^+ (\Delta_{mn}) - \frac{i}{\pi} p_\eta(\Delta_{mn}) \right) |m\rangle \langle n| \quad (3.57)$$

$$D^{\eta-}_{i\sigma} := \sum_{mnj} \Gamma^\eta_{ji}(\Delta_{nm}) \langle m|\hat{d}_{j\sigma}|n\rangle \left(f_\eta^- (\Delta_{nm}) - \frac{i}{\pi} p_\eta(\Delta_{nm}) \right) |m\rangle \langle n| \,, \quad (3.58)$$

where we used the abbreviation $\Delta_{mn} = -\Delta_{nm} = E_m - E_n$. Hence, with

$$\begin{aligned} \Gamma &= -\frac{1}{2} \sum_\eta \sum_{i\sigma} \left(\hat{d}_{i\sigma} D^{\eta+}_{i\sigma} + \hat{d}^\dagger_{i\sigma} D^{\eta-}_{i\sigma} \right) - \frac{i}{\hbar} \hat{H}_{\mathrm{mol}}, \\ \mathcal{L}_{\mathrm{rest}}[\rho] &= \frac{1}{2} \sum_\eta \sum_{i\sigma} \left(\hat{d}_{i\sigma}\, \rho\, D^{\eta+}_{i\sigma} + \hat{d}^\dagger_{i\sigma}\, \rho\, D^{\eta-}_{i\sigma} \right) + \mathrm{h.c.}, \end{aligned} \quad (3.59)$$

we can write the GME in operator form:

$$\dot{\rho} = \mathcal{L}[\rho] = \Gamma\rho + \rho\Gamma^\dagger + \mathcal{L}_{\mathrm{rest}}[\rho] + \mathcal{L}_{\mathrm{rel}}[\rho]. \quad (3.60)$$

This form of the GME is actually used in our transport algorithms.

In particular, we are interested in the stationary solution ρ^∞ for which $\dot{\rho}^\infty = \mathcal{L}[\rho^\infty] = 0$.

3.3 COMPUTATION OF THE STATIONARY SOLUTION

Our main goal when evaluating the GME is to obtain the stationary solution ρ^∞,

$$\dot{\rho}^\infty = \mathcal{L}[\rho^\infty] = 0. \quad (3.61)$$

We are hence searching for the nullspace of the operator $\mathcal{L}$, which is quite a challenge because of its superoperator structure. The most straightforward solution would be setting up the matrix representation of $\mathcal{L}$ and applying standard diagonalization schemes. But since the dimension of the Liouville space scales quadratically with the Hilbert space dimension which in turn scales exponentially with the number of degrees of freedom, this route is moribund already when dealing with not too large systems. Instead, our method of choice is the Arnoldi method which allows for computation of eigenstates and eigenenergies of large systems, and, what is even more beneficial for our requirements,

does not require the matrix representation of the operator to be diagonalized.

Another means for reaching faster and better convergence in the calculation of the stationary solution is the truncation of active Fock states, i.e. shrinking down the set of available states. We will later discuss the legitimity of that method.

3.3.1 *Arnoldi method*

The Arnoldi method is an iterative eigenvalue algorithm based on the concept of Krylov subspaces. A Krylov subspace of n-th order can be defined for an operator $\mathcal{M}$ and a vector $\mathbf{v}$:

$$\mathcal{K}_n = \text{span}\left\{\mathbf{v}, \mathcal{M}\mathbf{v}, \mathcal{M}^2\mathbf{v}, \ldots, \mathcal{M}^{n-1}\mathbf{v}\right\}, \tag{3.62}$$

where n is usually much smaller than the dimension of the operator, $n \ll \dim \mathcal{M}$. What the Arnoldi method does is to build up an orthonormal basis $\mathbf{q}_j$ for the Krylov subspace by using the Gram-Schmidt orthogonalization scheme and at the same time constructing an upper Hessenberg matrix H_n. Starting point is the normalization of the starting vector,

$$\mathbf{q}_1 = \frac{\mathbf{v}}{|\mathbf{v}|}. \tag{3.63}$$

Then, the remaining Krylov vectors $\mathbf{q}_{j+1}$, $j = 1, \ldots, n-1$ and the matrix elements $h_{i,j}$ of H_n, $i = 1, \ldots, j$, are iteratively constructed according to:

$$\begin{aligned} h_{i,j} &= \mathbf{q}_i^* \mathcal{M}\, \mathbf{q}_j \\ \tilde{\mathbf{q}}_{j+1} &= \mathcal{M}\, \mathbf{q}_j - \sum_{i=1}^{j} h_{ij}\, \mathbf{q}_i \\ h_{j+1,j} &= |\tilde{\mathbf{q}}_{j+1}| \\ \mathbf{q}_{j+1} &= \frac{\tilde{\mathbf{q}}_{j+1}}{h_{j+1,j}}. \end{aligned} \tag{3.64}$$

This procedure yields the matrix Q_n of Krylov vectors,

$$Q_n = \begin{pmatrix} \mathbf{q}_1 & \mathbf{q}_2 & \cdots & \mathbf{q}_n \end{pmatrix}, \tag{3.65}$$

and the upper Hessenberg matrix H_n,

$$H_n = \begin{pmatrix} h_{1,1} & h_{1,2} & h_{1,3} & \cdots & h_{1,n} \\ h_{2,1} & h_{2,2} & h_{2,3} & \cdots & h_{2,n} \\ 0 & h_{3,2} & h_{3,3} & \cdots & h_{3,n} \\ \vdots & \ddots & \ddots & \ddots & \vdots \\ 0 & \ldots & 0 & h_{n,n-1} & h_{n,n} \end{pmatrix}. \tag{3.66}$$

The eigenvalues of H_n are good approximations to the eigenvalues of $\mathcal{M}$. Since generally H_n is a small matrix, its eigenvalues can be calculated

with few effort using standard techniques. Then, for a given eigenvector $\mathbf{v}_\lambda$ of H_n with eigenvalue λ, we get the corresponding eigenvector $\mathbf{u}_\lambda$ of $\mathcal{M}$ with

$$\mathbf{u}_\lambda = Q_n \, \mathbf{v}_\lambda. \tag{3.67}$$

Specifically, in our case we are searching for the nullspace of the Liouvillian $\mathcal{L}$, i.e. $\lambda = 0$. Since the Liouvillian maps matrices onto matrices, we need to vectorize the matrices before handing them to the Arnoldi algorithm,

$$\begin{aligned} \rho &= \begin{pmatrix} \rho_{11} & \rho_{12} & \cdots & \rho_{1N} \\ \vdots & \vdots & \ldots & \vdots \\ \rho_{N1} & \rho_{N2} & \cdots & \rho_{NN} \end{pmatrix} \\ \Rightarrow \vec{\rho} &= \begin{pmatrix} \rho_{11} & \cdots & \rho_{N1} & \rho_{12} & \cdots & \rho_{N2} & \cdots & \rho_{1N} & \cdots & \rho_{NN} \end{pmatrix}^{\mathrm{T}}, \end{aligned} \tag{3.68}$$

and put them back into matrix form when $\mathcal{L}$ has to be applied. To calculate the nullspace of $\mathcal{L}$, we look for the eigenvector of H_n with the smallest eigenvalue. Let us call the eigenvector which was found with the Arnoldi method $\vec{\rho}_\mathrm{A}$ or ρ_A in its matrixform, respectively. Then the error ε can be estimated by

$$\varepsilon = \|\mathcal{L}\rho_\mathrm{A}\|_2, \tag{3.69}$$

where $\|\bullet\|_2$ is the 2-norm for matrices, which corresponds to the largest singular value of a matrix. Then, if the error lies above a given tolerance, $\varepsilon >$ tol, the suggested eigenvector is put into the Arnoldi iteration as a starting vector, i.e. $\mathbf{v} = \vec{\rho}_\mathrm{A}$. This procedure is repeated until $\varepsilon <$ tol.

Another possibility is to use the Implicitly Restarted Arnoldi Method (IRAM), which we are also using in this work. Schematically, what IRAM does different is to extend the initial H_n and Q_n matrices to H_{n+p} and Q_{n+p}, respectively. Then the eigenvalues of H_{n+p} are calculated and sorted. Finally the eigenstates corresponding to the worst p eigenvalues are projected out of H_{n+p} and Q_{n+p} using the QR-algorithm, yielding again n-th order H_n and Q_n matrices, from which finally eigenvectors and eigenvalues are calculated. The number p is usually much smaller than n, thus if it takes many iterations to arrive at a satisfying solution IRAM is often faster. However, it can not be determined a priori which method is faster or more reliable: it often depends on the type of problem and involves trial and error in order to find the more favorable method.

3.3.2 *Truncation of active Fock states*

Since in our formalism we do not only consider ground state-to-ground state transitions, but also transitions to excited states of the molecule, there exist in principle many different possible stationary solutions ρ^∞ for the nullspace algorithm to find, especially when there are also off-diagonal elements in the density matrix. Although there should be only

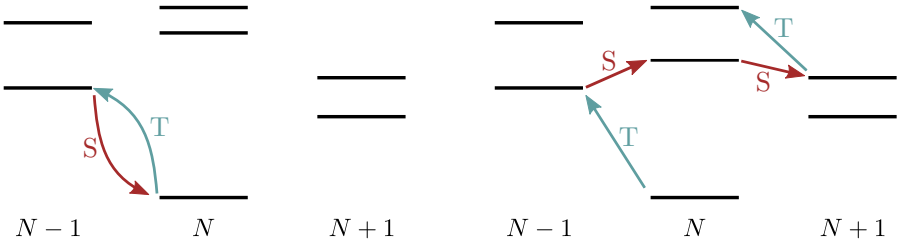

Figure 3.4: Left: Standard ground state-to-ground state transition. Right: cascading transitions. In this case, the bias voltage is negative, thus the commencing transition corresponds to the cationic resonance of the tip chemical potential.

one physical solution, it happens often that the algorithm gets stuck with a wrong solution, and because of its iterative nature is not able to find the physical solution. In particular, this can be the case when the physical solution has large contributions from excited states: Since we feed the Arnoldi algorithm with a Boltzmann distribution as a starting vector, if n and p for the Arnoldi algorithm are chosen too small, the Krylov space then essentially contains the wrong part of the spectrum of $\mathcal{L}$.

In order to reduce the number of possible solutions, we shrink down the number of many-body states available for the system to make transitions to. This is surely justified for states that are separated from the ground states by several eV. Additionally, the relaxation term $\mathcal{L}_{\text{rel}}$ rather strongly depopulates high-energy excited states. However, for states that are within a ~ 2 eV window from the ground state one has to be careful: by cascading transitions, see Fig. 3.4, between two or more different particle number subblocks of the spectrum, it is energetically possible for the system to reach such excited states; they can even be substantial in finding the physical solution when the system has to pass those states to end up in the stationary state.

Thus, when truncating the Fock states, one hast to start with a higher number of states and then gradually truncate them while checking that the obtained results like the current and the populations of the different many body states do not change. In this work we use 11 states in the cationic, 24 states in the neutral and 26 states in the anionic subblock of the spectrum. In the ranges of bias voltages and workfunctions presented in this work we found those numbers to be sufficient for obtaining the physical stationary solution.

3.3.3 *Expectation values of observables*

Having obtained the stationary solution ρ^{∞}, we are able to calculate expectation values of observables $\hat{O}$ as

$$\langle \hat{O} \rangle = \text{Tr}_{\text{mol}} \left(\hat{O} \rho^{\infty} \right). \tag{3.70}$$

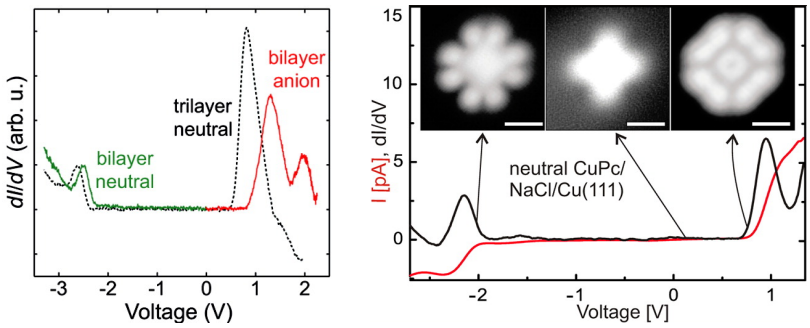

Figure 3.5: Left: Experimental data (black curve) to which our model was fitted, from [SSR11]. The experiment was performed on a NaCl(3ML)/Cu(100) substrate. Reprinted (adapted) with permission from [SSR11]. Copyright 2015 American Chemical Society. Right: topographical STM images at the cationic resonance, in the Coulomb gap and at the anionic resonance, from [USR13]. Reprinted (adapted) with permission from [USR13]. Copyright 2015 American Chemical Society.

The most obviuos expectation value to compute is the one of the current operator, which can be evaluated from the time derivative of the mean particle number in the system

$$\langle \hat{N} \rangle = \mathrm{Tr}_{\mathrm{mol}} \left(\hat{N} \rho^{\infty} \right). \tag{3.71}$$

Since $\dot{\rho} = \mathcal{L}[\rho]$, we get

$$\langle \hat{I}_{\mathrm{S}} + \hat{I}_{\mathrm{T}} \rangle = \frac{\mathrm{d}}{\mathrm{d}t} \langle \hat{N} \rangle = \mathrm{Tr}_{\mathrm{mol}} \left(\hat{N} \mathcal{L}[\rho^{\infty}] \right) \equiv 0. \tag{3.72}$$

The Liouvillian $\mathcal{L} = \mathcal{L}_{\mathrm{rel}} + \sum_{\eta} \mathcal{L}_{\eta}$ decomposes into the relaxation term and sub-Liouvillians for each lead. Sorting of the occuring terms in Eq. (3.72) after substrate and tip contributions yields the current operator of the respective lead η as

$$\hat{I}_{\eta} = \hat{N} \mathcal{L}_{\eta}. \tag{3.73}$$

By calculating the expectation value of the total spin operator $\hat{S}^2$,

$$\langle \hat{S}^2 \rangle = \mathrm{Tr}_{\mathrm{mol}} \left(\hat{S}^2 \rho^{\infty} \right), \tag{3.74}$$

and using that $\hat{S}^2 \left| s, s_z \right\rangle = s(s+1) \left| s, s_z \right\rangle$, we can also give an expression for the mean spin of the system:

$$S = \sqrt{\langle \hat{S}^2 \rangle + \frac{1}{4}} - \frac{1}{2}. \tag{3.75}$$

3.4 EXAMPLE: TRANSPORT IN THE STANDARD REGIME

In this section we show results obtained with the Hamiltonian of CuPc introduced in Sec. 2.2.4 and the transport formalism introduced in the

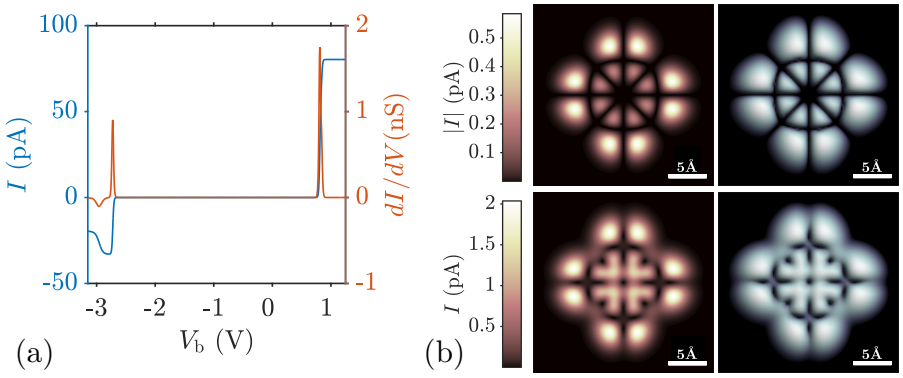

Figure 3.6: (a) IV characteristics (blue) and differential conductance (orange) for a CuPc molecule on a NaCl(3ML)/Cu(100) substrate. (b) Upper (lower) panel: Current maps of the cationic (anionic) resonance in CuPc. Left: Constant height map, right: Constant current map with setpoint at 0.5 (0.75) pA. The workfunction of the substrate is $\phi_0 = 4.65$ eV.

preceding sections. With standard regime we mean that the transition is a tip transition, i.e. the chemical potential of the tip is in resonance with a given excitation energy ΔE of the molecule; and additionally that the topography of the position-dependent results like constant height and constant current maps match the ones from eperiment, e.g. Refs. [SSR11, USR13, TMH08].

The bias voltage at which a transition from the mth N-particle state to the nth $N+1$ particle state of the molecule is happening is

$$V_{\mathrm{res},mn}(\phi_0) = \frac{1}{c_{\mathrm{T}}|e|}\left(E_{N+1,n} - E_{N,m} - \delta_{\mathrm{ic}} + \phi_0\right), \tag{3.76}$$

where e is the electron charge and c_{T} accounts for the fact that in STM setups the bias voltage drops asymetrically across the junction. We are using $c_{\mathrm{T}} = 0.59$ for the tip and $c_{\mathrm{S}} = -0.16$ for the substrate, see Sec. 3.1.3. If given without indices, V_{res} denotes the bias voltage corresponding to the ground state-to-ground state transition.

We fitted our model to the experiment of Swart et al. [SSR11], cf. Fig. 3.5, which was taken on a NaCl(3ML)/Cu(100) substrate (3 monolayers NaCl on the (100) crystallographic plane of copper) with a workfunction $\phi_0 = 4.65$ eV. To this end we used a constant shift $\Delta_i = \Delta = 1.83$ eV, a dielectric constant $\epsilon_{\mathrm{mol}} = 2.2$ in the evaluation of the matrix elements V_{ijkl}, and an image-charge renormalization $\delta_{\mathrm{ic}} = 0.32$ eV.

In Fig. 3.6 (a) we report the calculated current-voltage characteristics. At a positive bias voltage of about 0.8 eV, there is the anionic resonance and at negative bias of about -2.7 eV the cationic resonance is happening, whereas between them there is the Coulomb blockade region. The cause for the decrease of the current after the cationic resonance is the opening of transitions to neutral and anionic excited states similarly to what is shown in Fig. 3.4; once the transition to the

cationic ground state is open, from there further transitions to energetically accessible states are possible. If one of those states is a blocking state which can not be left, the current decreases the more this blocking state gets populated [BDDG08, SDG12, DSSG12], as discussed in the forthcoming chapter.

Turning to the topographical images, Fig. 3.6 (b) finally shows constant height and constant current STM maps recorded at the cationic and anionic resonances. At the cationic resonance, the depopulation of the HOMO is required, see Fig. 2.5. Thus the position-dependent current should mirror the structure of the corresponding wavefunction. Consequently, at the anionic resonance the STM should represent the topography of the LUMO. Comparing the current maps to the shapes of the wavefunctions of HOMO and LUMO in Figs. 2.2 and 2.3, respectively, we observe a satisfactory resemblance, also when comparing to STM images from an actual experiment, cf. Fig.3.5. In particular, the eightfold nodal plane structure of the HOMO and the four diagonal outer lobes of the LUMO, together with its virtual absence of nodal planes, are the most prominent features to identify the corresponding orbitals or to distinguish them amongst themselves, respectively.

4 MANY-BODY INTERFERENCE BLOCKADE

STM experiments have played an important role in the research field of NDC [LA89, BCMG89, CRRT99, ZWW+00, RJKT10, FSH+08], giving several examples of NDC observed with a variety of nanojunctions. A number of physical scenarios have been proposed for the explanation of the experimental findings: among others the existence of sharp resonances on both electrodes [BCMG89, XDH+99], the voltage dependent increase in the tunneling barrier height [GWYC05, TMH08], the orbital matching between molecule and tip [CHZ+07, SPX+09] or even just the symmetry matching between surface states in the substrate and molecular states [HRC+11]. Last but not least vibrational mediated NDC has also been observed in single molecule devices [GLH00] and proposed to test position dependent Franck-Condon factors in suspended carbon nanotubes [TZPCS11].

Recently, also interference phenomena in single molecule junctions have attracted intense theoretical [CSM06, KYB08, QLZ+08, SAH+08, MST10, TSY11, MST11, Ern11] and experimental [MWR+03, TTM+11, AMK+12, GVM+12] investigations. These junctions allow to tackle the fundamental question of the quantum mechanical nature of the electronic transport at the nanoscale and exhibit dramatic modulations of the current desirable for applications. The quest of specific fingerprints of the electronic interference which go beyond the bare current or conductance suppression [AMK+12] remains, though, a crucial issue. In this chapter we establish a criterion to identify the interference blocking scenario by correlating the spectral and the topographical information achievable in an STM single molecule measurement.

4.1 A MINIMAL MODEL

In this section, we set up a minimal model for describing interference NDC. It is predicted to occur in molecules whose electron affinity $EA = E_{N_0,0} - E_{N_0+1,0}$ or ionization potential $IP = E_{N_0-1,0} - E_{N_0,0}$ is very close to the workfunction ϕ_0 of the substrate, respectively. As discussed in Secs. 2.2.2.1 and 2.2.3, the molecular orbitals are classified according to their projection ℓ of the pseudo angular momentum along the principal rotation axis of the molecule.

For the minimal model we only consider the many-body basis spanned by the HOMO ($\ell = \ell_0$) and the two degenerate LUMOs ($\ell = \pm\ell_1$). Then, after neglecting the spin degree of freedom, the ground state of the neutral molecule is

$$|\mathrm{N}_0\, E_0\, \ell = \ell_0\rangle, \tag{4.1}$$

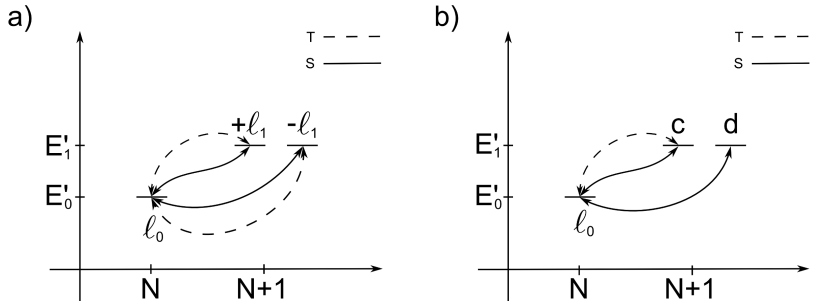

Figure 4.1: Schematic representation of the many-body states participating to the transport. On the vertical axis we report the grand canonical energies $E'_0 := E_0 - \mathrm{N}\mu_0$ and $E'_1 := E_1 - (\mathrm{N}+1)\mu_0$, being μ_0 the equilibrium chemical potential for the leads. In panel a) we adopt the angular momentum representation while in panel b) the decoupling basis is introduced for the anionic states.

which is nondegenerate with energy $E_0 = E_{N_0,0}$. The orbitally degenerate anionic ground state reads

$$|\mathrm{N}+1\, E_1\, \ell = \pm\ell_1\rangle, \tag{4.2}$$

with energy $E_1 = E_{N_0+1,0}$. Assume that the neutral state minimizes the grand canonical Hamiltonian $\hat{H}_\mathrm{G} = \hat{H} - \mu_0 N$. If $E_1 - E_0 \approx \mu_0$ there is a bias window in which the transport characteristics are dominated by a dynamics which involves the neutral and anionic ground states only. In panel a) of Fig. 4.1 we give a schematic representation of the many body states participating in the transport and the associated transition rates. Then, according to Ref. [SDG12], the corresponding GME for the RDM in the pseudo angular momentum basis reads:

$$\begin{aligned}\dot{\rho}^{\mathrm{N}_0 E_0}_{\ell_0\ell_0} &= -\sum_{\eta\ell} R^\eta_{\ell-\ell_0,\ell-\ell_0}(\Delta E)\, f^+_\eta(\Delta E)\, \rho^{\mathrm{N}_0 E_0}_{\ell_0\ell_0} \\ &\quad + \sum_{\eta\ell\ell'} R^\eta_{\ell-\ell_0,\ell'-\ell_0}(\Delta E)\, f^-_\eta(\Delta E)\, \rho^{\mathrm{N}_0+1E_1}_{\ell'\ell}\end{aligned} \tag{4.3}$$

$$\begin{aligned}\dot{\rho}^{\mathrm{N}_0+1E_1}_{\ell\ell'} = -\frac{1}{2}\sum_{\eta\ell''} \Big[& R^\eta_{\ell-\ell_0,\ell''-\ell_0}(\Delta E)\, \rho^{\mathrm{N}_0+1E_1}_{\ell''\ell'}, \\ & \rho^{\mathrm{N}_0+1E_1}_{\ell\ell''}\, R^\eta_{\ell''-\ell_0,\ell'-\ell_0}(\Delta E)\Big]\, f^-_\eta(\Delta E) \\ + \sum_\eta & R^\eta_{\ell-\ell_0,\,\ell'-\ell_0}(\Delta E) f^+_\eta(\Delta E)\, \rho^{\mathrm{N}_0 E_0}_{\ell_0\ell_0},\end{aligned} \tag{4.4}$$

where ℓ, ℓ' and $\ell'' = \pm\ell_1$ span the pseudo angular momenta of the anionic ground state and $\Delta E = E_1 - E_0$ is the energy difference between the anionic and neutral ground states. Note that, until stated otherwise, in this chapter we assume the potential drop of the tip to be $c_\mathrm{T} = 0.87 = 1 - c_\mathrm{S}$. The rate $R^\eta_{\ell-\ell_0,\,\ell'-\ell_0}$ is defined as:

$$R^\eta_{\Delta\ell,\Delta\ell'}(\Delta E) = \Gamma^\eta_{\Delta\ell,\Delta\ell''}(\Delta E)\, \langle \mathrm{N}_0+1E_1\ell|\hat{d}^\dagger_{\Delta\ell}|\mathrm{N}_0E_0\ell_0\rangle$$

$$\times \langle \mathrm{N}_0 E_0 \ell_0 | \hat{d}_{\Delta\ell'} | \mathrm{N}_0 + 1 E_1 \ell' \rangle, \tag{4.5}$$

where

$$\Gamma^{\eta}_{\Delta\ell,\Delta\ell'}(\Delta E) = \frac{2\pi}{\hbar} \sum_{\mathbf{k}} \left(t^{\eta}_{\mathbf{k}\Delta\ell}\right)^* t^{\eta}_{\mathbf{k}\Delta\ell'} \, \delta(\epsilon^{\eta}_{\mathbf{k}} - \Delta E), \tag{4.6}$$

and we have introduced the notation $\Delta\ell = \ell - \ell_0$, $\Delta\ell' = \ell' - \ell_0$ for the variation in angular momenta associated to the tunneling process.

Owing to the rotational symmetry of the molecule and the different spatial confinement of the leads (see Sec. 3.1), the rate matrices acquire the form:

$$R^{\mathrm{S}}_{\Delta\ell,\Delta\ell'} = R^{\mathrm{S}} \, \delta_{\Delta\ell,\Delta\ell'}, \tag{4.7}$$

$$R^{\mathrm{T}}_{\Delta\ell,\Delta\ell'} = R^{\mathrm{T}} \exp\left(-i \frac{\Delta\ell - \Delta\ell'}{\Delta\ell} \, \phi_{\Delta\ell}\right), \tag{4.8}$$

where we did not write for simplicity the energy dependence of R^S and the energy and tip position dependence of R^T and of the phase $\phi_{\Delta\ell}$. Moreover, the latter is defined as [SDG12]

$$\phi_{\Delta\ell} = \arg\left(t^{\mathrm{T}}_{\mathbf{k}\Delta\ell} \langle \mathrm{N}_0 E_0 \ell_0 | \hat{d}_{\Delta\ell} | \mathrm{N}_0 + 1 E_1 \ell \rangle\right). \tag{4.9}$$

Due to their particular structure, the rate matrices (4.7) are both diagonalized by the same basis transformation. While the substrate rate matrix is invariant under unitary transformations, the tip rate matrix acquires a peculiar diagonal form since one of its eigenvalues vanishes. The basis transformation reads

$$\begin{pmatrix} |\mathrm{c}\rangle \\ |\mathrm{d}\rangle \end{pmatrix} = \frac{1}{\sqrt{2}} \begin{pmatrix} \mathrm{e}^{-\mathrm{i}\phi_{\Delta\ell}} & \mathrm{e}^{+\mathrm{i}\phi_{\Delta\ell}} \\ \mathrm{e}^{-\mathrm{i}\phi_{\Delta\ell}} & -\mathrm{e}^{+\mathrm{i}\phi_{\Delta\ell}} \end{pmatrix} \begin{pmatrix} |+\ell_1\rangle \\ |-\ell_1\rangle \end{pmatrix} \tag{4.10}$$

and it depends on the position of the tip via the phase $\phi_{\Delta\ell}$. Due to the diagonal form of the rate matrices, in this basis the dynamics is described only by means of populations. In particular the *decoupled* states $|\mathrm{N}{+}1\, E_1\, \mathrm{d}\,\rangle$ are only coupled to the neutral ground state $|\mathrm{N}\, E_0\, \ell_0\rangle$ via substrate-molecule tunneling events. Both tunneling couplings are still open instead for the *coupled* states $|\mathrm{N}+1\, E_1\, \mathrm{c}\,\rangle$, see panel b) in Fig. 4.1. The corresponding master equation reads:

$$\begin{pmatrix} \dot{\rho}^{\mathrm{N}_0} \\ \dot{\rho}^{\mathrm{N}_0+1}_{\mathrm{c}} \\ \dot{\rho}^{\mathrm{N}_0+1}_{\mathrm{d}} \end{pmatrix} = \Bigg[2R^{\mathrm{T}} \begin{pmatrix} -2f^+_{\mathrm{T}} & 2f^-_{\mathrm{T}} & 0 \\ f^+_{\mathrm{T}} & -f^-_{\mathrm{T}} & 0 \\ 0 & 0 & 0 \end{pmatrix} + R^{\mathrm{S}} \begin{pmatrix} -4f^+_{\mathrm{S}} & 2f^-_{\mathrm{S}} & 2f^-_{\mathrm{S}} \\ f^+_{\mathrm{S}} & -f^-_{\mathrm{S}} & 0 \\ f^+_{\mathrm{S}} & 0 & -f^-_{\mathrm{S}} \end{pmatrix} \Bigg] \begin{pmatrix} \rho^{\mathrm{N}_0} \\ \rho^{\mathrm{N}_0+1}_{\mathrm{c}} \\ \rho^{\mathrm{N}_0+1}_{\mathrm{d}} \end{pmatrix}, \tag{4.11}$$

where for simplicity we have omitted the arguments (ΔE) of the Fermi functions and the tunneling rates R^{η} and suppressed the indexes E_0, ℓ_0

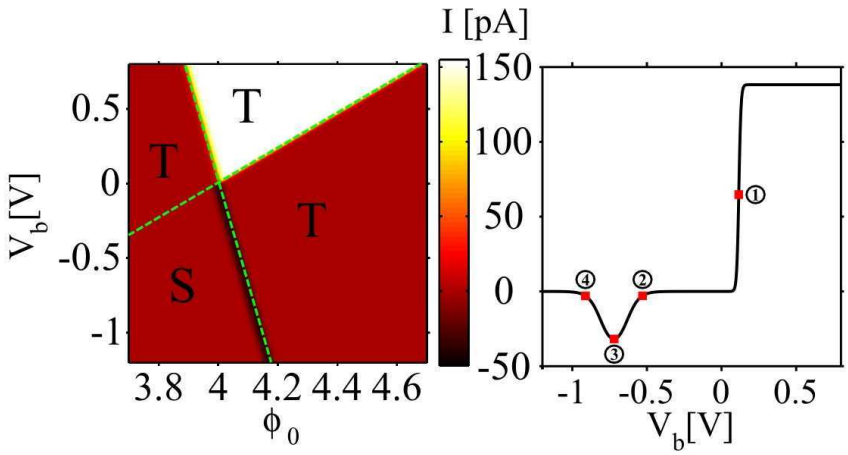

Figure 4.2: Left panel: Current through a CuPc single molecule junction as a function of the substrate (and tip) work function ϕ_0 and of the sample bias V_b. The tip apex position is assumed at $(x, y, z - d) = (+5, -5, 7)$ Å with the origin taken on the metal-insulator interface and in correspondance of the center of the molecule, and d being the thikness of the insulating layer (see Fig. 3.1). The tip and substrate resonant lines (respectively with positive and negative slopes) divide the parameter space into four regions. T (S) indicates a region in which the current is proportional to the tip (substrate) tunneling rate. Right panel: Current obtained from a cut of the left panel plot corresponding to $\phi_0 = 4.1eV$. The numbers on the current-voltage plot refer to the current maps of Fig. 4.3. The current scale is the same for the left and right panel.

.

and E_1 in the elements of the density matrix. The stationary current flowing through the STM junction is calculated as the average $\langle \hat{I}_S \rangle = \mathrm{Tr}\{\rho^\infty \hat{I}_S\} = -\langle \hat{I}_T \rangle$ where ρ^∞ is the stationary solution of Eq. (4.11) and $\hat{I}_\eta$ are the current operators, see Eq. (3.73). Despite its simplicity, Eq. (4.11) describes the system in a variety of different regimes which leave their fingerprints in the current voltage characteristics and current maps.

4.2 TOPOGRAPHICAL FINGERPRINTS

Given Eq. (4.11), the stationary current flowing through the system is

$$I(\mathbf{r}_T, V_b) = 2eR^S f_S^+ \rho^{N_0} \left(1 - \frac{\rho_c^{N_0+1}}{\rho_d^{N_0+1}}\right), \tag{4.12}$$

where e is the (negative) electron charge and

$$\rho^{N_0} = \left(1 + 2\frac{R^S f_S^+ + 2R^T f_T^+}{R^S f_S^- + 2R^T f_T^-} + 2\frac{f_S^+}{f_S^-}\right)^{-1}, \tag{4.13}$$

$$\frac{\rho_c^{N_0+1}}{\rho_d^{N_0+1}} = \frac{R^S f_S^+ + 2R^T f_T^+}{R^S f_S^- + 2R^T f_T^-} \cdot \frac{f_S^-}{f_S^+}. \tag{4.14}$$

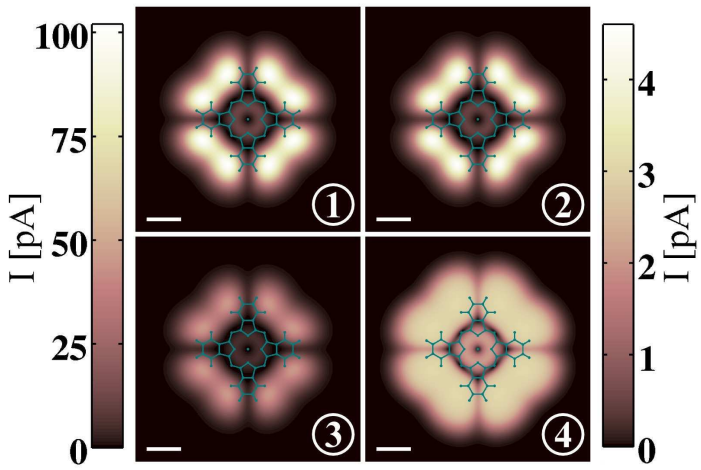

Figure 4.3: Constant height current maps calculated for different bias voltages. The color bar on the left (right) hand side corresponds to the maps 1 and 3 (2 and 4). The 5Å long white line sets the scale of the images. The numbers in the maps refer to the biases indicated in the right panel of Fig. 4.2. The current map in the interference blockade regime (map 4) appears flat in the molecule region. The characteristic nodal planes pattern appears instead much more pronounced at the positive and negative bias resonances (map 1 and 3) and even in the Coulomb blockade region (map 2). The tip apex is placed at 7Å above the molecular plane while the substrate biases are, respectively $V_{b1} = 0.1153$V, $V_{b2} = -0.5303$V, $V_{b3} = -0.7201$V, and $V_{b4} = -0.9118$V.

Since the rate R^T depends on the tip position and the Fermi functions on the bias, both topographical and spectral information is embedded in Eq. (4.12).

In the right panel of Fig. 4.2 we report the IV characteristics calculated for CuPc on a metal-insulator substrate ($d = 7$ Å with relative dielectric constant $\varepsilon_r = 5.9$) with an effective work function $\phi_S = 4.1eV$. Moreover, we assume an electron affinity $EA = E_0 - E_1 = 4$ eV.

At low bias the current is suppressed by Coulomb blockade. As the bias increases on the positive side the current undergoes a sudden jump corresponding to the opening of the neutral-anion transition at the tip-molecule interface $E_1 - E_0 = \mu_T(V_b)$. On the negative bias side the Coulomb blockade is also lifted, but this time at the substrate resonance point $E_1 - E_0 = \mu_S(V_b)$ and the current shows a sharp peak whose width scales with the temperature ($k_B T = 6$ meV in all presented plots). At higher negative biases the current is blocked due to interference and the decoupled anionic state is the sink of the system. A crucial condition for the interference blocking to occur is that $E_1 - E_0 \ll E_0 - E_{-1}$, ensuring that the substrate-molecule anion resonance anticipates the tip-molecule cation one which would otherwise dominate the transport characteristics.

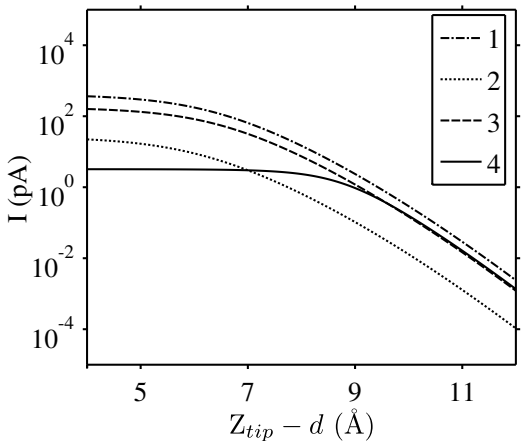

Figure 4.4: Current vs. tip-molecule distance calculated for different biases. The numbers in the legend correspond to the different cases illustrated in Fig. 4.3: respectively $V_{b1} = 0.1153$V, $V_{b2} = -0.5303$V, $V_{b3} = -0.7201$V and $V_{b4} = -0.9118$V. Notice in particular the wide plateau associated to the interference blockade regime (line 4) and its crossing with the Coulomb blockade line for $Z_{tip} - d = 7$Å.

Analogous interference blocking involving degenerate many-body states has been encountered in a variety of systems [DBDG09, DBG09, DBG10, BDDG08, SDG12]. Nevertheless the STM setup described here uniquely allows to correlate the interference current blocking with specific topographical fingerprints. In Fig. 4.3 we present different constant height current maps (the tip is positioned always 7 Å above the molecular plane) corresponding to the different points labeled in the right panel of Fig. 4.2. Maps 1 and 3 are calculated for the tip and substrate resonant tunneling conditions while maps 2 and 4 for the Coulomb and interference blockade regimes, respectively. Striking is the flattening of the current map obtained in the interference case (map 4) if compared to all other regimes.

Signatures of interference can be clearly seen also in the current vs. tip-molecule distance represented in Fig. 4.4. The four traces correspond to the four different biases conditions indicated with the numbers 1 to 4 in the right panel of Fig. 4.2 and the tip is in the same xy position. At large tip-molecule distances all traces show the exponentially decaying behaviour typical of the STM measurements (roughly 1 order of magnitude decay per Å). At shorter distances, all curves saturates due to the form of the p_z orbitals. Contrary to the others, though, the curve corresponding to the interference blockade regime (case 4) saturates at larger distances and shows a wide plateau. For this reason it even crosses the Coulomb blockade trace (case 2) at $\Delta z = 7$ Å, consistently with the result of Fig. 4.2.

Finally, we also present in Fig. 4.5 several constant current topographic maps simulated for different biases and different current setpoints. The surfaces presented in the upper panel correspond to the

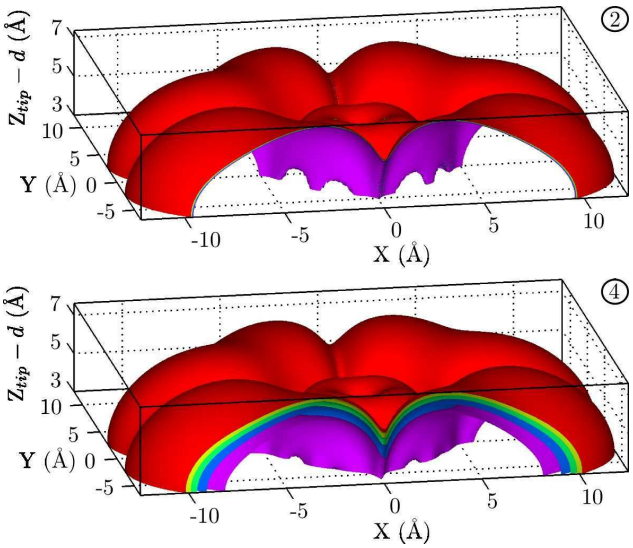

Figure 4.5: Isosurfaces of constant current calculated in the proximity of the Coulomb blockade (upper panel, $V_b = -0.5303\,\mathrm{V}$) and interference blockade (lower panel, $V_b = -0.9118\,\mathrm{V}$) regimes. The surfaces correspond in both cases to the currents: $I = 3.15$, 3.075, 3.0, 2.925, 2.85 pA.

Coulomb blockade regime, while the ones in the lower panel to the interference blockade. Due to the particular choice of the biases, the apparent height of the molecule is exactly the same if we choose 3 pA as a setpoint. The shape of the molecule is not modified in the interference blockade regime, as it is for the constant height current maps (see Fig.4.3). Quite noticeable is the enhanced sensitivity of the apparent height of the molecule with respect to the variation of the setpoint, if compared with the same measurement in the Coulomb blockade regime. The surfaces presented in Fig. 4.5 correspond in fact, for both cases, to working currents in the range $2.85 - 3.15$ pA.

4.3 ANALYTICAL EXAMINATION

The results presented in the previous section can be understood by analyzing the different limits of Eq. (4.12). In the Coulomb blockade regime, for negative bias voltages defined by $E_1 - E_0 - \mu_S \gg k_B T$, which in turn implies for the Fermi functions $f_S^+ \ll 1$ and $f_T^+ \ll 1$, we can show under the asymmetry relation $R^T \ll R^S$ typical of an STM experiment, that

$$I_{CB} = 4eR^T f_T^- \frac{f_S^+}{f_S^-}\left(1 + 4\frac{f_S^+}{f_S^-}\right)^{-1} \approx 4eR^T f_S^+. \tag{4.15}$$

Thus, the current is proportional to the tip rate. The equality in Eq. (4.15) has also a precise physical interpretation. The charge fluctuations at the substrate represent the fastest phenomenon ($f_S^+/f_T^+ \gg 1$ due to

the asymmetric potential drop at tip-molecule and substrate-molecule contacts) which sets the ratio between the populations of the states to be the thermal average, $\rho_{c/d}^{N_0+1}/\rho^{N_0} = f_S^+/f_S^-$. Finally, the trace sum rule implies:

$$\rho^{N_0} = \left(1 + 4\frac{f_S^+}{f_S^-}\right)^{-1}. \tag{4.16}$$

Instead, the current is determined by the slowest process, which is the transition $|N_0+1\, E_1\, c\rangle \to |N\, E_0\rangle$ happening at the tip. Equation (4.15) follows due to the presence of 2 spin channels and that the tip rate for the coupled state is $2R^T$. Analogously, for $V_b > 0$, the Coulomb blockade condition reads $E_1 - E_0 - \mu_T \gg k_B T$ and the current is again proportional to the tip rate, namely $I = -4eR^T f_T^+$. Thus, the constant height current map reproduces the shape of the molecular orbital encoded in R^T.

The interference blockade regime is confined to the negative bias and is defined by $E_1 - E_0 - \mu_S \ll -k_B T$, implying $f_S^+ \approx 1$ and $f_T^+ \ll 1$. Under these conditions Eq. (4.12), reduces to

$$\begin{aligned} I_{IB} &= e\frac{R^S f_S^- R^T f_T^-}{R^S f_S^- + R^T f_T^-} \\ &= \left[\left(eR^S f_S^-\right)^{-1} + \left(eR^T f_T^-\right)^{-1}\right]^{-1}. \end{aligned} \tag{4.17}$$

Equation (4.17) conveys that the current is the result of two competing processes happening in series: the thermal unblocking of the decoupled state $|N{+}1\, E_1 d\rangle \to |N\, E_0\rangle$ towards the substrate and the tip tunnelling event $|N{+}1\, E_1\, c\rangle \to |N\, E_0\rangle$. Notice that in the system dynamics the two tunnelling events are not independent: one cannot happen if the other did not happen before. In the interference blocking regime $f_S^- \ll f_T^-$, but, in an STM setup it typically also holds that $R^T \ll R^S$. At a fixed tip position (thus, the ratio R^T/R^S) and low enough bias, deep in the interference blockade, the condition $R^S f_S^- \ll R^T f_T^-$ holds. Thus, the current is proportional to R^S and independent of the tip position. This fact explains the flattening of the constant height current map in Fig. 4.3 and the wide plateau of the current versus tip molecule distance in Fig. 4.4. On the other hand, when the $R^T f_T^- \ll R^S f_S^-$ is fulfilled for example by moving the tip off the molecule, the tip rate drops and the position dependence of the current is recovered ($I_{IB} \propto R^T$). The crossover between the two regimes is estimated by the relation:

$$R^T(\mathbf{r}_T, \Delta E) = R^S e^{\beta(\Delta E - \mu_S)}. \tag{4.18}$$

The interference blockade is the only regime in which the current loses its dependence on the tip position. In fact, the current saturates to $I = -4eR^T$ for large positive biases, it is $I = -2eR^T$ at the tip-molecule resonance and $I = \frac{4}{5}eR^T$ at the substrate-molecule resonance. In Fig.

4.2 the letters T and S indicate regions where the current is proportional to the tip or substrate rate, respectively.

In the interference blocking regime, the enhanced sensitivity of the apparent molecular height to the setpoint can also be understood. From Eqs. (4.15) and (4.17) we can extract the relations for the constant current isosurfaces for a given setpoint I_0:

$$R^{\mathrm{T}} = \frac{I_0}{4ef_{\mathrm{S}}^{+}} \equiv K_{\mathrm{CB}}(I_0, V_b), \tag{4.19}$$

$$R^{\mathrm{T}} = \frac{I_0}{ef_{\mathrm{T}}^{-}} \left(1 - \frac{I_0}{eR^{\mathrm{S}} f_{\mathrm{S}}^{-}}\right)^{-1} \equiv K_{\mathrm{IB}}(I_0, V_b), \tag{4.20}$$

If, for a given choice of the parameters I_0 and V_b, it holds that $K_{\mathrm{IB}} = K_{\mathrm{CB}}$, the two associated contant current isosurfaces coincide. This is indeed, by construction, the case for the bias corresponding to the points 2 and 4 in Fig. 4.2 if the setpoint is chosen exactly as the one in the IV characteristics. When analyzing Eq. (4.20) we can see that K_{IB} diverges for $I_0 \to I_{\mathrm{crit}} = eR^{\mathrm{S}} f_{\mathrm{S}}^{-}$, while K_{CB} shows a completely regular behaviour. As $K_{IB} \to \infty$ the corresponding isosurface shrinks rapidly as it can be seen in Fig. 4.5. Moreover, in the vicinity of the interference blockade regime, the critical current I_{crit} represents an upper limit for the maximal setpoint current possible for a constant current STM scan. In fact, for $I_0 > I_{\mathrm{crit}}$ the constant K_{IB} turns negative and Eq. (4.20) can not be fulfilled for any tip position.

4.4 ROBUSTNESS OF THE EFFECT

Special consideration should be given to the robustness of the presented effect. Indeed we have presented so far the idealized situation in which the rotational symmetry of CuPc is assumed to be unperturbed with a consequently perfect degeneracy of the anionic ground states. Nevertheless this perfect degeneracy is not a necessary condition for the occurrence of the many-body interference effect: As shown in Ref. [DBDG09], the interference blocking scenario persists as far as the quasi-degeneracy is present, i.e. the splitting of the interfering energy levels is smaller than the tunneling coupling. In fact, if the tunneling coupling is strong enough, the indetermination principle does not allow to distinguish between the two quasi-degenerate states in the tunneling event and interference takes place. Moreover, since in STM experiments the tip tunneling rate can be controlled by varying the tip distance, the interference between quasi-degenerate states could be controlled by the tip position. The result would be the tuning of the interference NDC with the tip-molecule distance.

On the other hand, intra-molecular relaxation effects can influence interference NDC. In particular, dephasing can lead to the suppression of the offdiagonal elements of the density matrix. Since those elements are responsible for the emergence of the decoupling basis (4.10), strong

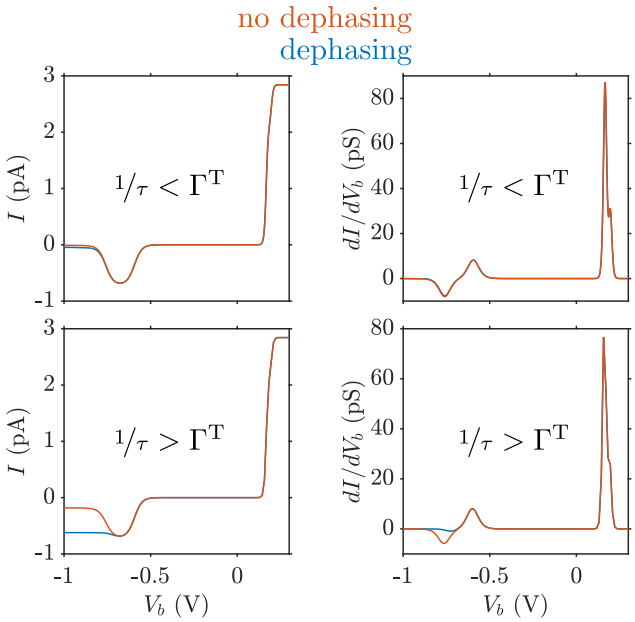

Figure 4.6: IV characteristics and differential conductance curves recorded for the full Hamiltonian Eq. (2.60) with transport model from Eq. (3.60), depending on the relaxation factor $\frac{1}{\tau}$ and if dephasing is possible (blue curves) or not (orange curves). Upper (lower) panels: $1/\tau$ is smaller (larger) than the mean tip tunneling rate.

dephasing can cause the interference NDC to disappear. As seen in Fig. 4.6, both relative size of $1/\tau$ in Eq. (3.54) as well as whether dephasing is enabled or not are influencing the NDC interference. For small $1/\tau$ and enabled dephasing, the effect is still there but the current is not completely blocked anymore. Instead there is residual current after the interference NDC dip. For larger values of $1/\tau$ the residual current after the interference NDC increases when dephasing is disabled; however if dephasing for larger $1/\tau$ is enabled, interference NDC is essentially spoiled. In contrast to the other results in this chapter, the curves in Fig. 4.6 were evaluated using the full many-body Hamiltonian, Eq. 2.60, as well as our transport formalism, Eq. (3.60) in its full glory.

5 NON-EQUILIBRIUM SPIN-CROSSOVER

SCO is a quantum mechanical phenomenon where metalorganic complexes undergo a transition from a low spin (LS) to a high spin (HS) state [CS31] under the influence of external stimuli like pressure, temperature and strain [GGG00]. Prominent candidates showing SCO are complexes containing Co and Fe due to their favorable electronic configurations, ranging from d^5 in Fe(III) over d^6 in Fe(II) to d^7 in Co(II) [SBH61, GGG00, MBF+11]. Among those also the family of phthalocyanines is represented through iron phthalocyanine (FePc) [CFJ+82, KMZ+86, MGD+12, GMN+12].

A theoretical explanation for *static* SCO can be given by ligand field theory [GO57]: Because of interaction with the surrounding ions and electrons in the ligand, the degenerate d orbitals of a metal in a metalorganic compound are splitting up. For example, in a complex with octahedral symmetry they split into twofold degenerate e_g and threefold degenerate t_{2g} orbitals, respectively. The interplay between the many-body exchange interaction between the d-electrons and the size of the splitting Δ finally determines the spin state of the metal center, see Fig. 5.1. Manipulation of the ligand in a metalorganic compound thus allows for an indirect control of its spin state.

In this chapter we investigate the appearance of *non-equilibrium* SCO in CuPc caused by population inversion to an excited neutral HS state. Furthermore, we illustrate that the resulting effective ground state of the molecule can be influenced via variation of the tip position or the bias voltage across the junction. The most important prerequisites for this effect to occur are the energetic proximity of a neutral excited HS state to the anionic ground state, which can be influenced by varying the workfunction of the substrate, and a strong asymmetry between tip and substrate tunneling rates, which is a natural property of STM setups. Control over the workfunction can be achieved by choosing different materials or crystallographic orientations for the substrate, with effects analogous to a discrete gating of the molecule. Several

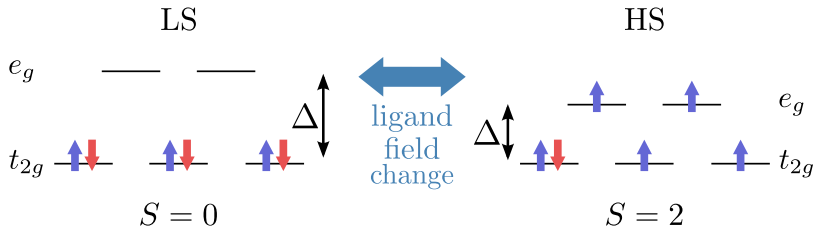

Figure 5.1: Scheme showing two different spin states for a d^6 configuration, depending on the strength Δ of the ligand field splitting.

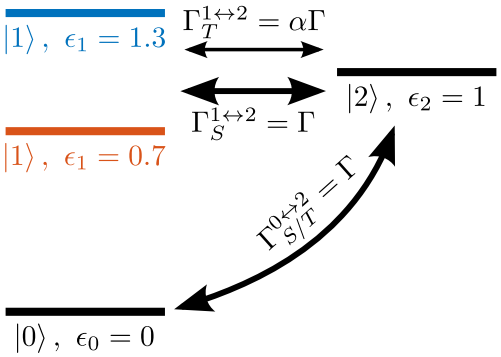

Figure 5.2: Sketch of the three state model, where state $|1\rangle$ is shown for two different energies.

approaches to gate an STM junction have been also very recently investigated [FTKLSdz+12, Bou14, MBNE+15].

5.1 MINIMAL MODEL FOR POPULATION INVERSION

Before we turn to the realistic model of CuPc in an STM setup, we explain the basic mechanism of bias-induced population inversion by means of a simple model: Population inversion to an excited state can be easily investigated analytically in a three state model using detailed balance equations. Consider the populations P_i of the three states $|i\rangle$ with energies ϵ_i, $i = 0, 1, 2$, see Fig. 5.2 (a). Then we can establish the following system of equations for the steady state ($t \to \infty$):

$$\begin{aligned}
\sum_\eta \Gamma_\eta^{0\to 2} f_\eta^+(\epsilon_2 - \epsilon_0) P_0 &= \sum_\eta \Gamma_\eta^{2\to 0} f_\eta^-(\epsilon_2 - \epsilon_0) P_2, \\
\sum_\eta \Gamma_\eta^{1\to 2} f_\eta^+(\epsilon_2 - \epsilon_1) P_1 &= \sum_\eta \Gamma_\eta^{2\to 1} f_\eta^-(\epsilon_2 - \epsilon_1) P_2, \\
P_0 + P_1 + P_2 &= 1
\end{aligned} \tag{5.1}$$

where the $\Gamma_\eta^{i\to j}$ are the rates for the system to transition from state $|i\rangle$ to $|j\rangle$ via tunneling of an electron to or from the lead denoted by η, respectively.

Altough Eq. (5.1) can be solved exactly in the present form, we assume for the sake of simplicity:

$$\begin{aligned}
\Gamma_{\mathrm{S}}^{i\to j} &= \Gamma, \\
\Gamma_{\mathrm{T}}^{0\to 2} &= \Gamma_{\mathrm{T}}^{2\to 0} = \Gamma, \\
\Gamma_{\mathrm{T}}^{1\to 2} &= \Gamma_{\mathrm{T}}^{2\to 1} = \alpha\Gamma.
\end{aligned} \tag{5.2}$$

Then, by introducing

$$A := \frac{f_{\mathrm{T}}^-(\epsilon_2 - \epsilon_0) + f_{\mathrm{S}}^-(\epsilon_2 - \epsilon_0)}{f_{\mathrm{T}}^+(\epsilon_2 - \epsilon_0) + f_{\mathrm{S}}^+(\epsilon_2 - \epsilon_0)}, \tag{5.3}$$

$$B := \frac{\alpha f_{\mathrm{T}}^+(\epsilon_2 - \epsilon_1) + f_{\mathrm{S}}^+(\epsilon_2 - \epsilon_1)}{\alpha f_{\mathrm{T}}^-(\epsilon_2 - \epsilon_1) + f_{\mathrm{S}}^-(\epsilon_2 - \epsilon_1)}, \tag{5.4}$$

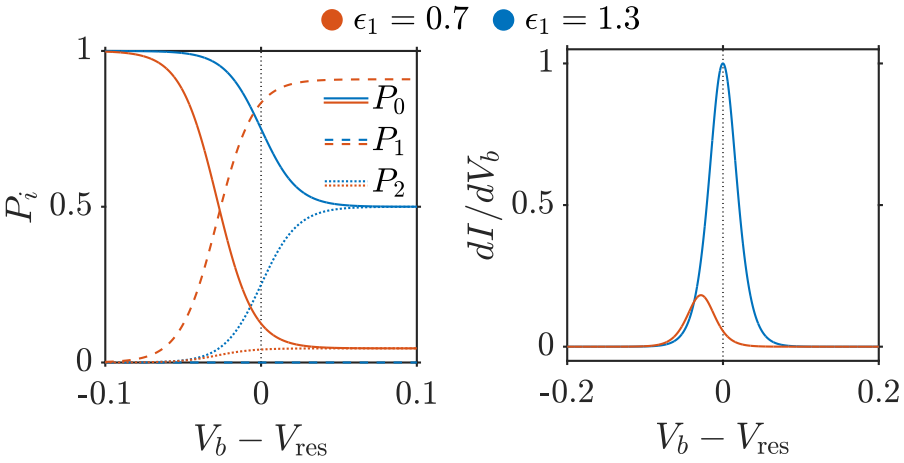

Figure 5.3: Left panel: Populations of the three states depending on the bias voltage V_b around the expected position of the resonance V_{res}. Right panel: Differential conductance. In both panels, blue curves are calculated for $\epsilon_1 = 1.3$ and orange curves for $\epsilon_1 = 0.7$.

we can write the solution for Eq. (5.1) around the tip resonance $V_{\mathrm{res}} = \frac{1}{c_{\mathrm{T}}}(\epsilon_2 - \epsilon_0)$ as:

$$\begin{aligned} P_1 &= (1 + B(1 + A))^{-1}, \\ P_0 &= AB\, P_1, \\ P_2 &= B\, P_1. \end{aligned} \tag{5.5}$$

The current through the system then can be evaluated as

$$\begin{aligned} I = {} & f_{\mathrm{T}}^{+}(\epsilon_2 - \epsilon_0)\, P_0 + \alpha f_{\mathrm{T}}^{+}(\epsilon_2 - \epsilon_0)\, P_1, \\ & - \Big(f_{\mathrm{T}}^{-}(\epsilon_2 - \epsilon_0) + f_{\mathrm{T}}^{-}(\epsilon_2 - \epsilon_1) \Big)\, P_2. \end{aligned} \tag{5.6}$$

In Fig. 5.3 we show the evolution of the different populations P_i (left panel) and the differential conductance $\frac{dI}{dV_b}$ (right panel) for the following parameter choice: $\epsilon_0 = 0$, $\epsilon_2 = 1$, $k_b T = 0.01$, $c_{\mathrm{T}} = 0.85$, $\Gamma = 1$ and $\alpha = \frac{1}{20}$. If ϵ_1 is well above ϵ_2 (as is the case for the blue curves) the peak position in the differential conductance coincides with the expected position V_{res}. When ϵ_1 is around ϵ_2, population inversion is occuring (the orange curves), as the system has finite possibility to end up in state $|1\rangle$.

One can also derive a condition for the energetic proximity of $|2\rangle$ to $|1\rangle$: At resonance, when $V_b = V_{\mathrm{res}} = \frac{1}{c_{\mathrm{T}}}(\epsilon_2 - \epsilon_0)$, the system has an energy of $c_{\mathrm{S}} V_{\mathrm{res}} = \frac{c_{\mathrm{S}}}{c_{\mathrm{T}}}(\epsilon_2 - \epsilon_0)$ at disposal to undergo a substrate transition. Therefore we can derive a condition for the energy difference $\epsilon_2 - \epsilon_1$:

$$\epsilon_2 - \epsilon_1 \overset{!}{\leq} \frac{c_{\mathrm{S}}}{c_{\mathrm{T}}}(\epsilon_2 - \epsilon_0)\,. \tag{5.7}$$

Hence, for population inversion to occur, the state $|1\rangle$ can energetically be even above $|2\rangle$. The smallness of α supports the inversion additionally, since tunneling out of state $|1\rangle$ is suppressed. The smaller α the

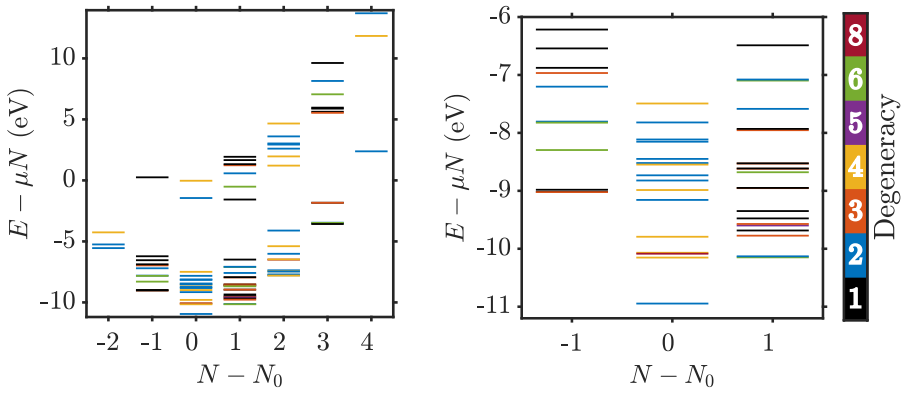

Figure 5.4: Left panel: Full many-body spectrum of CuPc. Right panel: Cationic, neutral and anionic low-energy parts of the spectrum.

more drastic the population inversion becomes. Normal behaviour also can be restored for $\epsilon_1 < \epsilon_2$: When $\alpha \gg 1$, depopulation of $|1\rangle$ happens so fast that the dynamics of the system is basically governed by $|0\rangle$ and $|2\rangle$ and the peak in the differential conductance moves to the expected position again.

When we postulate that $P_2 = 0$, meaning that the state $|2\rangle$ gets depopulated instantaneously, we can even determine the shift of the resonance analytically by finding the maximum of $\frac{\mathrm{d}P_1}{\mathrm{d}V_b}$:

$$\Delta V_{\mathrm{res}} = \frac{k_{\mathrm{B}}T}{c_{\mathrm{T}}} \log \frac{\alpha}{1+\alpha}. \tag{5.8}$$

Putting the numbers of our previous example into Eq. (5.8) yields $\Delta V_{\mathrm{res}} \approx -0.036$. Altough the conditions for the derivation of Eq. (5.8) are as such unphysical, the latter can be used as a rule of thumb; namely that the shift of the resonance increases with both increasing temperature and stronger asymmetry between tip and substrate rates (smaller α).

5.2 SPIN-CROSSOVER IN CUPC

As discussed in Sec. 3.4, the experimental setup is similar to that of Ref. [SSR11]. For the calculation of the many-body spectrum, the Hamiltonian $\hat{H}_{\mathrm{mol}}$ in Eq. (2.60) was used.

5.2.1 *The excited state structure of CuPc*

Exact numerical diagonalization of $\hat{H}_{\mathrm{mol}}$ yields the many-body eigenenergies E_{Nm} and eigenstates $|Nm\rangle$ of the molecule, labelled after particle number N and state index m, see Fig. 5.4. Since in an STM experiment the molecule is in contact with the substrate and is able to exchange electrons, it is necessary to consider a grandcanonical ensemble

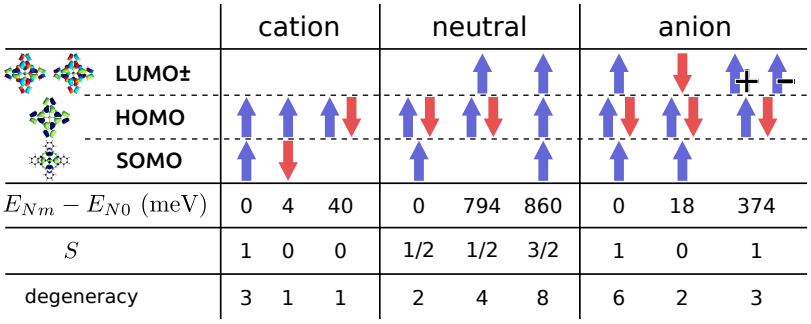

	cation			neutral			anion		
$E_{Nm} - E_{N0}$ (meV)	0	4	40	0	794	860	0	18	374
S	1	0	0	1/2	1/2	3/2	1	0	1
degeneracy	3	1	1	2	4	8	6	2	3

Figure 5.5: Scheme of the lowest-lying many-body states of CuPc. As the actual states are linear combinations of several Slater determinants, only dominant contributions are shown.

$\hat{H}_{\text{mol}} - \mu\hat{N}$ where μ is the chemical potential of the substrate which is given by its negative workfunction, $\mu = -\phi_0$.

A schematic depiction of the low lying excited states of CuPc is shown in Fig. 5.5. The neutral ground state has a doublet structure (with total spin $S = \frac{1}{2}$) coming from the doubly filled HOMO and the unpaired spin in the SOMO. The cationic and anionic ground states have triplet structures ($S = 1$). The former has a singly filled HOMO, the latter a singly filled LUMO orbital which form spin triplets (and singlets, $S = 0$, for the first excited states) with the singly filled SOMO. Importantly, the orbital degeneracy of the LUMO makes up for an additional twofold multiplicity of the anionic ground and first excited states. The first excited state of the neutral molecule is found to be also a doublet ($S = \frac{1}{2}$) with additional twofold orbital degeneracy. Finally, the second excited state shows a spin quadruplet structure ($S = \frac{3}{2}$) together with twofold orbital degeneracy.

5.2.2 *Transport calculations*

The results of our transport calculations are presented in Fig. 5.6. In panels (a,d,g) we show constant height current maps, constant current STM images in (b,e,h) and in (c,f,i) maps of the expectation value of the total spin of the molecule depending on the tip position, $S_{\mathbf{r}_\text{T}} = \sqrt{\langle\hat{S}^2\rangle_{\mathbf{r}_\text{T}} + \frac{1}{4}} - \frac{1}{2}$ where $\langle\hat{S}^2\rangle_{\mathbf{r}_\text{T}} = \text{Tr}_{\text{mol}}\left(\hat{S}^2\rho^{\infty}_{\text{red}}(\mathbf{r}_\text{T})\right)$. The constant height and spin maps are each taken at a tip-molecule distance of 5 Å. The upper three panels (a,b,c) are for a workfunction of $\phi_0 = 4.65$ eV and a bias voltage of $V_b = -2.72$ V. At this position the cationic resonance is occuring. Since the difference between neutral and cationic ground state is the occupation of the HOMO (see Fig. 5.5), tunneling occurs via this orbital and the current maps (a,b) resemble its structure. With the same work function $\phi_0 = 4.65$ eV, the anionic resonance is taking place at the positive bias $V_b = 0.81$ V, see Fig. 5.6(d,e). For equivalent reasons as in the former case, tunneling is happening via the LUMO and the spatial dependence of the cur-

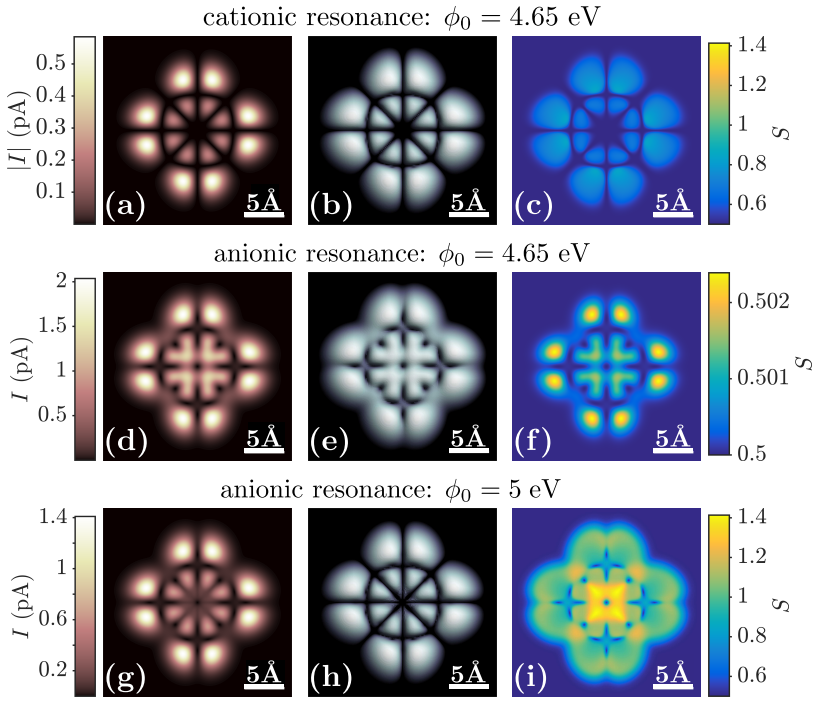

Figure 5.6: Constant height current maps (a,d,g), constant current maps (b,e,h) and maps of the system's total spin S (c,f,i). Constant height and spin maps are taken at a tip-molecule distance of 5 Å, constant current maps at currents $I = 0.5$, 0.75, 1.0 pA for panels (c), (f), and (i), respectively.

rent resembles the topography of this orbital. Panels (g,h,i) instead are recorded at $\phi_0 = 5$ eV, again at the anionic resonance which is now shifted to $V_b = 1.38$ V due to the larger workfunction. Panel (g) is puzzling. Despite being an anionic resonance, it closely resembles the HOMO, cf. panels (a),(b). A closer inspection reveals also an alikeness with the LUMO (see panel (d)) but with additional diagonal nodal planes, matching the nodal plane structure of the HOMO. When observing the constant current map in panel (h), and comparing it with panels (b) and (e), this statement becomes more evident. This anomalous topography can not be explained by single orbital tunneling.

Panels (c), (f) and (i) reveal the tip-position dependent expectation value of the total spin. At the standard anionic transition, panel (f), the spin remains essentially constant. At the standard cationic transition, panel (c), the rather homogeneous enhancement of the molecular spin is due to small populations of a large number of excited states, made accessible by the large resonance bias ($V_{\text{res}} = -2.7$ V). The anomalous anionic transition, panel (i), shows the largest variation of the molecular spin, concentrated at the positions of the anomalous current suppression, compare panels (g) and (d). To explain the unconventional properties shown in Fig. 5.6, we examine bias traces taken at different tip positions and values of the workfunction. Figure 5.7(a) shows a

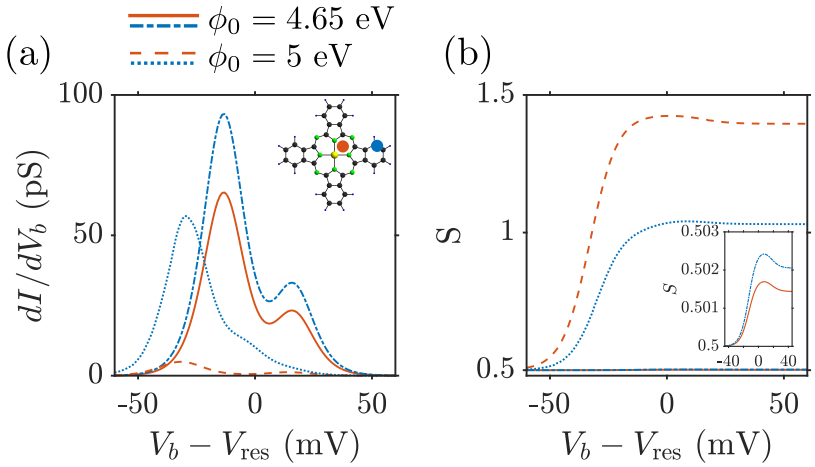

Figure 5.7: (a) Differential conductance and (b) total spin curves for different tip positions and workfunctions around the bias $V_{\mathrm{res}}(\phi_0)$ of the anionic resonance. The inset in (b) shows the change of the spin for the standard case in magnification.

shift of the anionic resonant peak in the $\frac{dI}{dV}$ for the anomalous case. The value V_{res} at which the peak is expected is given by

$$V_{\mathrm{res}}(\phi_0) = \frac{1}{\alpha_{\mathrm{T}}|e|}\left(E_{N_0+1,0} - E_{N_0,0} - \delta_{\mathrm{ic}} + \phi_0\right), \tag{5.9}$$

where α_{T} is the fraction of bias drop between tip and molecule, and $E_{N,0}$ is the energy of the N-particle ground state.

The shift of the resonance to lower biases seen in Fig. 5.7(a) suggests the appearance of a population inversion from the neutral ground state to an excited state. Transitions from the latter to the anionic ground state open in fact at much lower biases. Also the evolution of the spin of the molecule shown in Fig. 5.7(b) reinforces this proposition. In the anomalous case, the change of the system from a low to a high spin state, as well as the saturation of the spin, can be clearly seen. This contrasts the normal anionic transition, where only a marginal change is observable.

In Fig. 5.8 we show the evolution of the eigenvalues of the stationary density matrix ρ^{∞}_{red}, *i*.e. the populations of the physical basis [DBDG09], around the anionic resonance $V_{\mathrm{res}}(\phi_0)$, depending on workfunction and tip position. In the standard case (left panel of Fig. 5.8), the ground state of the system is always the neutral ground state. For the anomalous case (middle and right panels of Fig. 5.8) however, the picture changes dramatically, as there is a remarkable depopulation of the neutral ground state in favor of different excited states, depending on the position of the tip.

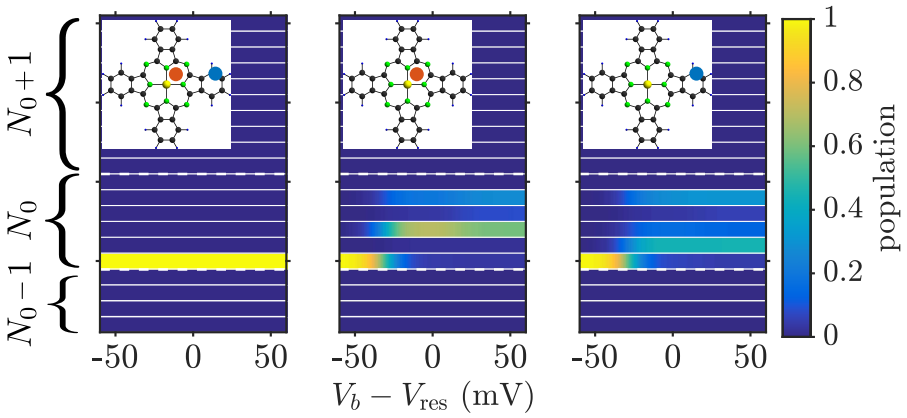

Figure 5.8: Populations of the density matrix around $V_{\mathrm{res}}(\phi_0)$. Left panel: standard case, $\phi_0 = 4.65$ eV. Middle (right) panel: anomalous case, $\phi_0 = 5$ eV, with tip near the center (outer on the ligand).

5.2.3 *The mechanism of SCO in CuPc*

We focus now on the mechanism yielding the population inversion with associated spin-crossover. In the standard case, at sufficiently high bias, the transition from the neutral to the anionic ground state is opening, and tunneling of an electron into the LUMO brings the molecule into the anionic ground state. By consecutive tunneling to the substrate, the system goes back into its neutral ground state, see Fig. 5.9 for a simple sketch. Since the tunneling rates to the substrate are much larger than their tip counterparts, the system stays essentially in the neutral ground state with spin $S = \frac{1}{2}$.

Also in the anomalous case an initial tunneling event brings the molecule into the anionic ground state. However, from there, due to finite temperature and proximity of the many-body eigenenergies, the system has a finite probability to go into a neutral excited state by releasing an electron to the substrate. The position of the tip and the structure of these excited states themselves then determine the stationary state: The molecule can only return to its neutral ground state by successive transitions to the anionic ground state via the tip, and from there to the neutral ground state via the substrate. However, the former process acts as a bottleneck and depends on the tip position. Leaving the first excited state ($S = \frac{1}{2}$) requires tunneling into the SOMO, while leaving the second excited state ($S = \frac{3}{2}$) would require tunneling into the HOMO. Additionally, near the center of the molecule the HOMO is vanishing, whereas on the outer ligand part the SOMO has little to no amplitude. Therefore, tunneling into these orbitals at the respective positions is strongly suppressed and the system ultimately ends up in the corresponding neutral excited states.

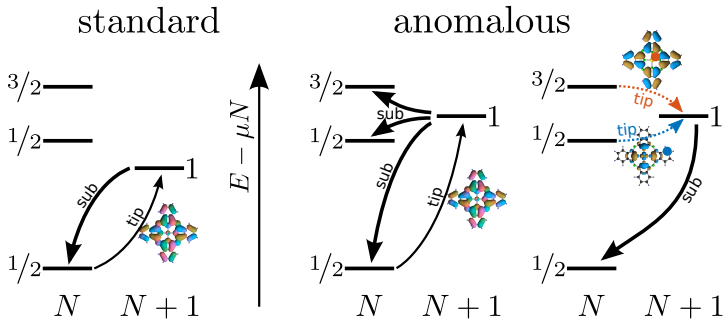

Figure 5.9: Simplified sketch of the tunnelling processes at the anionic resonance for the standard ($\phi_0 = 4.65$ eV) and the anomalous ($\phi_0 = 5$ eV) case. In the latter population inversion takes place. The colors of the arrows denote tip positions where the corresponding transition acts as a bottleneck: Orange (blue) stands for the center (the outer ligand) of CuPc.

5.3 ENERGETIC REQUIREMENTS

As shown in Sec. 5.1, the energetic proximity of the neutral excited state to the anionic ground state is a key requirement for population inversion to occur. In the following section we will develop constraints on the work function ϕ_0 depending on elementary molecular quantities like ionization potential, electron affinity and optical gap to predict possible other molecules that could show population inversion.

Using the grandcanonical ensemble with chemical potential $\mu = -\phi_0$, we can write the energy difference Δ_{ani} of the first neutral excited state to the anionic ground state as

$$\begin{aligned}\Delta_{\text{ani}} &= (E_{N_0,1} + \phi_0 N_0) - (E_{N_0+1,0} + \phi_0(N_0+1)) = E_{N_0,1} - E_{N_0+1,0} - \phi_0 \\ &= \Delta_{\text{opt}} + EA - \phi_0, \end{aligned} \tag{5.10}$$

where we introduced the optical gap $\Delta_{\text{opt}} = E_{N_0,1} - E_{N_0,0}$ and the electron affinity $EA = E_{N_0,0} - E_{N_0+1,0}$. We can also rewrite V_{res} for the anionic resonance:

$$V_{\text{res}} = \frac{1}{c_{\text{T}}} \left(E_{N_0+1,0} - E_{N_0,0} + \phi_0\right) = \frac{1}{c_{\text{T}}} \left(\phi_0 - EA\right). \tag{5.11}$$

Since $\Delta_{\text{opt}} > 0$, we have, analogous to Eq. (5.7),

$$\Delta_{\text{cat}} \leq \frac{c_{\text{S}}}{c_{\text{T}}} \left(\phi_0 - EA\right), \tag{5.12}$$

$$\Delta_{\text{opt}} + EA - \phi_0 \leq \frac{c_{\text{S}}}{c_{\text{T}}} \left(\phi_0 - EA\right), \tag{5.13}$$

$$\phi_0 \geq EA + \frac{\Delta_{\text{opt}}}{1 + \frac{c_{\text{S}}}{c_{\text{T}}}}. \tag{5.14}$$

On the other hand, the cationic ground state has to be sufficiently distanced energetically, so that the system can not make a transition to it, which would spoil the population inversion. Thus, the energy

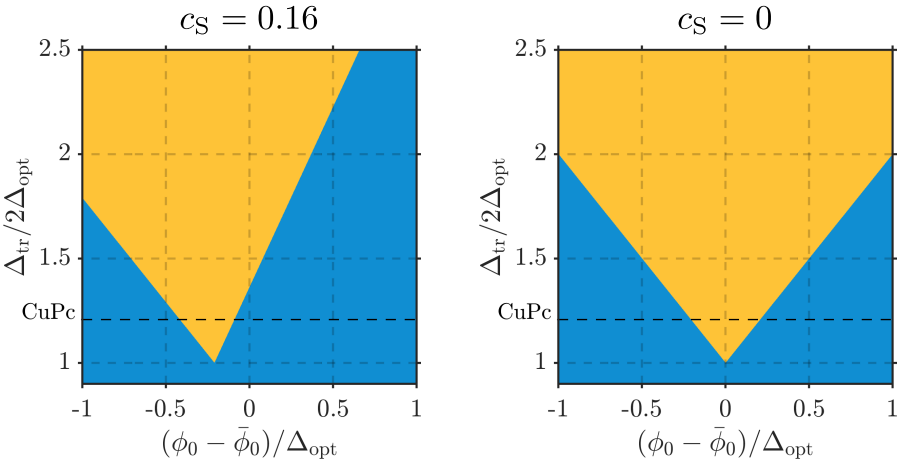

Figure 5.10: Diagrams demonstrating the conditions given in Eq. (5.19). Left (right) panel shows in yellow color where population inversion can occur for given values of Δ_{opt}, Δ_{tr}, ϕ_0 and $\bar{\phi}_0$ for finite (vanishing) bias drop c_S at the substrate. The dashed line depicts the value of $\frac{\Delta_{tr}}{2\Delta_{opt}}$ of CuPc obtained in this work.

difference Δ_{cat} between the first neutral excited state and the cationic ground state,

$$\Delta_{cat} = E_{N_0-1,0} - E_{N_0,1} - \phi_0 = IP - \Delta_{opt} - \phi_0, \tag{5.15}$$

has to be larger than the available energy at the anionic resonance:

$$\Delta_{cat} > \frac{c_S}{c_T}(\phi_0 - EA). \tag{5.16}$$

Here we have defined the ionization potential $IP = E_{N_0-1,0} - E_{N_0,0}$. This yields another constraint on ϕ_0,

$$\phi_0\left(1 + \frac{c_S}{c_T}\right) < IP + \frac{c_S}{c_T}EA - \Delta_{opt}. \tag{5.17}$$

Using the definition of the transport gap $\Delta_{tr} = IP - EA$, we can put Eqs. (5.14) and (5.17) together in the following form:

$$\frac{\Delta_{opt}}{1 + \frac{c_S}{c_T}} + EA \leq \phi_0 < \frac{\Delta_{tr} - \Delta_{opt}}{1 + \frac{c_S}{c_T}} + EA. \tag{5.18}$$

Introducing $\bar{\phi}_0 = \frac{EA+IP}{2}$, which is the workfunction for which the ground state spectrum is symmetric with respect to the neutral ground state, i.e. $E_{N_0+1,0} - E_{N_0,0} + \phi_0 = E_{N_0-1,0} - E_{N_0,0} - \phi_0$, we can recast Eq. (5.18) in a dimensionless form:

$$\frac{c_T}{c_T + c_S} - \frac{\Delta_{tr}}{2\Delta_{opt}} \leq \frac{\phi_0 - \bar{\phi}_0}{\Delta_{opt}} < \frac{c_T - c_S}{c_T + c_S}\frac{\Delta_{tr}}{2\Delta_{opt}} - \frac{c_T}{c_T + c_S}. \tag{5.19}$$

In Fig. 5.10 we graphically show the constraints on the molecular properties like Δ_{opt}, Δ_{tr} and $\bar{\phi}_0$ and the workfunction ϕ_0 for two different values of the substrate bias drop c_S: The area colored in yellow

depicts where population inversion can occur. Hereby, its right edge reflects the critical value for Δ_{cat}, while its left edge indicates the critical value for Δ_{ani}, cf. Eqs. (5.16) and (5.12), respectively. For $c_{\mathrm{S}} = 0$ in the symmetric configuration, $\phi_0 - \bar{\phi}_0 = 0$, Eq. (5.19) reveals that the transport gap must be at least twice as large as the optical gap,

$$\Delta_{\mathrm{tr}} > 2\Delta_{\mathrm{opt}}. \tag{5.20}$$

For a finite deviation from the symmetric configuration, $\phi_0 - \bar{\phi}_0 \neq 0$, we get a minimal condition for ϕ_0, namely

$$\left| \frac{\phi_0 - \bar{\phi}_0}{\Delta_{\mathrm{opt}}} \right| < \frac{\Delta_{\mathrm{tr}}}{2\Delta_{\mathrm{opt}}} - 1. \tag{5.21}$$

The two conditions given in Eqs. (5.20) and (5.21) can be nicely checked in the right panel of Fig. 5.10. They can help to determine if a particular molecule can display population inversion on a given substrate. However, since there is a finite bias drop c_{S} across the substrate, they should be regarded as thumb rules. Note that, although not explictily included in this Section, charging-dependent contributions like δ_{ic} can be absorbed by

$$EA \to EA + \delta_{\mathrm{ic}}, \tag{5.22}$$

$$IP \to IP - \delta_{\mathrm{ic}}, \tag{5.23}$$

$$\Delta_{\mathrm{tr}} \to \Delta_{\mathrm{tr}} - 2\delta_{\mathrm{ic}} \tag{5.24}$$

without changing the relations.

6

MAGNETOTRANSPORT THROUGH COPPER PHTHALOCYANINE

Spin-orbit interaction (SOI) can play a major role in molecular spintronics. For example, in combination with the configuration of the non-magnetic component (organic ligand), it is known to be essential in establishing magnetic anisotropy in high-spin molecular magnets [GSV06]. Effective spin-Hamiltonians are commonly used to describe this anisotropy, and usually well capture the low energy properties of these systems, see e.g. Ref. [MPD+10]. Such effective Hamiltonians have been derived microscopically for widely studied molecular magnets like Fe_8, Fe_4 and Mn_{12} [CCS+13]. Recently, magnetic anisotropy effects could be directly probed by magnetotransport spectroscopy for Fe_4 in quantum dot setups [MBG+15, BGvdZ15]. An interesting question is hence if other classes of metallorganic compounds, like the widely studied metal phthalocyanines [LS01, MRK+12], exhibit magnetic anisotropy induced by the interplay of electronic correlations and SOI. Indeed, in an XMCD analysis CuPc was found to exhibit enormous anisotropies in both spin and orbital dipole moments [SMC+10]. Furthermore, recent experimental findings for cobalt pththalocyanine in an STM setup [SID+15] suggest that many-body correlations play an important role in the interpretation of the transport measurements.

In this chapter we add the SOI to our analysis. We find that it further removes the triplet degeneracy by inducing splittings of few tenths of meV. Moreover, in combination with exchange correlations, it produces a magnetic anisotropy which can in turn be captured by an effective spin Hamiltonian.

6.1 SPIN-ORBIT, EXCHANGE AND MAGNETIC FIELDS

The focus of this section is the establishment of a minimal model Hamiltonian for an isolated CuPc molecule capable to account for both electron-electron interaction and spin-orbit coupling effects. In its most general form such Hamiltonian reads

$$\hat{H}_{\mathrm{mol}} = \hat{H}_0 + \hat{V}_{\mathrm{ee}} + \hat{V}_{\mathrm{SO}}, \tag{6.1}$$

where the single-particle Hamiltonian of the molecule is given by $\hat{H}_0$, $\hat{V}_{\mathrm{ee}}$ describes electronic interactions and $\hat{V}_{\mathrm{SO}}$ accounts for the SOI.

6.1.1 *Spin-orbit coupling in the frontier orbitals basis*

A perturbative contribution to the bare one-body Hamiltonian $\hat{H}_0$ relevant in molecular systems is provided by the SOI. In the following we derive an effective spin-orbit coupling operator acting on the subset of frontier orbitals. The atomic SOI operator reads

$$\hat{V}_{\mathrm{SO}} = \sum_{\alpha,\ell_\alpha} \xi_{\ell_\alpha} \hat{\boldsymbol{\ell}}_\alpha \cdot \hat{\boldsymbol{s}}_\alpha, \tag{6.2}$$

where α and ℓ_α run over all atoms and shells, respectively. By evaluating Eq. (6.2) only on the central copper atom, i.e. $\ell = 2$ and $\alpha = \mathrm{Cu}$, $\hat{V}_{\mathrm{SO}}$ in second quantization is given by

$$\begin{aligned}\hat{V}_{\mathrm{SO}} = \xi_{\mathrm{Cu}} \Bigg(& \sum_{m=-2}^{2} \frac{m}{2} \left(\hat{d}^\dagger_{m\uparrow} \hat{d}_{m\uparrow} - \hat{d}^\dagger_{m\downarrow} \hat{d}_{m\downarrow} \right) \\ & + \sqrt{\frac{3}{2}} \left(\hat{d}^\dagger_{0\downarrow} \hat{d}_{-1\uparrow} + \hat{d}^\dagger_{1\downarrow} \hat{d}_{0\uparrow} + \mathrm{h.c.} \right) \\ & + \left(\hat{d}^\dagger_{2\downarrow} \hat{d}_{1\uparrow} + \hat{d}^\dagger_{-1\downarrow} \hat{d}_{-2\uparrow} + \mathrm{h.c.} \right) \Bigg),\end{aligned} \tag{6.3}$$

where $\hat{d}^\dagger_{m\sigma}$ creates an electron with spin σ on the copper atom in the orbital specified by $(\ell = 2, m)$. For an electron in the 3d-shell of Cu we use $\xi_{\mathrm{Cu}} \approx 100$ meV [BBS93]. Projecting Eq. (6.3) onto the minimal set of frontier orbitals then yields:

$$\begin{aligned}\hat{V}_{\mathrm{SO}} = & \lambda_1 \sum_{\tau=\pm} \tau \left(\hat{d}^\dagger_{L\tau\uparrow} \hat{d}_{L\tau\uparrow} - \hat{d}^\dagger_{L\tau\downarrow} \hat{d}_{L\tau\downarrow} \right) \\ & + \lambda_2 \left(\hat{d}^\dagger_{S\uparrow} \hat{d}_{L-\downarrow} + \hat{d}^\dagger_{L+\uparrow} \hat{d}_{S\downarrow} + \mathrm{h.c.} \right),\end{aligned} \tag{6.4}$$

where $\lambda_1 = \frac{1}{2}\xi_{\mathrm{Cu}} |c_L|^2 = 0.47$ meV and $\lambda_2 = \xi_{\mathrm{Cu}} \frac{c_S c_L}{\sqrt{2}} = 6.16$ meV are now effective spin-orbit coupling constants. A similar analysis of SOI in CuPc, laying more focus on the central Cu atom, can be found in Ref. [Yu12].

Finally, many body eigenenergies E_{Nk} and eigenstates $|Nk\rangle$, labelled after particle number N and state index k, are obtained by exact numerical diagonalization of $\hat{H}_{\mathrm{mol}}$ in the frontier orbitals basis. Despite numerically tractable, the problem described by $\hat{H}_{\mathrm{mol}}$ is still highly intricate, as the Fock space has dimension $4^4 = 256$. In reality, though, only few low-lying many-body states are relevant at low energies, what enables further simplification and even an analytical treatment, as discussed below.

In the following we will analyze the neutral and anionic low-energy part of the many-body spectrum of CuPc and establish an effective Hamiltonian which enables us to analyze the low-energy behaviour in a more lucid way. To this extent, we start by observing that $\hat{H}_{\mathrm{mol}}$ (in the considered particle number subblocks) contains different energy

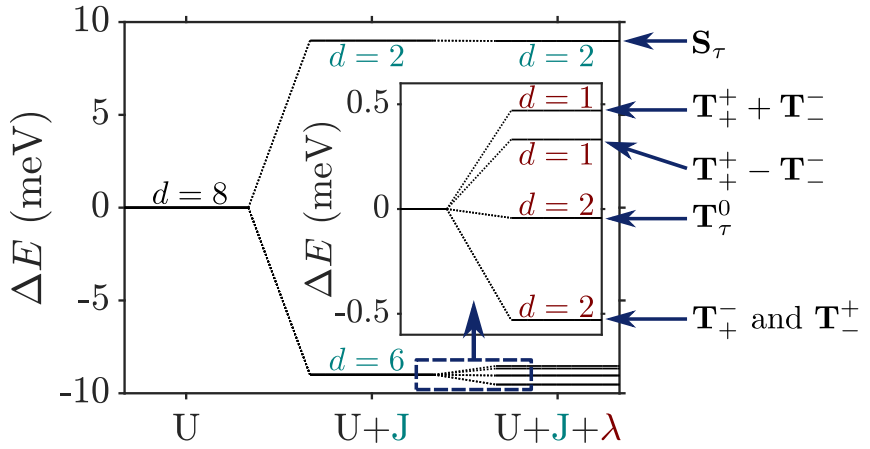

Figure 6.1: Lowest lying anionic states of CuPc, together with their grade of degeneracy d. Without exchange and SOI, the anionic ground state is eightfold degenerate. When exchange interaction between SOMO and LUMOs is introduced, the degeneracy is lifted, yielding two triplets and two singlets because of the orbital degeneracy of the LUMO. SOI further splits the triplet states, generating a twofold degenerate anionic ground state consisting of the states $\mathbf{T}_{+}^{-}$ and $\mathbf{T}_{-}^{+}$.

scales, in particular, $U > J > \lambda$, what suggests a hierarchy of steps. We use U, J and λ to denote the set of all Hubbard-like parameters (U_i, U_{ij}), all exchange parameters $(J_{ij}^{\mathrm{ex}}, J_{ij}^{\mathrm{p}}, \tilde{J}_{ijk}^{\mathrm{p}})$ and all SOI parameters (λ_i), respectively. As a first step we set both the exchange (J) and SOI (λ) contributions to $\hat{H}_{\mathrm{mol}}$ to zero and determine the neutral and anionic ground states. In a second and third step exchange and SOI are added, respectively.

6.1.1.1 *Neutral low-energy spectrum*

In the neutral low-energy part of the spectrum, we retain the two spin-degenerate ground states of $\hat{H}_{\mathrm{mol}}(J = 0, \lambda = 0)$,

$$|N_0, \sigma\rangle := \hat{d}_{S\sigma}^{\dagger} |\Omega\rangle \,, \tag{6.5}$$

with corresponding energy $E_{N_0}^{\mathrm{g}}$. Here we defined $|\Omega\rangle = \hat{d}_{H\uparrow}^{\dagger} \hat{d}_{H\downarrow}^{\dagger} |0\rangle$. The ground states in Eq. (6.5) are neither affected by $\hat{V}_{\mathrm{SO}}$ nor by the exchange terms in Eq. (2.60). Trivially, the effective Hamiltonian in the basis of $|N_0, g\sigma\rangle$ reads:

$$\mathrm{H}_0^{N_0} = E_{N_0}^{\mathrm{g}}. \tag{6.6}$$

In principle Eq. (2.60) also contains terms which act on the neutral ground state, like for example pair hopping terms which are proportional to $\tilde{J}_{HL+L-}^{\mathrm{p}}$, and cause admixtures with other many-body states. However, according to our full numerical calculations, these admixtures are rather small and do not affect transitions between neutral and anionic states.

6.1.1.2 *Anionic low-energy spectrum*

In the anionic low-energy part of the spectrum of $\hat{H}_{\mathrm{mol}}(J=0,\lambda=0)$, we find an eightfold degenerate ground state:

$$|N_0+1,\tau\sigma\sigma'\rangle := \hat{d}^\dagger_{S\sigma}\hat{d}^\dagger_{L\tau\sigma'}\,|\Omega\rangle\,, \tag{6.7}$$

with corresponding energy $E^{\mathrm{g}}_{N_0+1}$. The eightfold degeneracy comes from the two unpaired spins in either SOMO or LUMO and the orbital degeneracy of the LUMO orbitals. In order to make the anionic eigenstates also eigenstates of the spin operators $\hat{\mathbf{S}}^2$ and $\hat{S}_z$, they can be rewritten as

$$\begin{aligned}
|\mathbf{S}_\tau\rangle &= \frac{1}{\sqrt{2}}\left(\hat{d}^\dagger_{S\uparrow}\hat{d}^\dagger_{L\tau\downarrow} - \hat{d}^\dagger_{S\downarrow}\hat{d}^\dagger_{L\tau\uparrow}\right)|\Omega\rangle\,,\\
|\mathbf{T}^+_\tau\rangle &= \hat{d}^\dagger_{S\uparrow}\hat{d}^\dagger_{L\tau\uparrow}\,|\Omega\rangle\,,\\
|\mathbf{T}^0_\tau\rangle &= \frac{1}{\sqrt{2}}\left(\hat{d}^\dagger_{S\uparrow}\hat{d}^\dagger_{L\tau\downarrow} + \hat{d}^\dagger_{S\downarrow}\hat{d}^\dagger_{L\tau\uparrow}\right)|\Omega\rangle\,,\\
|\mathbf{T}^-_\tau\rangle &= \hat{d}^\dagger_{S\downarrow}\hat{d}^\dagger_{L\tau\downarrow}\,|\Omega\rangle\,.
\end{aligned} \tag{6.8}$$

The orbital degeneracy of the LUMOs, expressed by the index τ, is responsible for the two sets of singlets (total spin $S=0$) and triplets (total spin $S=1$). Considering exchange interaction in a second step, we find that only the J^{ex}_{SL} term in Eq. (2.60),

$$-\sum_{\tau\sigma} J^{\mathrm{ex}}_{SL}\left(\hat{n}_{S\sigma}\hat{n}_{L\tau\sigma} - \hat{d}^\dagger_{S\sigma}\hat{d}^\dagger_{L\tau\bar{\sigma}}\hat{d}_{S\bar{\sigma}}\hat{d}_{L\tau\sigma}\right), \tag{6.9}$$

directly determines the low-energy structure of the anionic low-energy part because of the singly occupied SOMO and LUMOs: The degeneracy between singlets and triplets is lifted, see Fig. 6.1, and we obtain

$$\begin{aligned}
E_{\mathbf{S}} &= E^{\mathrm{g}}_{N_0} + J^{\mathrm{ex}}_{SL},\\
E_{\mathbf{T}} &= E^{\mathrm{g}}_{N_0} - J^{\mathrm{ex}}_{SL},
\end{aligned} \tag{6.10}$$

for the singlets and triplets, respectively.

Finally, to analyze in a third step how $\hat{V}_{\mathrm{SO}}$ affects the low-energy part of the anionic part of the spectrum, in particular which degeneracies are lifted, we treat it as a perturbation and apply second order perturbation theory to obtain the energy shifts. To this end, some additional states have to be considerd. They are listed in App. A.4.

The states $\mathbf{T}^+_-$ and $\mathbf{T}^-_+$ experience a downshift due to $\hat{V}_{\mathrm{SO}}$ and become the ground states. Measuring energies with respect to $E_{\mathbf{T}}$, we get

$$\Delta E_{\mathbf{T}^-_+} = \Delta E_{\mathbf{T}^+_-} = -\lambda_1 - \frac{2\lambda_2^2}{\Delta_1 + J^{\mathrm{ex}}_{SL}}, \tag{6.11}$$

see Fig. 6.1. Note that in our numerical calculations $\mathbf{T}^-_+$ and $\mathbf{T}^+_-$ are mixed and the degeneracy of the resulting states is lifted by a small shift in the range of some μeV. A more detailed discussion concerning

the mixing of $\mathbf{T}^-_+$ and $\mathbf{T}^+_-$ can be found in App. A.4. The next states are $\mathbf{T}^0_+$ and $\mathbf{T}^0_+$ with

$$\Delta E_{\mathbf{T}^0_+} = \Delta E_{\mathbf{T}^0_-} = -\frac{\lambda_1^2}{2J^{\mathrm{ex}}_{SL}} - \frac{\lambda_2^2}{\Delta_1 - J^{\mathrm{ex}}_{SL}}. \tag{6.12}$$

Due to their quadratic dependence on λ_1 and λ_2, these states change very little with $\hat{V}_{\mathrm{SO}}$. The degeneracy of the states $\mathbf{T}^+_+$ and $\mathbf{T}^-_-$ is lifted by the mixing of these states through $\hat{V}_{\mathrm{SO}}$. We find

$$|\alpha\rangle = \frac{1}{\sqrt{2}}\Big(|T^+_+\rangle + |T^-_-\rangle \Big), \tag{6.13}$$

$$|\beta\rangle = \frac{1}{\sqrt{2}}\Big(|T^+_+\rangle - |T^-_-\rangle \Big), \tag{6.14}$$

where for $|\beta\rangle$ we omitted smaller additional contributions from other states. The energies change according to

$$\Delta E(\alpha) = \lambda_1, \tag{6.15}$$

$$\Delta E(\beta) = \lambda_1 - 4\lambda_2^2 \left(\frac{1}{\Delta_1 + J^{\mathrm{ex}}_{SL}} + \frac{1}{\Delta_2 + J^{\mathrm{ex}}_{SL}} \right). \tag{6.16}$$

For further details we refer to App. A.4. Finally, the singlets $\mathbf{S}_+$ and $\mathbf{S}_-$, similar to $\mathbf{T}^0_+$ and $\mathbf{T}^0_-$, change very little (with respect to $E_{\mathbf{S}}$):

$$\Delta E_{\mathbf{S}_\tau} = \frac{\lambda_1^2}{2J^{\mathrm{ex}}_{SL}} - \frac{\lambda_2^2}{\Delta_1 - J^{\mathrm{ex}}_{SL}}. \tag{6.17}$$

By introducing $\hat{\tau} := \hat{n}_{L+} - \hat{n}_{L-}$, an approximate Hamiltonian up to first order in $\hat{V}_{\mathrm{SO}}$ can be given for the $N_0 + 1$ particle subblock:

$$\mathrm{H}_0^{N_0+1} = E^{\mathrm{g}}_{N_0+1} - J^{\mathrm{ex}}_{SL}\left(\hat{S}^2 - 1\right) + \lambda_1 \hat{\tau}\hat{S}_z. \tag{6.18}$$

Equation (6.18) is quite remarkable. It shows that, similar to the well studied molecular magnets [MPD+10, CCS+13, MBG+15, BGvdZ15], the interplay of spin-orbit coupling and exchange interactions yield magnetic anisotropies which can be captured by effective spin Hamiltonians. Noticeably, because Eq. (6.18) was derived from the microscopic molecular Hamiltonian $\hat{H}_{\mathrm{mol}}$, it was possible to check that deviations are in the μeV range and only of quantitative nature by comparison of the spectrum to the numerically evaluated one.

6.1.2 *Interaction with magnetic fields*

An experimentally accessible way to probe magnetic anisotropies is to apply external magnetic fields. In order to account for interactions of orbitals with magnetic fields, the atomic hopping matrix elements $b_{\alpha\beta}$ in Eq. (2.21) have to be corrected with Peierls phase factors,

$$b_{\alpha\beta} \to b_{\alpha\beta}\, \mathrm{e}^{i\phi_{\alpha\beta}}, \tag{6.19}$$

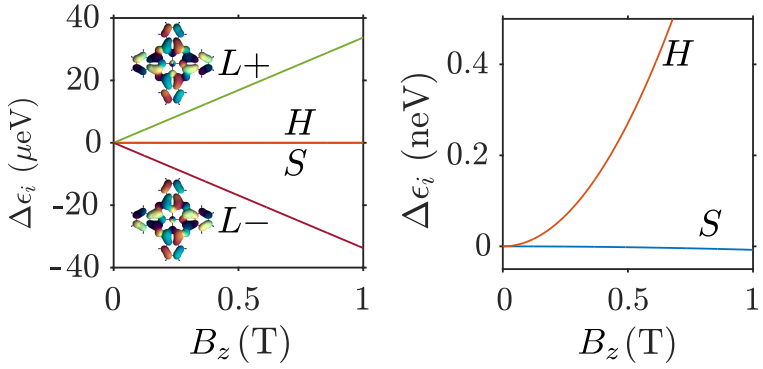

Figure 6.2: (a) Dependence of the single particle orbital energies on the magnetic field strength. From this, the effective orbital moment of the LUMOs, here depicted in their complex representation, can be extracted as $\mu_{\mathrm{orb}} = 33.7\ \mu\mathrm{eVT}^{-1}$. The energies of the SOMO and HOMO orbitals depend quadratically on the magnetic field and involve a much lower scale than the LUMOs, as seen in the close-up in panel (b).

where, using the gauge $\mathbf{A} = -B_z\, y\hat{x}$, the phase is given by

$$\phi_{\alpha\beta} = \frac{eB_z}{2\hbar}\,(y_\alpha + y_\beta)\,(x_\alpha - x_\beta)\,. \tag{6.20}$$

Here (x_α, y_α) are the in-plane atomic coordinates. Owing to the planar geometry of CuPc, $\phi_{\alpha\beta}$ depends only on the z-component B_z of the magnetic field $\mathbf{B}$. In Fig. 6.2 we show the dependence of the energies of the frontier molecular orbitals on the strength of the magnetic field in z-direction, B_z. For the two LUMOs we observe a linear dependence on the magnetic field, yielding an effective orbital moment of $\mu_{\mathrm{orb}} = 33.7\ \mu\mathrm{eVT}^{-1}$. Hereby the LUMO$-$(+) goes down (up) in energy with B_z, see Fig. 6.2 (a). The energies of the HOMO and the SOMO however scale quadratically with the magnetic field at a much lower scale, cf. Fig. 6.2 (b). This behaviour is expected, since the a_{1u} and b_{1g} representations have characters $+1$ under C_2' rotations, which transform B_z to $-B_z$. Thus the energies of HOMO and SOMO can not depend on the sign of B_z and must move at least quadratically with B_z. The two-dimensional e_g representation on the other hand has zero character under C_2' rotations, which implies that the constituents of e_g transform under such rotations either with different signs or into each other; indeed under a C_2' rotation LUMO+ is mapped onto LUMO$-$ and vice versa.

Finally, the interaction of electronic spins with magnetic fields is represented by adding a Zeeman term $\hat{V}_{\mathrm{Z}}$ to Eq. (6.1),

$$\hat{H}_{\mathrm{mol}} \to \hat{H}_{\mathrm{mol}} + \hat{V}_{\mathrm{Z}} = \hat{H}_{\mathrm{mol}} + g_S \mu_{\mathrm{B}}\, \hat{\mathbf{S}} \cdot \mathbf{B}, \tag{6.21}$$

where $g_S = 2$ and $\mathbf{S}$ is the total spin operator on the molecule written in the frontier orbital basis.

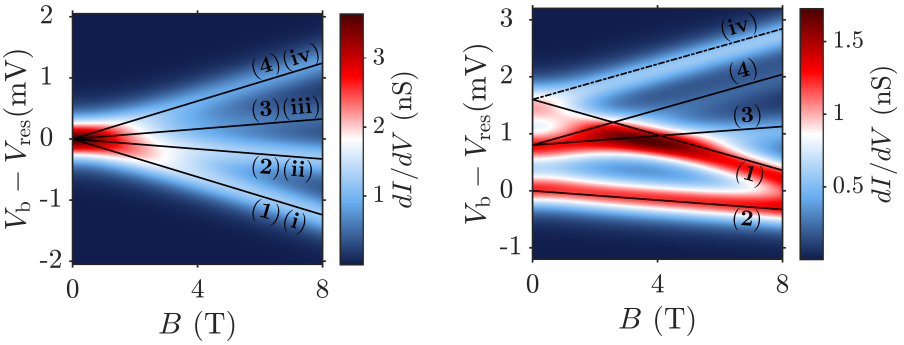

Figure 6.3: Differential conductance maps as a function of the strength B_z of the magnetic field in z-direction. Left (right) panel: Spin-orbit interaction switched off (on). Solid and dashed lines depict the addition spectrum as calculated from the effective spin Hamiltonian, cf. Eq. (6.22). Transitions starting from the neutral ground state are denoted by solid lines, those from the neutral excited state by dashed lines.

6.1.2.1 *Effective low-energy Hamiltonian*

Putting everything together, an effective low-energy Hamiltonian including magnetic interaction terms for both orbital and spin degrees of freedom can thus be given. It reads

$$\mathrm{H}_{\mathrm{eff}}^{N} = \mathrm{H}_{0}^{N} + \mu_{\mathrm{orb}}\,\hat{\tau} B_z + g_S \mu_{\mathrm{B}}\,\hat{\mathbf{S}} \cdot \mathbf{B}, \tag{6.22}$$

where H_{0}^{N} is the Hamiltonian for the corresponding low-energy N-particle subblock as given by Eqs. (6.6) and (6.18).

6.2 MAGNETOTRANSPORT AND MAGNETIC ANISOTROPY

In Fig. 6.3 we show the splitting of the anionic resonance with applied magnetic field in a dI/dV map. In the left panel SOI is switched off, whereas in the right panel it is switched on. One striking difference at first glance is the zero-field splitting for nonvanishing SOI, which is proportional to λ_1 but enhanced by the bias drop, cf. Eq. (3.76). For vanishing SOI, when S_z is a good quantum number, we can readily identify the corresponding transitions by using the effective spin Hamiltonian introduced in Eq. (6.22). In the following, transitions from the neutral ground state will be denoted by arabic numbers:

$$\begin{aligned}
(1): &\quad |N_0, \downarrow\rangle \to |\mathbf{T}_{-}^{-}\rangle \\
(2): &\quad |N_0, \downarrow\rangle \to |\mathbf{T}_{+}^{-}\rangle \\
(3): &\quad |N_0, \downarrow\rangle \to |\mathbf{T}_{-}^{0}\rangle \\
(4): &\quad |N_0, \downarrow\rangle \to |\mathbf{T}_{+}^{0}\rangle\,,
\end{aligned}$$

while transitions from the neutral excited state will be denoted by roman numerals:

$$(i): \quad |N_0, \uparrow\rangle \to |\mathbf{T}_{-}^{0}\rangle$$

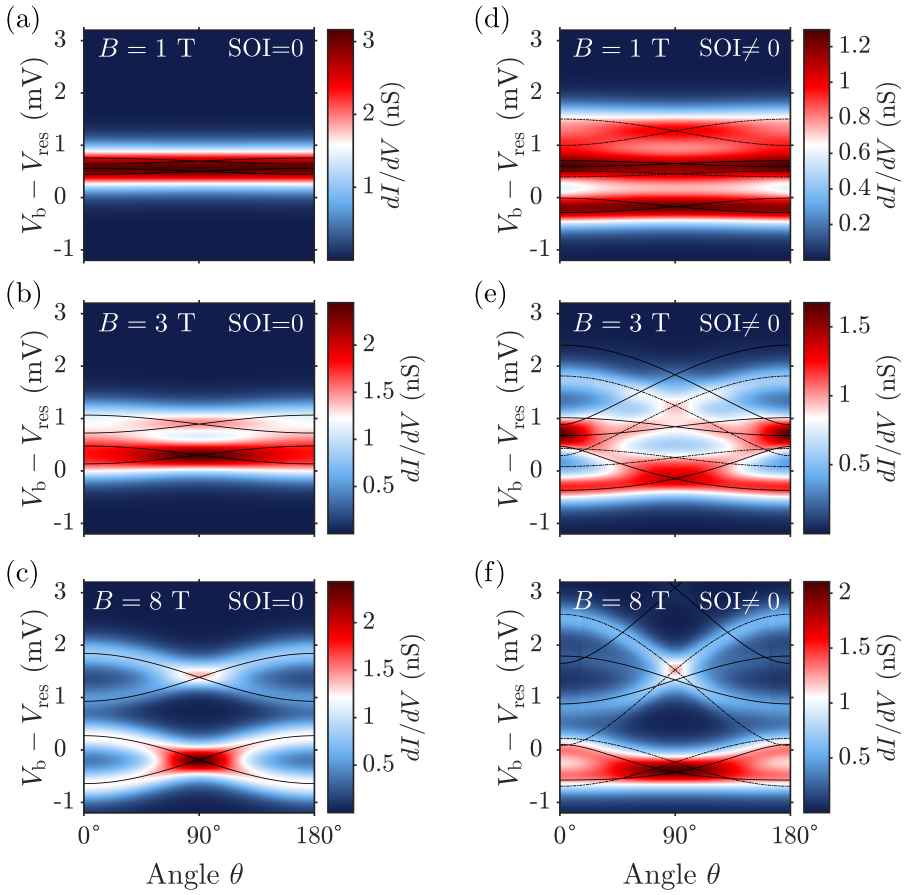

Figure 6.4: Differential conductance maps vs. the angle θ, formed by the applied magnetic field with the z-axis. Left (right) panels are without (with) SOI. Upper, middle and lower panels are calculated for a magnetic field strength of 1 T, 3 T and 8 T, respectively. Solid and dashed lines depict the addition spectrum as calculated from the effective spin Hamiltonian, cf. Eq. (6.22). Transitions starting from the neutral ground state are denoted by solid lines, those from the neutral excited state by dashed lines.

$$
\begin{aligned}
(ii): &\quad |N_0,\uparrow\rangle \rightarrow |\mathbf{T}^0_+\rangle \\
(iii): &\quad |N_0,\uparrow\rangle \rightarrow |\mathbf{T}^+_-\rangle \\
(iv): &\quad |N_0,\uparrow\rangle \rightarrow |\mathbf{T}^+_+\rangle\,.
\end{aligned}
$$

Other transitions are forbidden due to the selection rule for S_z, $\Delta S_z = \pm\frac{1}{2}$. The reason for the splitting into four lines observed in Fig. 6.3 top is that the orbital moment of the LUMO is not of the same size as the Bohr magneton.

For nonvanishing SOI, see lower panel of Fig. 6.3, the definite assignment of transitions is not straightforward, at least for small magnetic fields. Since $\mathbf{T}^-_+$ and $\mathbf{T}^+_-$ are shifted downward by SOI, transition (2) now is the lowest lying transition, whereas transition (1) is shifted upward due to the positive contribution $+\lambda_1$ to $\mathbf{T}^-_-$. Furthermore, transition (iv) is the only excited state transition which can be definitely assigned to a line in the lower panel in Fig. 6.3.

Figure 6.4 finally shows dI/dV maps as a function of the angle θ between the magnetic field and the z-axis. Hereby panels (a), (b) and (c) show results obtained with vanishing SOI and panels (d), (e) and (f) are for finite SOI. Again, the results were fitted using the effective spin Hamiltonian introduced in Eq. (6.22) with good agreement. The respective transitions can be identified by checking the assigned transitions in Fig. 6.3 at the corresponding field strength.

Already at $|\mathbf{B}| = B = 1$ T, cf. (a) and (d), the influence of SOI can be clearly seen. While for vanishing SOI any anisotropy of the dI/dV map is hidden beneath the temperature broadening, for finite SOI a slight θ-dependence can be observed. For $B = 3$ T, now also in the vanishing SOI case, Fig. 6.4 (b), a slight anisotropy due to the orbital moment of the LUMOs can be observed, although still blurred by temperature. Again, at finite SOI in Fig. 6.4 (e) there is a much more pronounced dependence on θ. The high conductance areas at $\theta = 0°$ and $\theta = 180°$ for $V_\mathrm{b} - V_\mathrm{res} \approx 0.8$ meV correspond to the high conductance area in the middle of Fig. 6.3 bottom, where many transitions are taking place at the same time. At $B = 8$ T, the magnetic field is dominating and a characteristic double cosine-like behaviour of the resonances can be observed, for both the case with no SOI, Fig. 6.4 (c), and finite SOI, Fig. 6.4 (f). For vanishing SOI, this behaviour is caused by the orbital moment of the LUMOs, since they interchange their positions when going from B_z to $-B_z$. The overall splitting between the double cosines, most evident at $\theta = 90°$, is caused by the Zeeman term. The results for $B = 8$ T in Fig. 6.4 (f) at finite SOI are similar to those in Fig. 6.4 (c), with the only difference that the cosine at large biases is more stretched, the one at low bias more compressed.

7

CONCLUSIONS

In this chapter we summarize the main results presented in the thesis and finally provide some remarks that could stimulate a future continuation of the present work.

7.1 SUMMARY

By studying the transport characteristics of an STM single molecule junction on a thin insulating film we established a criterion to identify the interference blocking scenario based on topographical fingerprints. In particular, for biases in the vicinity of the interference blocking regime, a flattening of the molecular image in constant height and an enhanced sensitivity of the apparent height to the working current in the constant current mode are expected. The robustness of the effect is on the one hand ensured by the observation that quasi-degeneracy and not exact degeneracy of the interfering many-body states is the necessary condition for the persistence of the phenomenon. On the other hand, altough intra-molecular relaxation processes can affect the robustness of interference NDC, we found that the effect could only be completely spoiled through a dephasing which is larger than the mean tip tunneling rate. Finally, the results presented so far for CuPc apply in general to the class of planar molecules belonging to the C_{nv} symmetry group. Their many body-states, like the single particle ones, can be classified using the projection ℓ of the angular momentum in the direction of their principal axis (conventionally the z axis). The generic many body eigenstates of $\hat{H}_{\mathrm{mol}}$ can thus be written in the form $|\mathrm{N}\, E\, \ell\, S_z\rangle$, where N is the particle number, E the energy, S_z and ℓ respectively the projections of the total spin and of the angular momentum in the z direction in units of $\hbar$. The state $|\mathrm{N}\, E\, \ell\, S_z\rangle$ transforms under a rotation of an angle $\phi = z2\pi/n$ around the main rotation axis as: $R_\phi|\mathrm{N}\, E\, \ell\, S_z\rangle = \mathrm{e}^{\mathrm{i}\phi(\ell+S_z)}|\mathrm{N}\, E\, \ell\, S_z\rangle$, where R_ϕ is the rotation operator. Consequently it is not difficult to prove that ℓ is an integer number and $-\frac{n}{2} < \ell \leq \frac{n}{2}$ for C_{nv} molecules with even n and $-\frac{n-1}{2} \leq \ell \leq \frac{n-1}{2}$ when n is odd. Since C_{nv} admits at maximum bidimensional irreducible representations, we conclude that the states with opposite ℓ have symmetry protected degeneracy and only states with $\ell = 0$ (for even or odd n) or $\ell = 0, \frac{n}{2}$ (for even n) are non degenerate.

For an experimentally accessible substrate work function of $\phi_0 = 5$ eV, we predicted the appearance, in proximity to the anionic resonance, of a population inversion between the neutral ground and excited states of CuPc. Depending on the tip position, the molecule is

triggered into a LS ($S = 1/2$) to HS ($S = 3/2$) transition which is mediated by this population inversion. This inversion is experimentally observable via dramatic changes in the topographical properties of constant height and constant current STM images, compared to a standard LUMO-mediated anionic transition. Direct observation of the spin-crossover might be accessible using spin-polarized scanning probe microscopy techniques. [PG13] The effect is also robust against moderate charge conserving relaxation processes. The quantitative accuracy of the spectroscopic and topographical results presented in this work is limited by the adopted semiempirical model. The spin-crossover with the associated anomalous topography of the anionic resonance depends on qualitative properties of the many-body spectrum and of the molecular orbitals. Thus, despite our focus on CuPc, they should be observable also in other molecules with comparable frontier orbital structure. To this end we provided criteria based on general molecular properties to help identify possible other candidates that could exhibit such anomalous transport properties.

Accounting for electron-electron, spin-orbit and magnetic interactions, we established a many-body Hamiltonian for CuPc. For the low-energy parts of the neutral and anionic blocks of the many-body spectrum we could further derive an effective spin Hamiltonian, capturing both SOI induced splittings and magnetic anisotropy. In order to study fingerprints of the SOI under realistic experimental conditions, we have studied the magnetotransport characteristics of a CuPc based junction in an STM setup. Noticeably, by using the effective spin Hamiltonian, it was possible to reconstruct the nature of the many-body resonances observed in the numerical calculations.

7.2 SOME OPEN QUESTIONS

Througout this work questions arose about problems or possible improvements of the transport formalism. We list them here as stimuli for possible continuations and improvements of the present work.

Electrostatic interactions of the molecule with its surroundings not only affect the charged states of the molecule, but in principle also other quantities like hopping or Coulomb integrals. To this end one has to use Poisson-equation based approaches. Is an analytical approach in the spirit of Ref. [KF11] possible for STM setups with thin insulating films, or at least numerically feasible?

If we compare our computed differential conductance spectra to experimental results, we immediately observe that in contrast to our theory, in the experiment there is substantial broadening on the order of 100 meV or more. Is it possible to set up an effective theory capturing the cause for the broadening or has one to microscopically incorparate vibronic degrees of freedom into the model? Or would adding a vibronic bath be a better solution?

More and more STM experiments report about bistabilites [SSR11, SID+15]. What is eventually the cause for those bistabilities and can they be incorporated in our transport formalism?

The occupied, bonding e_g partner orbitals to the LUMOs in CuPc have a rather large weight on the central copper atom (see Fig. 2.1). This in turn could affect the spin orbit interaction in this system, since these weights would yield a larger effective SOI constant. Would it be feasible to incorporate them in the many-body description of CuPc?

A

APPENDIX

A.1 REWRITING THE SINGLE PARTICLE PART

In order to render the single particle part in Eq. (2.7) in a more appropriate form, the sum over α and β is split into a diagonal and an offdiagonal part,

$$\hat{H}^{(1)}_{\text{mol}} = \sum_{\alpha mn} \langle \alpha m| \left(\frac{\hat{\mathbf{p}}^2}{2} + \sum_{\gamma} \hat{V}_{\gamma} \right) |\alpha n\rangle \; \hat{d}^{\dagger}_{\alpha m} \hat{d}_{\alpha n} + \sum_{\substack{\alpha\beta \\ mn}}^{\alpha\neq\beta} \langle \alpha m| \left(\frac{\hat{\mathbf{p}}^2}{2} + \sum_{\gamma} \hat{V}_{\gamma} \right) |\beta n\rangle \; \hat{d}^{\dagger}_{\alpha m} \hat{d}_{\beta n}. \tag{A.1}$$

In the diagonal part the sum over γ is split into two parts with $\gamma = \alpha$ and $\gamma \neq \alpha$, respectively:

$$\sum_{\alpha mn} \langle \alpha m| \left(\frac{\hat{\mathbf{p}}^2}{2} + \sum_{\gamma} \hat{V}_{\gamma} \right) |\alpha n\rangle \; \hat{d}^{\dagger}_{\alpha m} \hat{d}_{\alpha n} \tag{A.2}$$

$$= \sum_{\alpha mn} \left[\epsilon_{\alpha m} \delta_{mn} + \sum_{\gamma\neq\alpha} \langle \alpha m| \hat{V}_{\gamma} |\alpha n\rangle \right] \hat{d}^{\dagger}_{\alpha m} \hat{d}_{\alpha n}. \tag{A.3}$$

Here $\epsilon_{\alpha m}$ is the onsite energy of an electron in the orbital $|\alpha m\rangle$. Consequently, in the offdiagonal part the sum over γ is split accordingly:

$$\sum_{\substack{\alpha\beta \\ mn}}^{\alpha\neq\beta} \langle \alpha m| \left(\frac{\hat{\mathbf{p}}^2}{2} + \sum_{\gamma} \hat{V}_{\gamma} \right) |\beta n\rangle \; \hat{d}^{\dagger}_{\alpha m} \hat{d}_{\beta n} \tag{A.4}$$

$$= \sum_{\substack{\alpha\beta \\ mn}}^{\alpha\neq\beta} \left[b_{\alpha m,\beta n} + \sum_{\gamma}^{\gamma\neq\alpha,\beta} \langle \alpha m| \hat{V}_{\gamma} |\beta n\rangle \right] \hat{d}^{\dagger}_{\alpha m} \hat{d}_{\beta n}, \tag{A.5}$$

with $b_{\alpha m,\beta n}$ being the hopping matrix element between states $|\alpha m\rangle$ and $|\beta n\rangle$ and has only offdiagonal elements, $b_{\alpha m,\alpha n} = 0$. All non-hopping terms can be condensed in

$$V^{\text{ion}}_{\alpha m,\beta n} = \sum_{\gamma}^{\gamma\neq\alpha,\beta} \langle \alpha m| \hat{V}_{\gamma} |\beta n\rangle \,, \tag{A.6}$$

which is the crystal field correction to the single particle Hamiltonian.

A.2 SETTING UP THE MANY PARTICLE HAMILTONIAN

A.2.1 *The different terms of the Coulomb interaction*

The Coulomb interaction

$$\frac{1}{2}\sum_{ijkl}\sum_{\sigma\sigma'} V_{ijkl}\,\hat{d}^\dagger_{i\sigma}\hat{d}^\dagger_{k\sigma'}\hat{d}_{l\sigma'}\hat{d}_{j\sigma} \tag{A.7}$$

can be split into different terms corresponding to the number of different indices in the sum. The first term, where all four indices are the same is:

$$\sum_i V_{iiii}\,n_{i\uparrow}n_{i\downarrow}. \tag{A.8}$$

Terms with two different indices are:

$$\begin{aligned}
&\frac{1}{2}\sum_{[ij]} V_{iijj}\,\hat{n}_i\hat{n}_j + \sum_{[ij]\sigma}\left(V_{iiij}\,\hat{n}_{i\sigma}\,\hat{d}^\dagger_{i\bar{\sigma}}\hat{d}_{j\bar{\sigma}} + \text{h.c.}\right)\\
-&\frac{1}{2}\sum_{[ij]\sigma} V_{ijji}\left(\hat{n}_{i\sigma}\hat{n}_{j\sigma} - \hat{d}^\dagger_{i\sigma}\hat{d}^\dagger_{j\bar{\sigma}}\hat{d}_{i\bar{\sigma}}\hat{d}_{j\sigma}\right)\\
+&\frac{1}{2}\sum_{[ij]\sigma} V_{ijij}\,\hat{d}^\dagger_{i\sigma}\hat{d}^\dagger_{i\bar{\sigma}}\hat{d}_{j\bar{\sigma}}\hat{d}_{j\sigma},
\end{aligned} \tag{A.9}$$

where we used that $V_{ijkl} = V_{klij} = V^*_{jilk} = V^*_{lkji}$. The symbol $[\ldots]$ under the sum means for example for $[ijk]$: $i \neq j, i \neq k, j \neq k$. Terms with three different indices are:

$$\begin{aligned}
&\frac{1}{2}\sum_{[ijk]}\sum_{\sigma}\left(V_{ijik}\,\hat{d}^\dagger_{i\sigma}\hat{d}^\dagger_{i\bar{\sigma}}\hat{d}_{k\bar{\sigma}}\hat{d}_{j\sigma} + \text{h.c.}\right)\\
&+\sum_{[ijk]}\sum_{\sigma} V_{ijki}\left(\hat{d}^\dagger_{i\sigma}\hat{d}^\dagger_{k\bar{\sigma}}\hat{d}_{i\bar{\sigma}}\hat{d}_{j\sigma} - \hat{n}_{i\sigma}\,\hat{d}^\dagger_{k\sigma}\hat{d}_{j\sigma}\right)\\
&+\sum_{[ijk]}\sum_{\sigma} V_{iijk}\,\hat{n}_i\,\hat{d}^\dagger_{j\sigma}\hat{d}_{k\sigma}.
\end{aligned} \tag{A.10}$$

Consequently the last term with four different indices reads

$$\frac{1}{2}\sum_{[ijkl]}\sum_{\sigma\sigma'} V_{ijkl}\,\hat{d}^\dagger_{i\sigma}\hat{d}^\dagger_{k\sigma'}\hat{d}_{l\sigma'}\hat{d}_{j\sigma}. \tag{A.11}$$

A.2.2 *Monte Carlo integration*

The intermediate value theorem for integrals states that, for a function f which is continous on the interval $[x_1, x_2]$, there exists a number x_m such that

$$\int_{x_1}^{x_2} \mathrm{d}x\, f(x) = (b-a)\, f(x_m). \tag{A.12}$$

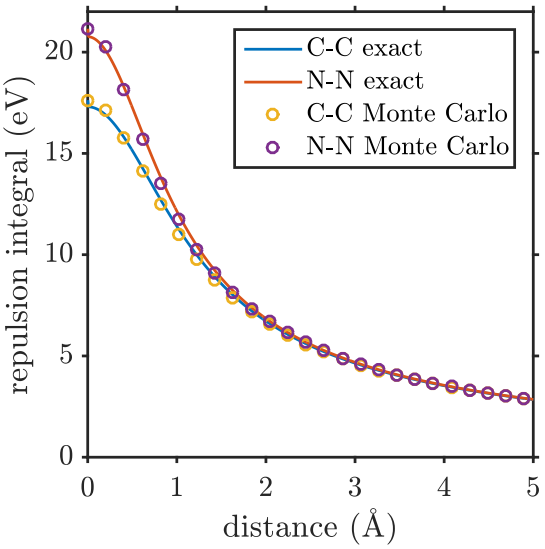

Figure A.1: Benchmark of numerical integration algorithm for a repulsion integral between two p_z-type Slater orbitals, varying with distance against the exact result given by Ref. [Roo51].

Basically, Monte Carlo integration makes use of this theorem by evaluating f at N uniformly distributed random numbers q_i in the interval $[x_1, x_2]$ and averaging over them:

$$\int_{x_1}^{x_2} \mathrm{d}x\, f(x) = (b-a)\, f(x_m) \approx (b-a)\, \frac{1}{N} \sum_{i=1}^{N} f(q_i). \tag{A.13}$$

The larger N, the better is the estimate for the integral. This approach can also be extended to multidimensional integrals over a multidimensional volume V:

$$\int_V \mathrm{d}r^d\, f(\underline{r}) \approx V \frac{1}{N} \sum_{i=1}^{N} f(\underline{q}_i), \tag{A.14}$$

which makes it our tool of choice to evaluate the integrals of the Coulomb interaction. In this work, we use the implementation of the VEGAS Monte Carlo algorithm in GSL [Gal13].

In Fig. A.1 we compare the results of the integration algorithm for a repulsion integral between two p_z-type Slater orbitals with varying distance d and effective charges corresponding to carbon and nitrogen atoms,

$$I(d) = \int \mathrm{d}^3 r_1 \int \mathrm{d}^3 r_2\, |\phi(\mathbf{r}_1 - \frac{\mathbf{d}}{2})|^2\, V(r_{12})\, |\phi(\mathbf{r}_1 + \frac{\mathbf{d}}{2})|^2, \tag{A.15}$$

with the exact result given by Roothaan [Roo51]. As can be seen, there is quite good agreement.

A.2.3 *Detailed list of fit parameters*

Using our model Hamiltonian we could fit the absolute spectroscopic position of the anionic and cationic transition and obtain, in accordance with the experiments, standard topographical images for CuPc on Cu(100) and trilayer NaCl [SSR11], as well as CuPc on Cu(111) and bilayer NaCl [USR13] within essentially the same set of fitting parameters ϵ_{mol} and Δ for the isolated molecule, see Table A.1.

			NaCl(3ML) Cu[100]	NaCl(2ML) Cu[111]
i)	ϕ_0	(eV)	4.65	5.00
	d	(Å)	8.1	6.0
ii)	Δ	(eV)	1.83	1.74
iii)	δ_{ic}	(eV)	0.32	0.44
	α_{S}		0.16	0.12
	α_{T}		0.59	0.62
iv)	$V_{\text{an}}^{\text{exp}}$	(V)	0.81	0.95
	$V_{\text{an}}^{\text{th}}$	(V)	0.81	1.01
	$V_{\text{cat}}^{\text{exp}}$	(V)	−2.62	−2.15
	$V_{\text{cat}}^{\text{th}}$	(V)	−2.72	−2.00

Table A.1: The table contains: i) The substrate tabulated parameters: work function ϕ_0 and insulating layer thickness d ii). The fitting parameter: the crystal field energy shift Δ. The molecular relative permittivity is taken to be $\epsilon_{mol} = 2.2$ in both cases. iii) The relative potential drops $\alpha_{S/T}$ and the image charge renormalization δ_{ic} are calculated according to (3.34) and (3.36), assuming in both cases a tip molecule distance $h = 5$ Å and a molecular surface $A = 144$ Å^2. iv) Experimental and fitted values for the biases corresponding to the anionic and cationic resonances. The experimental values are extracted from [SSR11] for NaCl(3ML)/Cu[100] and from [USR13] for NaCl(2ML)/Cu[111].

A.3 FUNCTIONS AND INTEGRALS USED IN THE DERIVATION OF THE TUNNELING MATRIX ELEMENTS

The functions $I_\eta^n(\kappa, a)$, $n = 0, 1$ result from the overlap of $\psi_\perp^\eta(z)$ with an atomic Gaussian orbital and are given by:

$$I_{\text{T}}^n(\kappa, a) = \frac{n_\perp^{\text{T}}}{2} F^n(a, \kappa, z_{\text{T}} - d)\, \mathrm{e}^{\frac{\kappa^2}{4a}}, \tag{A.16}$$

$$I_{\text{S}}^n(\kappa, a) = \frac{n_\perp^{\text{S}}}{2} F^n(a, \kappa, d)\, \mathrm{e}^{\frac{\kappa^2}{4a}}. \tag{A.17}$$

The functions $F^n(a,\kappa,x)$ are defined as:

$$F^0(a,\kappa,x) = \sqrt{\frac{\pi}{a}}\,\mathrm{e}^{-\kappa x}\left(1-\mathrm{erf}\left(\sqrt{a}\left[\frac{\kappa}{2a}-x\right]\right)\right),$$
$$F^1(a,\kappa,x) = \frac{\kappa}{2a}\,F^0(a,\kappa,x) - \mathrm{e}^{-ax^2-\frac{\kappa^2}{4a}}, \tag{A.18}$$

where $\mathrm{erf}(x)$ is the error function.

In order to establish Eq. (3.26), first the product $\sin^p(\theta+\varphi)\cos^q(\theta+\varphi)$ is expanded using the binomial theorem:

$$\sin^p(\theta+\phi)\cos^q(\theta+\phi) =$$
$$\frac{i^p}{2^{p+q}}\sum_{k=0}^{p}\sum_{l=0}^{q}(-1)^k\binom{p}{k}\binom{q}{l}\mathrm{e}^{i(2[k+l]-[p+q])(\theta+\varphi)}. \tag{A.19}$$

Then, by using the relation

$$\mathrm{e}^{ix\cos\theta} = \sum_{t=-\infty}^{\infty} i^t J_t(x)\,\mathrm{e}^{it\theta}, \tag{A.20}$$

and noting that for an integer t the integral

$$\int_0^{2\pi}\mathrm{d}\theta\,\mathrm{e}^{it\theta} = 2\pi\,\delta_{t,0} \tag{A.21}$$

is either 2π or 0 depending if $t=0$ or $t\neq 0$, respectively, we immediately arrive at Eq. (3.26).

A.4 DETAILS ON THE PERTURBATIVE TREATMENT OF SOI

In addition to the states introduced in Eq. (6.8), the following states must be also taken into account when performing second order perturbation theory:

$$|L\tau\uparrow, L\tau\downarrow\rangle = \hat{d}^\dagger_{L\tau\uparrow}\hat{d}^\dagger_{L\tau\downarrow}|\Omega\rangle,$$
$$|L\tau\sigma, L\bar{\tau}\sigma'\rangle = \hat{d}^\dagger_{L\tau\sigma}\hat{d}^\dagger_{L\tau\sigma'}|\Omega\rangle,$$
$$|S\uparrow, S\downarrow\rangle = \hat{d}^\dagger_{S\uparrow}\hat{d}^\dagger_{S\downarrow}|\Omega\rangle, \tag{A.22}$$

with $E_{L\tau\uparrow,L\tau\downarrow} = E_{L\tau\sigma,L\bar{\tau}\sigma'} = \Delta_1$ and $E_{S\uparrow,S\downarrow} = \Delta_2$. In the basis introduced in Eqs. (6.8) and (A.22), $\hat{V}_{\mathrm{SO}}$ is block-diagonal and decomposes into six subblocks: two three-dimensional, two two-dimensional, one four-dimensional and one one-dimensional subblocks.

The four dimensional subblock describes the effects of SOI on the $\mathbf{T}^+_+$ and $\mathbf{T}^-_-$ states. Written in the basis $\{|\mathbf{T}^+_+\rangle, |\mathbf{T}^-_-\rangle, |L^+\uparrow, L^-\downarrow\rangle, |S\uparrow, S\downarrow\rangle\}$, the Hamiltonian reads

$$H = \begin{pmatrix} -J^{\mathrm{ex}}_{SL} & 0 & 0 & 0 \\ 0 & -J^{\mathrm{ex}}_{SL} & 0 & 0 \\ 0 & 0 & \Delta_1 & 0 \\ 0 & 0 & 0 & \Delta_2 \end{pmatrix}$$

$$+\begin{pmatrix} \lambda_1 & 0 & -\sqrt{2}\lambda_2 & \sqrt{2}\lambda_2 \\ 0 & \lambda_1 & \sqrt{2}\lambda_2 & -\sqrt{2}\lambda_2 \\ -\sqrt{2}\lambda_2 & \sqrt{2}\lambda_2 & \lambda_1 & 0 \\ \sqrt{2}\lambda_2 & -\sqrt{2}\lambda_2 & 0 & 0 \end{pmatrix}. \tag{A.23}$$

The degeneracy of the unperturbed states $\mathbf{T}_+^+$ and $\mathbf{T}_-^-$ and the fact that there are no matrix-elements which couple these states require the use of second order degenerate perturbation theory. Applying it yields the following matrix M:

$$M = A \times \begin{pmatrix} 1 & -1 \\ -1 & 1 \end{pmatrix}, \tag{A.24}$$

where the prefactor A is given by

$$A = -2\lambda_2^2 \left(\frac{1}{\Delta_1 + J_{SL}^{\mathrm{ex}}} + \frac{1}{\Delta_2 + J_{SL}^{\mathrm{ex}}} \right). \tag{A.25}$$

Diagonalization of M gives the second-order energy corrections

$$\Delta E(\alpha) = \lambda_1, \tag{A.26}$$

$$\Delta E(\beta) = \lambda_1 - 4\lambda_2^2 \left(\frac{1}{\Delta_1 + J_{SL}^{\mathrm{ex}}} + \frac{1}{\Delta_2 + J_{SL}^{\mathrm{ex}}} \right), \tag{A.27}$$

and the correct linear combinations of the states $\mathbf{T}_+^+$ and $\mathbf{T}_-^-$:

$$|\alpha\rangle = \frac{1}{\sqrt{2}} \Big(|\mathbf{T}_+^+\rangle + |\mathbf{T}_-^-\rangle \Big), \tag{A.28}$$

$$|\beta\rangle = \frac{1}{\sqrt{2}} \Big(|\mathbf{T}_+^+\rangle - |\mathbf{T}_-^-\rangle \Big). \tag{A.29}$$

Writing H in the basis $\{|\alpha\rangle, |\beta\rangle, |L^+\uparrow, L^-\downarrow\rangle, |S\uparrow, S\downarrow\rangle\}$ yields:

$$\tilde{H} = \begin{pmatrix} -J_{SL}^{\mathrm{ex}} & 0 & 0 & 0 \\ 0 & -J_{SL}^{\mathrm{ex}} & 0 & 0 \\ 0 & 0 & \Delta_1 & 0 \\ 0 & 0 & 0 & \Delta_2 \end{pmatrix} + \begin{pmatrix} \lambda_1 & 0 & 0 & 0 \\ 0 & \lambda_1 & -2\lambda_2 & 2\lambda_2 \\ 0 & -2\lambda_2 & \lambda_1 & 0 \\ 0 & 2\lambda_2 & 0 & 0 \end{pmatrix}. \tag{A.30}$$

We see that $|\alpha\rangle$ stays unaffected by the perturbation, whereas $|\beta\rangle$ will change:

$$|\beta\rangle \to |\beta\rangle + 2\,\frac{\lambda_2}{\Delta_1 + J_{SL}^{\mathrm{ex}}}\,|L^+\uparrow, L^-\downarrow\rangle$$

$$-2\,\frac{\lambda_2}{\Delta_2 + J_{SL}^{\mathrm{ex}}}\,|S\uparrow, S\downarrow\rangle\,. \tag{A.31}$$

The mixing of $\mathbf{T}_+^-$ and $\mathbf{T}_-^+$ is caused by a pair-hopping term in the Hamiltonian, more precisely by

$$\frac{1}{2}J_{L+L-}^{\mathrm{p}}\sum_{\sigma}\left(\hat{d}_{L+\sigma}^{\dagger}\hat{d}_{L+\bar{\sigma}}^{\dagger}\hat{d}_{L-\bar{\sigma}}\hat{d}_{L-\sigma} + \mathrm{h.c.}\right), \tag{A.32}$$

which couples $\mathbf{T}_+^-$ and $\mathbf{T}_-^+$ to the following states:

$$\begin{aligned}
|a\rangle &= \frac{1}{\sqrt{2}}\hat{d}_{H\uparrow}^{\dagger}\hat{d}_{H\downarrow}^{\dagger}\left(\hat{d}_{L+\uparrow}^{\dagger}\hat{d}_{L+\downarrow}^{\dagger} - \hat{d}_{L-\uparrow}^{\dagger}\hat{d}_{L-\downarrow}^{\dagger}\right)|0\rangle\,,\\
|b\rangle &= \frac{1}{\sqrt{2}}\hat{d}_{H\uparrow}^{\dagger}\hat{d}_{H\downarrow}^{\dagger}\left(\hat{d}_{L+\uparrow}^{\dagger}\hat{d}_{L+\downarrow}^{\dagger} + \hat{d}_{L-\uparrow}^{\dagger}\hat{d}_{L-\downarrow}^{\dagger}\right)|0\rangle\,,
\end{aligned} \tag{A.33}$$

with corresponding energies E_a and $E_b = E_a + 2J_{L+L-}^{\mathrm{p}}$. Then, after introducing

$$\begin{aligned}
|\mathbf{T}_1\rangle &= \frac{1}{\sqrt{2}}\left(|\mathbf{T}_+^-\rangle + |\mathbf{T}_-^+\rangle\right),\\
|\mathbf{T}_2\rangle &= \frac{1}{\sqrt{2}}\left(|\mathbf{T}_+^-\rangle - |\mathbf{T}_-^+\rangle\right),
\end{aligned} \tag{A.34}$$

the Hamiltonian in the basis of these four states can be written as

$$H = \begin{pmatrix} H_{1b} & 0\\ 0 & H_{2a}\end{pmatrix}, \tag{A.35}$$

with

$$H_{1b} = \begin{pmatrix} -J_{SL}^{\mathrm{ex}} - \lambda_1 & \lambda_2\\ \lambda_2 & E_b\end{pmatrix} \tag{A.36}$$

and

$$H_{2a} = \begin{pmatrix} -J_{SL}^{\mathrm{ex}} - \lambda_1 & \lambda_2\\ \lambda_2 & E_a\end{pmatrix}. \tag{A.37}$$

Diagonalization finally yields the four states

$$\begin{aligned}
|1\rangle &= \frac{1}{\sqrt{1-\gamma_b^2}}\left(|\mathbf{T}_1\rangle + \gamma_b\,|b\rangle\right),\\
|2\rangle &= \frac{1}{\sqrt{1-\gamma_a^2}}\left(|\mathbf{T}_2\rangle + \gamma_a\,|a\rangle\right),\\
|\tilde{1}\rangle &= \frac{1}{\sqrt{1-\gamma_b^2}}\left(|b\rangle - \gamma_b\,|\mathbf{T}_1\rangle\right),\\
|\tilde{2}\rangle &= \frac{1}{\sqrt{1-\gamma_a^2}}\left(|a\rangle - \gamma_a\,|\mathbf{T}_2\rangle\right),
\end{aligned} \tag{A.38}$$

with the admixture $\gamma_{a/b} \approx \frac{-\lambda_2}{E_{a/b}+J_{SL}^{\mathrm{ex}}}$. Their energies are approximately

$$
\begin{aligned}
E_1 &\approx -\lambda_1 - \frac{\lambda_2^2}{E_b + J_{SL}^{\mathrm{ex}} + \lambda_1}, \\
E_2 &\approx -\lambda_1 - \frac{\lambda_2^2}{E_a + J_{SL}^{\mathrm{ex}} + \lambda_1}, \\
E_{\tilde{1}} &\approx E_b + \frac{\lambda_2^2}{E_b + J_{SL}^{\mathrm{ex}} + \lambda_1}, \\
E_{\tilde{2}} &\approx E_a + \frac{\lambda_2^2}{E_a + J_{SL}^{\mathrm{ex}} + \lambda_1}.
\end{aligned} \tag{A.39}
$$

This analysis reproduces mixing and energy splittings consistent with our numerical calculations.

BIBLIOGRAPHY

[AJP88] A. Aviram, C. Joachim, and M. Pomerantz. Evidence of switching and rectification by a single molecule effected with a scanning tunneling microscope. Chem. Phys. Lett. **146**, 490, 1988. (Cited on page 1.)

[AJP89] A. Aviram, C. Joachim, and M. Pomerantz. Evidence of switching and rectification by a single molecule effected by a scanning tunneling microscope: Chem. phys. letters 146 (1988) 490. Chem. Phys. Lett. **162**, 416, 1989. (Cited on page 1.)

[AMK+12] S. V. Aradhya, J. S. Meisner, M. Krikorian, S. Ahn, R. Parameswaran, M. L. Steigerwald, C. Nuckolls, and L. Venkataraman. Dissecting Contact Mechanics from Quantum Interference in Single-Molecule Junctions of Stilbene Derivatives. Nano Lett. **12**, 1643, 2012. (Cited on page 41.)

[AR74] A. Aviram and M. A. Ratner. Molecular rectifiers. Chem. Phys. Lett. **29**, 277, 1974. (Cited on page 1.)

[AV13] S. V. Aradhya and L. Venkataraman. Single-molecule junctions beyond electronic transport. Nat. Nano **8**, 399, 2013. (Cited on page 1.)

[Bar61] J. Bardeen. Tunnelling from a many-particle point of view. Phys. Rev. Lett. **6**, 57, 1961. (Cited on page 3.)

[BBS93] J. Bendix, M. Brorson, and C. E. Schaffer. Accurate empirical spin-orbit coupling parameters ζ_{nd} for gaseous ndq transition metal ions. The parametrical multiplet term model. Inorg. Chem. **32**, 2838, 1993. (Cited on page 64.)

[BCMG89] P. Bedrossian, D. M. Chen, K. Mortensen, and J. A. Golovchenko. Demonstration of the tunnel-diode effect on an atomic scale. Nature **342**, 258, 1989. (Cited on page 41.)

[BDDG08] G. Begemann, D. Darau, A. Donarini, and M. Grifoni. Symmetry fingerprints of a benzene single-electron transistor: Interplay between Coulomb interaction and orbital symmetry. Phys. Rev. B **77**, 201406, 2008. Erratum **78**, 089901(E) (2008). (Cited on pages 40 and 46.)

[BGvdZ15] E. Burzurí, R. Gaudenzi, and H. S. J. van der Zant. Observing magnetic anisotropy in electronic transport through individual single-molecule magnets. J. Phys.: Condens. Matter **27**, 113202, 2015. (Cited on pages 63 and 67.)

[BJ84] B. Bott and T. Jones. A highly sensitive no2 sensor based on electrical conductivity changes in phthalocyanine film. Sens. Actuators **5**, 43, 1984. (Cited on page 4.)

[BLD96] Z. Bao, A. J. Lovinger, and A. Dodabalapur. Organic field-effect transistors with high mobility based on copper phthalocyanine. Appl. Phys. Lett. **69**, 3066, 1996. (Cited on page 4.)

[Blu96] K. Blum. *Density Matrix Theory and Applications*. Plenum Press, 1996. (Cited on pages 31 and 32.)

[BMO+02] M. Brandbyge, J.-L. Mozos, P. Ordejón, J. Taylor, and K. Stokbro. Density-functional method for nonequilibrium electron transport. Phys. Rev. B **65**, 165401, 2002. (Cited on page 1.)

[BO27] M. Born and R. Oppenheimer. Zur Quantentheorie der Molekeln. Ann. Phys. **389**, 457, 1927. (Cited on page 8.)

[Bou14] S. Bouvron. *Gate-controlled scanning tunneling spectroscopy of CoPc molecules on graphene*. PhD thesis, Faculty of Physics, University of Konstanz, 2014. (Cited on page 52.)

[BRGW82] G. Binnig, H. Rohrer, C. Gerber, and E. Weibel. Surface studies by scanning tunneling microscopy. Phys. Rev. Lett. **49**, 57, 1982. (Cited on page 2.)

[CCL07] H. J. Choi, M. L. Cohen, and S. G. Louie. First-principles scattering-state approach for nonlinear electrical transport in nanostructures. Phys. Rev. B **76**, 155420, 2007. (Cited on page 1.)

[CCS+13] A. Chiesa, S. Carretta, P. Santini, G. Amoretti, and E. Pavarini. Many-Body Models for Molecular Nanomagnets. Phys. Rev. Lett. **110**, 157204, 2013. (Cited on pages 63 and 67.)

[CF67] I. D. Clark and D. C. Frost. A study of the energy levels in benzene and some fluorobenzenes by photoelectron spectroscopy. J. Am. Chem. Soc. **89**, 244, 1967. (Cited on page 9.)

[CFJ+82] F. Calderazzo, S. Frediani, B. R. James, G. Pampaloni, K. J. Reimer, J. R. Sams, A. M. Serra, and D. Vitali. Synthesis and Mössbauer Spectroscopic Studies of Carbonyl Derivatives of (Phthalocyaninato)iron(II). Inorg. Chem. **21**, 2302, 1982. (Cited on page 51.)

[CFN07] A. Calzolari, A. Ferretti, and M. B. Nardelli. Ab initio correlation effects on the electronic and transport properties of metal(ii)-phthalocyanine-based devices. Nanotechnology **18**, 424013, 2007. (Cited on page 12.)

[CHZ+07] L. Chen, Z. Hu, A. Zhao, B. Wang, Y. Luo, J. Yang, and J. G. Hou. Mechanism for Negative Differential Resistance in Molecular Electronic Devices: Local Orbital Symmetry Matching. Phys. Rev. Lett. **99**, 146803, 2007. (Cited on page 41.)

[CR63] E. Clementi and D. L. Raimondi. Atomic Screening Constants from SCF Functions. J. Chem. Phys. **38**, 2686, 1963. (Cited on page 21.)

[CRRT99] J. Chen, M. A. Reed, A. M. Rawlett, and J. M. Tour. Large On-Off Ratios and Negative Differential Resistance in a Molecular Electronic Device. Science **286**, 1550, 1999. (Cited on page 41.)

[CS31] L. Cambi and L. Szegö. Über die magnetische Susceptibilität der komplexen Verbindungen. Ber. Dtsch. Chem. Ges. **64**, 2591, 1931. (Cited on page 51.)

[CSM06] D. M. Cardamone, C. A. Stafford, and S. Mazumdar. Controlling Quantum Transport through a Single Molecule. Nano Lett. **6**, 2422, 2006. (Cited on page 41.)

[DBDG09] D. Darau, G. Begemann, A. Donarini, and M. Grifoni. Interference effects on the transport characteristics of a benzene single-electron transistor. Phys. Rev. B **79**, 235404, 2009. (Cited on pages 46, 49, and 57.)

[DBG09] A. Donarini, G. Begemann, and M. Grifoni. All-Electric Spin Control in Interference Single Electron Transistors. Nano Lett. **9**, 2897, 2009. (Cited on page 46.)

[DBG10] A. Donarini, G. Begemann, and M. Grifoni. Interference effects in the Coulomb blockade regime: Current blocking and spin preparation in symmetric nanojunctions. Phys. Rev. B **82**, 125451, 2010. (Cited on page 46.)

[dOESGL+10] D. G. de Oteyza, A. El-Sayed, J. M. Garcia-Lastra, E. Goiri, T. N. Krauss, A. Turak, E. Barrena, H. Dosch, J. Zegenhagen, A. Rubio, Y. Wakayama, and J. E. Ortega. Copper-phthalocyanine based metal-organic interfaces: The effect of fluorination, the substrate, and its symmetry. The Journal of Chemical Physics **133**, 214703, 2010. (Cited on page 12.)

[DSSG12] A. Donarini, B. Siegert, S. Sobczyk, and M. Grifoni. Topographical fingerprints of many-body interference in STM junctions on thin insulating films. Phys. Rev. B **86**, 155451, 2012. (Cited on pages 1, 24, and 40.)

[DTH+97] S. Datta, W. Tian, S. Hong, R. Reifenberger, J. I. Henderson, and C. P. Kubiak. Current-voltage characteristics of self-assembled monolayers by scanning tunneling microscopy. Phys. Rev. Lett. **79**, 2530, 1997. (Cited on page 23.)

[DVPL00] M. Di Ventra, S. T. Pantelides, and N. D. Lang. First-principles calculation of transport properties of a molecular device. Phys. Rev. Lett. **84**, 979, 2000. (Cited on page 1.)

[ECS+07] F. Evangelista, V. Carravetta, G. Stefani, B. Jansik, M. Alagia, S. Stranges, and A. Ruocco. Electronic structure of copper phthalocyanine: An experimental and theoretical study of occupied and unoccupied levels. J. Chem. Phys. **126**, 124709, 2007. (Cited on page 12.)

[Ern11] M. Ernzerhof. Simple orbital theory for the molecular electrician. J. Chem. Phys. **135**, 014104, 2011. (Cited on page 41.)

[FH79] S. Froyen and W. A. Harrison. Elementary prediction of linear combination of atomic orbitals matrix elements. Phys. Rev. B **20**, 2420, 1979. (Cited on pages 9 and 11.)

[FSH+08] K. J. Franke, G. Schulze, N. Henningsen, I. Fernández-Torrente, J. I. Pascual, S. Zarwell, K. Rück-Braun, M. Cobian, and N. Lorente. Reducing the Molecule-Substrate Coupling in C_{60}-Based Nanostructures by Molecular Interactions. Phys. Rev. Lett. **100**, 036807, 2008. (Cited on page 41.)

[FTKLSdz+12] I. Fernández-Torrente, D. Kreikemeyer-Lorenzo, A. Stróżecka, K. J. Franke, and J. I. Pascual. Gating the Charge State of Single Molecules by Local Electric

Fields. Phys. Rev. Lett. **108**, 036801, 2012. (Cited on page 52.)

[Gal13] M. Galassi. *GNU Scientific Library Reference Manual*, third edition, 2013. https://www.gnu.org/software/gsl/manual/. (Cited on pages 20 and 79.)

[GGG00] P. Gütlich, Y. Garcia, and H. A. Goodwin. Spin crossover phenomena in Fe(II) complexes. Chem. Soc. Rev. **29**, 419, 2000. (Cited on page 51.)

[GLH00] J. Gaudioso, L. J. Lauhon, and W. Ho. Vibrationally Mediated Negative Differential Resistance in a Single Molecule. Phys. Rev. Lett. **85**, 1918, 2000. (Cited on pages 2 and 41.)

[GMM+11] L. Gross, N. Moll, F. Mohn, A. Curioni, G. Meyer, F. Hanke, and M. Persson. High-resolution molecular orbital imaging using a *p*-wave stm tip. Phys. Rev. Lett. **107**, 086101, 2011. (Cited on page 2.)

[GMN+12] T. G. Gopakumar, F. Matino, H. Naggert, A. Bannwarth, F. Tuczek, and R. Berndt. Electron-induced spin crossover of single molecules in a bilayer on gold. Angew. Chem. Int. Ed. **51**, 6262, 2012. (Cited on pages 1, 2, and 51.)

[GO57] J. S. Griffith and L. E. Orgel. Ligand-field theory. Q. Rev. Chem. Soc. **11**, 381, 1957. (Cited on page 51.)

[GSV06] D. Gatteschi, R. Sessoli, and J. Villain. *Molecular Nanomagnets*. Oxford University Press, 2006. (Cited on page 63.)

[GVM+12] C. M. Guedon, H. Valkenier, T. Markussen, K. S. Thygesen, J. C. Hummelen, and S. J. van der Molen. Observation of quantum interference in molecular charge transport. Nat. Nano **7**, 305, 2012. (Cited on page 41.)

[GWYC05] M. Grobis, A. Wachowiak, R. Yamachika, and M. F. Crommie. Tuning negative differential resistance in a molecular film. Appl. Phys. Lett. **86**, 204102, 2005. (Cited on page 41.)

[HFS03] W. A. Hofer, A. S. Foster, and A. L. Shluger. Theories of scanning probe microscopes at the atomic scale. Rev. Mod. Phys. **75**, 1287, 2003. (Cited on page 2.)

[HRC+11] B. W. Heinrich, M. V. Rastei, D.-J. Choi, T. Frederiksen, and L. Limot. Engineering Negative Differential

Conductance with the Cu(111) Surface State. Phys. Rev. Lett. **107**, 246801, 2011. (Cited on page 41.)

[HSP69] W. J. Hehre, R. F. Stewart, and J. A. Pople. Self-Consistent Molecular-Orbital Methods. I. Use of Gaussian Expansions of Slater-Type Atomic Orbitals. J. Chem. Phys. **51**, 2657, 1969. (Cited on page 25.)

[Hue31] E. Hueckel. Quantentheoretische Beiträge zum Benzolproblem I: die Elektronenkonfiguration des Benzols und verwandter Verbindungen. Zeitschrift fur Physik **70**, 204, 1931. (Cited on page 9.)

[Jen99] F. Jensen. *Introduction to Computational Chemistry*. John Wiley & Sons, 1999. (Cited on page 8.)

[JGSC95] C. Joachim, J. K. Gimzewski, R. R. Schlittler, and C. Chavy. Electronic transparence of a single c_{60} molecule. Phys. Rev. Lett. **74**, 2102, 1995. (Cited on page 1.)

[KF11] K. Kaasbjerg and K. Flensberg. Image charge effects in single-molecule junctions: Breaking of symmetries and negative-differential resistance in a benzene single-electron transistor. Phys. Rev. B **84**, 115457, 2011. (Cited on pages 24, 29, and 74.)

[KMZ+86] B. J. Kennedy, K. S. Murray, P. R. Zwack, H. Homborg, and W. Kalz. Spin States in Iron(iii) Phthalocyanines Studied by Mössbauer, Magnetic Susceptibility, and ESR Measurements. Inorg. Chem. **25**, 2539, 1986. (Cited on page 51.)

[KSG03] K. Kadish, K. M. Smith, and R. Guilard, editors. *The Porphyrin Handbook*, volume 19. Academic Press, New York, 2003. (Cited on page 4.)

[KvO05] J. Koch and F. von Oppen. Franck-Condon Blockade and Giant Fano Factors in Transport through Single Molecules. Phys. Rev. Lett. **94**, 206804, 2005. (Cited on page 33.)

[KYB08] S.-H. Ke, W. Yang, and H. U. Baranger. Quantum-Interference-Controlled Molecular Electronics. Nano Lett. **8**, 3257, 2008. (Cited on page 41.)

[LA89] I.-W. Lyo and P. Avouris. Negative Differential Resistance on the Atomic Scale: Implications for Atomic Scale Devices. Science **245**, 1369, 1989. (Cited on page 41.)

[LDWG15] L. Liu, T. Dienel, R. Widmer, and O. Gröning. Interplay between energy-level position and charging effect of manganese phthalocyanines on an atomically thin insulator. ACS Nano **ASAP**, 2015. (Cited on pages 1 and 2.)

[LRM07a] P. Liljeroth, J. Repp, and G. Meyer. Current-induced hydrogen tautomerization and conductance switching of naphthalocyanine molecules. Science **317**, 1203, 2007. (Cited on page 2.)

[LRM07b] P. Liljeroth, J. Repp, and G. Meyer. Current-Induced Hydrogen Tautomerization and Conductance Switching of Naphthalocyanine Molecules. Science **317**, 1203, 2007. (Cited on page 4.)

[LS01] M.-S. Liao and S. Scheiner. Electronic structure and bonding in metal phthalocyanines, Metal=Fe,Co,Ni,Cu,Zn,Mg. J. Chem. Phys. **114**, 9780, 2001. (Cited on pages 11, 12, and 63.)

[Man67] J. B. Mann. Atomic Structure Calculations I. Hartree-Fock Energy Results for the Elements Hydrogen to Law-rencium. Technical report, Los Alamos Scientific Laboratory of the University of California, 1967. (Cited on pages 11 and 20.)

[MBF+11] V. Meded, A. Bagrets, K. Fink, R. Chandrasekar, M. Ruben, F. Evers, A. Bernand-Mantel, J. S. Seldenthuis, A. Beukman, and H. S. J. van der Zant. Electrical control over the Fe(II) spin crossover in a single molecule: Theory and experiment. Phys. Rev. B **83**, 245415, 2011. (Cited on page 51.)

[MBG+15] M. Misiorny, E. Burzurí, R. Gaudenzi, K. Park, M. Leijnse, M. R. Wegewijs, J. Paaske, A. Cornia, and H. S. J. van der Zant. Probing transverse magnetic anisotropy by electronic transport through a single-molecule magnet. Phys. Rev. B **91**, 035442, 2015. (Cited on pages 63 and 67.)

[MBNE+15] J. Martinez-Blanco, C. Nacci, S. C. Erwin, K. Kanisawa, E. Locane, M. Thomas, F. von Oppen, P. W. Brouwer, and S. Fölsch. Gating a single-molecule transistor with individual atoms. Nat. Phys. **11**, 640, 2015. (Cited on page 52.)

[MDS+08] C. A. Martin, D. Ding, J. K. Sørensen, T. Bjørnholm, J. M. van Ruitenbeek, and H. S. J. van der Zant.

Fullerene-based anchoring groups for molecular electronics. J. Am. Chem. Soc. **130**, 13198, 2008. (Cited on page 1.)

[MGD+12] T. Miyamachi, M. Gruber, V. Davesne, M. Bowen, S. Boukari, L. Joly, F. Scheurer, G. Rogez, T. K. Yamada, P. Ohresser, E. Beaurepaire, and W. Wulfhekel. Robust spin crossover and memristance across a single molecule. Nature Commun. **3**, 938, 2012. (Cited on pages 1 and 51.)

[MPD+10] M. Mannini, F. Pineider, C. Danieli, F. Totti, L. Sorace, P. Sainctavit, M.-A. Arrio, E. Otero, L. Joly, J. C. Cezar, A. Cornia, and R. Sessoli. Quantum tunnelling of the magnetization in a monolayer of oriented single-molecule magnets. Nature **468**, 417, 2010. (Cited on pages 63 and 67.)

[MRK+12] A. Mugarza, R. Robles, C. Krull, R. Korytár, N. Lorente, and P. Gambardella. Electronic and magnetic properties of molecule-metal interfaces: Transition-metal phthalocyanines adsorbed on Ag(100). Phys. Rev. B **85**, 155437, 2012. (Cited on pages 2, 4, and 63.)

[MST10] T. Markussen, R. Stadler, and K. S. Thygesen. The Relation between Structure and Quantum Interference in Single Molecule Junctions. Nano Lett. **10**, 4260, 2010. (Cited on page 41.)

[MST11] T. Markussen, R. Stadler, and K. S. Thygesen. Graphical prediction of quantum interference-induced transmission nodes in functionalized organic molecules. Phys. Chem. Chem. Phys. **13**, 14311, 2011. (Cited on page 41.)

[MWR+03] M. Mayor, H. B. Weber, J. Reichert, M. Elbing, C. von Hänisch, D. Beckmann, and M. Fischer. Electric Current through a Molecular Rod-Relevance of the Position of the Anchor Groups. Angew. Chem. Int. Ed. **42**, 5834, 2003. (Cited on pages 1 and 41.)

[NWH05] G. V. Nazin, S. W. Wu, and W. Ho. Tunneling rates in electron transport through double-barrier molecular junctions in a scanning tunneling microscope. Proc. Natl. Acad. Sci. U.S.A. **102**, 8832, 2005. (Cited on page 23.)

[OB92] E. Orti and J. L. Bredas. Photoelectron spectra of phthalocyanine thin films: a valence band theoretical

interpretation. J. Am. Chem. Soc. **114**, 8669, 1992. (Cited on page 3.)

[PG13] F. Pielmeier and F. J. Giessibl. Spin Resolution and Evidence for Superexchange on NiO(001) Observed by Force Microscopy. Phys. Rev. Lett. **110**, 266101, 2013. (Cited on page 74.)

[PLA+99] H. Park, A. K. L. Lim, A. P. Alivisatos, J. Park, and P. L. McEuen. Fabrication of metallic electrodes with nanometer separation by electromigration. Appl.Phys. Lett. **75**, 301, 1999. (Cited on page 1.)

[PLHS80] W. J. Pietro, B. A. Levi, W. J. Hehre, and R. F. Stewart. Molecular orbital theory of the properties of inorganic and organometallic compounds. 1. STO-NG basis sets for third-row main-group elements. Inorg. Chem. **19**, 2225, 1980. (Cited on page 25.)

[PVM+13] M. L. Perrin, C. J. O. Verzijl, C. A. Martin, A. J. Shaikh, R. Eelkema, J. H. van Esch, J. M. van Ruitenbeek, J. M. Thijssen, H. S. J. van der Zant, and D. Dulic. Large tunable image-charge effects in single-molecule junctions. Nat. Nano **8**, 282, 2013. (Cited on page 29.)

[QGWW02] Y. Qiu, Y. Gao, P. Wei, and L. Wang. Organic light-emitting diodes with improved hole-electron balance by using copper phthalocyanine/aromatic diamine multiple quantum wells. Appl. Phys. Lett. **80**, 2628, 2002. (Cited on page 4.)

[QLZ+08] Z. Qian, R. Li, X. Zhao, S. Hou, and S. Sanvito. Conceptual molecular quantum phase transistor based on first-principles quantum transport calculations. Phys. Rev. B **78**, 113301, 2008. (Cited on page 41.)

[QNH03] X. H. Qiu, G. V. Nazin, and W. Ho. Vibrationally resolved fluorescence excited with submolecular precision. Science **299**, 542, 2003. (Cited on page 1.)

[RDGR13] D. A. Ryndyk, A. Donarini, M. Grifoni, and K. Richter. Many-body localized molecular orbital approach to molecular transport. Phys. Rev. B **88**, 085404, 2013. (Cited on page 20.)

[RFU00] V. Rodrigues, T. Fuhrer, and D. Ugarte. Signature of atomic structure in the quantum conductance of gold nanowires. Phys. Rev. Lett. **85**, 4124, 2000. (Cited on page 1.)

[RJKT10] M. Rinkiö, A. Johansson, V. Kotimäki, and P. Törmä. Negative Differential Resistance in Carbon Nanotube Field-Effect Transistors with Patterned Gate Oxide. ACS Nano **4**, 3356, 2010. (Cited on page 41.)

[RMSac+05] J. Repp, G. Meyer, S. M. Stojković, A. Gourdon, and C. Joachim. Molecules on Insulating Films: Scanning-Tunneling Microscopy Imaging of Individual Molecular Orbitals. Phys. Rev. Lett. **94**, 026803, 2005. (Cited on page 2.)

[ROB+02] J. Reichert, R. Ochs, D. Beckmann, H. B. Weber, M. Mayor, and H. v. Löhneysen. Driving current through single organic molecules. Phys. Rev. Lett. **88**, 176804, 2002. (Cited on page 1.)

[Roo51] C. C. J. Roothaan. A Study of Two-Center Integrals Useful in Calculations on Molecular Structure. I. J. Chem. Phys. **19**, 1445, 1951. (Cited on page 79.)

[RZM+97] M. A. Reed, C. Zhou, C. J. Muller, T. P. Burgin, and J. M. Tour. Conductance of a molecular junction. Science **278**, 252, 1997. (Cited on page 1.)

[SAH+08] G. C. Solomon, D. Q. Andrews, T. Hansen, R. H. Goldsmith, M. R. Wasielewski, R. P. Van Duyne, and M. A. Ratner. Understanding quantum interference in coherent molecular conduction. J. Chem. Phys. **129**, 054701, 2008. (Cited on page 41.)

[SBH61] R. C. Stoufer, D. H. Busch, and W. B. Hadley. Unusual magnetic properties of some six-coordinate cobalt(II) complexes - electronic isomers. J. Am. Chem. Soc. **83**, 3732, 1961. (Cited on page 51.)

[SBN+11] S. Schmaus, A. Bagrets, Y. Nahas, T. K. Yamada, A. Bork, M. Bowen, E. Beaurepaire, F. Evers, and W. Wulfhekel. Giant magnetoresistance through a single molecule. Nat. Nano **6**, 1748, 2011. (Cited on pages 2 and 4.)

[SDG12] S. Sobczyk, A. Donarini, and M. Grifoni. Theory of STM junctions for π-conjugated molecules on thin insulating films. Phys. Rev. B **85**, 205408, 2012. (Cited on pages 1, 24, 26, 28, 40, 42, 43, and 46.)

[SDG13] B. Siegert, A. Donarini, and M. Grifoni. The role of the tip symmetry on the STM topography of π-conjugated molecules. Phys. Stat. Sol. (b) **250**, 2444, 2013. (Cited on page 10.)

[SID+15] F. Schulz, M. Ijäs, R. Drost, S. K. Hämäläinen, A. Harju, A. P. Seitsonen, and P. Liljeroth. Many-body transitions in a single molecule visualized by scanning tunnelling microscopy. Nat. Phys. **11**, 229, 2015. (Cited on pages 1, 2, 4, 63, and 75.)

[SK54] J. C. Slater and G. F. Koster. Simplified LCAO Method for the Periodic Potential Problem. Phys. Rev. **94**, 1498, 1954. (Cited on pages 9 and 11.)

[Skl42] A. L. Sklar. Electronic Absorption Spectra of Benzene and Its Derivatives. Rev. Mod. Phys. **14**, 232, 1942. (Cited on page 9.)

[Sla30] J. C. Slater. Atomic Shielding Constants. Phys. Rev. **36**, 57, 1930. (Cited on page 20.)

[SMC+10] S. Stepanow, A. Mugarza, G. Ceballos, P. Moras, J. C. Cezar, C. Carbone, and P. Gambardella. Giant spin and orbital moment anisotropies of a Cu-phthalocyanine monolayer. Phys. Rev. B **82**, 014405, 2010. (Cited on pages 4 and 63.)

[SNU+02] R. H. M. Smit, Y. Noat, C. Untiedt, N. D. Lang, M. C. van Hemert, and J. M. van Ruitenbeek. Measurement of the conductance of a hydrogen molecule. Nature **419**, 906, 2002. (Cited on page 1.)

[SPX+09] X. Q. Shi, W. W. Pai, X. D. Xiao, J. I. Cerdá, R. Q. Zhang, C. Minot, and M. A. Van Hove. Significant negative differential resistance predicted in scanning tunneling spectroscopy for a C_{60} monolayer on a metal surface. Phys. Rev. B **80**, 075403, 2009. (Cited on page 41.)

[SSR11] I. Swart, T. Sonnleitner, and J. Repp. Charge State Control of Molecules Reveals Modification of the Tunneling Barrier with Intramolecular Contrast. Nano Lett. **11**, 1580, 2011. (Cited on pages 1, 2, 4, 38, 39, 54, 75, and 80.)

[TES+92] M. Trometer, R. Even, J. Simon, A. Dubon, J.-Y. Laval, J. Germain, C. Maleysson, A. Pauly, and H. Robert. Lutetium bisphthalocyanine thin films for gas detection. Sens. Actuators B **8**, 129, 1992. (Cited on page 3.)

[TH83] J. Tersoff and D. R. Hamann. Theory and application for the scanning tunneling microscope. Phys. Rev. Lett. **50**, 1998, 1983. (Cited on page 3.)

[Tin64] M. Tinkham. *Group theory and quantum mechanics*. McGraw-Hill, 1964. (Cited on page 13.)

[TMH08] X. W. Tu, G. Mikaelian, and W. Ho. Controlling Single-Molecule Negative Differential Resistance in a Double-Barrier Tunnel Junction. Phys. Rev. Lett. **100**, 126807, 2008. (Cited on pages 4, 39, and 41.)

[TRC11] D. Toroz, M. Rontani, and S. Corni. Visualizing electron correlation by means of ab initio scanning tunneling spectroscopy images of single molecules. J. Chem. Phys. **134**, 024104, 2011. (Cited on page 1.)

[TRC13] D. Toroz, M. Rontani, and S. Corni. Proposed Alteration of Images of Molecular Orbitals Obtained Using a Scanning Tunneling Microscope as a Probe of Electron Correlation. Phys. Rev. Lett. **110**, 018305, 2013. (Cited on page 1.)

[TSY11] Y. Tsuji, A. Staykov, and K. Yoshizawa. Orbital Views of Molecular Conductance Perturbed by Anchor Units. J. Am. Chem. Soc. **133**, 5955, 2011. (Cited on page 41.)

[TTM+11] M. Taniguchi, M. Tsutsui, R. Mogi, T. Sugawara, Y. Tsuji, K. Yoshizawa, and T. Kawai. Dependence of Single-Molecule Conductance on Molecule Junction Symmetry. J. Am. Chem. Soc. **133**, 11426, 2011. PMID: 21740028. (Cited on page 41.)

[TZPCS11] N. Traverso Ziani, G. Piovano, F. Cavaliere, and M. Sassetti. Electrical probe for mechanical vibrations in suspended carbon nanotubes. Phys. Rev. B **84**, 155423, 2011. (Cited on page 41.)

[USR13] C. Uhlmann, I. Swart, and J. Repp. Controlling the Orbital Sequence in Individual Cu-Phthalocyanine Molecules. Nano Lett. **13**, 777, 2013. (Cited on pages 38, 39, and 80.)

[WBJJ89] R. Wilkins, E. Ben-Jacob, and R. C. Jaklevic. Scanning-tunneling-microscope observations of coulomb blockade and oxide polarization in small metal droplets. Phys. Rev. Lett. **63**, 801, 1989. (Cited on page 23.)

[WEHP+15] B. Warner, F. El Hallak, H. Prüser, J. Sharp, M. Persson, A. J. Fisher, and C. F. Hirjibehedin. Tunable magnetoresistance in an asymmetrically coupled single-molecule junction. Nat. Nano **10**, 259, 2015. (Cited on pages 4 and 23.)

[XDH+99] Y. Xue, S. Datta, S. Hong, R. Reifenberger, J. I. Henderson, and C. P. Kubiak. Negative differential resistance in the scanning-tunneling spectroscopy of organic molecules. Phys. Rev. B **59**, R7852, 1999. (Cited on page 41.)

[XT03] B. Xu and N. J. Tao. Measurement of single-molecule resistance by repeated formation of molecular junctions. Science **301**, 1221, 2003. (Cited on page 1.)

[Yu12] Z. G. Yu. Spin-orbit coupling and its effects in organic solids. Phys. Rev. B **85**, 115201, 2012. (Cited on page 64.)

[ZWW+00] C. Zeng, H. Wang, B. Wang, J. Yang, and J. G. Hou. Negative differential-resistance device involving two C_{60} molecules. Appl. Phys. Lett. **77**, 3595, 2000. (Cited on page 41.)

COLOPHON

This document was typeset using the typographical look-and-feel `classicthesis` developed by André Miede. The style was inspired by Robert Bringhurst's seminal book on typography "*The Elements of Typographic Style*". `classicthesis` is available for both LaTeX and LyX:

http://code.google.com/p/classicthesis/

Happy users of `classicthesis` usually send a real postcard to the author, a collection of postcards received so far is featured here:

http://postcards.miede.de/

Final Version as of December 4, 2015 (`classicthesis` version 4.1).